

© 2013

WEIWEI SONG

ALL RIGHTS RESERVED

OPTICAL AND THERMAL PROPERTIES OF PERIODIC PHOTONIC
STRUCTURES ON A SILICON-ON-INSULATOR PLATFORM

BY

WEIWEI SONG

A Dissertation submitted to the
Graduate School-New Brunswick
Rutgers, The State University of New Jersey
in partial fulfillment of the requirements

for the degree of

Doctor of Philosophy

Graduate Program in

Electrical and Computer Engineering

written under the direction of

Professor Wei Jiang

and approved by

New Brunswick, New Jersey

May, 2013

ABSTRACT OF THE DISSERTATION
OPTICAL AND THERMAL PROPERTIES OF PERIODIC PHOTONIC
STRUCTURES ON A SILICON-ON-INSULATOR PLATFORM

by WEIWEI SONG

Dissertation Director:

Professor Wei Jiang

Silicon photonics is the leading candidate to fulfill the high bandwidth requirement for the future communication networks. Periodic photonic structures, due to their fascinating properties including compact size, high efficiency, and ease of design, play an important role in photonic systems. In this dissertation, SOI-based one-dimensional and two-dimensional periodic photonic structures are studied.

Low crosstalk, high density integration of bus waveguides is demonstrated by employing a novel waveguide array structure. Inspired by the low coupling strength shown by initial pair waveguide experiments, novel waveguide array structures are studied by generalizing the nearest-neighbor tight-bonding model. Based on the theory, waveguide arrays have been designed and fabricated. The waveguide arrays have been characterized to demonstrate high density bus waveguides with minimal crosstalk.

Two-dimensional photonic crystal waveguide (PCW) structure was then investigated aiming at reducing the propagation loss. A general cross-sectional eigenmode orthogonality relation is first derived for a one dimensional periodic system. Assisted by this orthogonality, analytic formulas are obtained to describe the propagation loss in PCW structures. By introducing the radiation and backscattering loss factors α_1 and α_2 ,

the total loss coefficient α can be written as $\alpha = \alpha_1 n_g + \alpha_2 n_g^2$ (n_g is the group index). It is analytically shown the backscattering loss *generally* dominates the radiation loss for $n_g > 10$. Combined with systematic simulations of loss dependences on key structure parameters, this analytic study helps identify promising strategies to reduce the slow light loss.

The influence of the substrate on the performance of a thermo-optic tuning photonic crystal device was studied in the following section. The substrate-induced thermo-optic tuning is obtained as a function of key physical parameters, based on a semi-analytic theory that agrees well with numeric simulations. It is shown that for some devices, the substrate's contribution to the thermo-optic tuning can exceed 10% for a heater located in the waveguide core and much higher for some other configurations. The slow response of the substrate may also significantly slow down the overall response time of the device. Strategies of minimizing the substrate's influence are discussed.

DEDICATED

TO

my parents and my sister

ACKNOWLEDGEMENTS

This dissertation would not have been possible without the help from many people. I want to first express my sincere gratitude to my advisor, Professor Wei Jiang, for his continuous support, insightful guidance, and great patience. His enthusiasm and encyclopedic knowledge in photonics inspires my interests and also leads my study on silicon photonics. I would like to sincerely thank my thesis committee: Prof. Yicheng Lu, Prof. Jaeseok Jeon, Prof. Warren Lai and Prof. George K. Celler for their encouragement and helpful discussions. Their help is greatly appreciated. I also acknowledge the helpful collaboration with Prof. Yogesh Jaluria and Prof. Graham T. Reed.

I am grateful to my group members for their assistants and inspiring discussions. Dr. Ryan Integlia provided great help on the photonic device simulation. Words here are not enough to express my gratitude for the help from Dr. Lianghong Yin and Mr. Jun Tan on the fabrication and characterization process development. I would also like to acknowledge all the other group members, including Ms. Manjit Chahal, Mr. Siamak Abaslou, Mr. Robert Gatdula, and other previous students, postdoctors and visiting scholars, for their discussion, assistance, collaboration and help throughout my whole PhD study at Rutgers University.

I would like to express my gratitude to the staff in Brookhaven National Lab (BNL) and Robert Lorber in the MERL lab at Rutgers for their help in process developments and assistants on advanced facilities. Thanks for the valuable suggestions and assistances on the device patterning processes from Dr. Ming Lu and Dr. Aaron Stein at Brookhaven National Laboratory.

This work has been supported by AFOSR Grant No. FA9550-08-1-0394 (through the office of G. Pomrenke), and by the DARPA Young Faculty Award Grant No. N66001-12-1-4246. Part of the fabrication was carried out at the Center for Functional Nanomaterials of Brookhaven National Laboratory, which is supported by the U.S. Department of Energy, Office of Basic Energy Sciences, under Contract No. DE-AC02-98CH10886.

TABLE OF CONTENTS

ABSTRACT OF THE DISSERTATION	ii
DEDICATED	iv
ACKNOWLEDGEMENTS.....	v
LISTS OF TABLES	ix
LIST OF ILLUSTRATIONS.....	x
Chapter 1 Introduction	1
1.1 Silicon as the photonic material	2
1.2 Integration of photonic circuits	6
1.3 Photonic Crystal	10
1.3 Waveguides and waveguide lattice	13
1.4 Photonic crystal waveguide.....	17
1.5 Thermo-optic tuning of the photonic crystal waveguide structure	22
1.6. Fabrication of photonic devices based on the SOI platform	24
1.7. Characterization of the photonic devices	33
1.8. Organization of the Dissertation	34
Chapter 2 High-density bus waveguides based on the asymmetric-waveguide-array structure.....	36
2.1. Constrains on high-density waveguide integration	37
2.1.1 Constrains on the waveguide geometry	37
2.1.2 Constrains on the adjacent waveguides coupling	40
2.1.3 Constrains from the system level and the signal integrity	43
2.2. Design of asymmetric waveguide array	45
2.3. Fabrication and characterization of the 3-AWA bus waveguides.....	50
2.4. Performance improvement and discussion.....	54
2.4. Summary	57
Chapter 3 Optical propagation loss properties of PCW.....	59
3.1. Propagation loss in PCWs	60

3.2. Theory on Scattering Loss.....	62
3.2.1. Coupled mode theory and mode orthogonality in a PCW crossection.....	62
3.2.2. Separate calculation of backscattering loss and radiation loss	66
3.3. Analytic formulas for backscattering and radiation losses.....	71
3.4 Comparison with experiments.....	74
3.5 Loss dependence on structure and roughness parameters and loss reduction strategies.....	76
3.6 Summary	78
Chapter 4 Influence of substrate on PCW thermo-optic devices.....	80
4.1 Model used for multi-scale device	81
4.3 Analogy between steady heat conduction and electrostatics problems.....	84
4.4 Simulation and Analytic Results	86
4.4.1 Semi-analytical model and a comparison with FEM simulation results	86
4.4.2 Fractional thermo-optic tuning due to the substrate	90
4.4.3 Transient response of the TO PCW devices	94
4.4.4 Minimizing the substrate-induced thermooptic effect.....	96
4.5 Minimizing the substrate-induced thermooptic effect	100
4.6 Summary	102
Chapter 5 Conclusions and suggestions for future works.....	103
5.1 Conclusions	103
5.2 Suggestions for future works.....	104
References.....	107
Curriculum Vitae.....	115

LISTS OF TABLES

Table 1.1 Comparison on some semiconductor materials.....	2
Table 1.2 International Technology Roadmap for Semiconductors (ITRS).....	4
Table 1.3 The efficiency of different communication links.....	9
Table 4.1 Empirically values of X_{spr} and $\kappa_{eff} / \kappa_{Si}$ for different hole size	84

LIST OF ILLUSTRATIONS

Figure 1.1 Schematics of 1-D, 2-D, 3-D photonic crystal structures.....	10
Figure 1.2 2-D photonic crystal and typical band diagram.....	12
Figure 1.3 Schematics of strip, ridge, and slot waveguides and the corresponding electric field distributions.....	13
Figure 1.4 Propagation of light in waveguide lattice.....	16
Figure 1.5 Photonic crystal waveguide and its corresponding band structure.....	18
Figure 1.6 Connector between a strip waveguide and a PCW.....	21
Figure 1.7 Schematics of a TO tuned PCW.....	22
Figure 1.8 Fabrication process flow chart for the air-bridge PCW structure by negative EBL resist.....	26
Figure 1.9 Schematic diagram of the JEOL 6300EBL system.....	28
Figure 1.10 Stitching problem of EBL.....	29
Figure 1.11 Schematics of the ICP.....	31
Figure 1.12 Schematics of the testing system.....	33
Figure 2.1 Field distributions of confined modes for waveguides at different sizes.....	38
Figure 2.2 Schematics of the directional coupler.....	40
Figure 2.3 Crosstalk between parallel waveguides with different width.....	41
Figure 2.4 Schematics of the asymmetric-waveguide-array.....	45
Figure 2.5 Coupling between waveguides in two unit cells.....	48
Figure 2.6 Broadband transmission response of the 3-AWA bus waveguides.....	49
Figure 2.7 Characterization of the 3-AWA.....	51

Figure 2.8 SEM images on sidewall roughness.....	53
Figure 2.9 Characterization of the 5-AWA	55
Figure 3.1 SEM images on plane-view and cross-section of a air-bridge PCW.....	61
Figure 3.2 Schematics of the propagation losses in a PCW.....	66
Figure 3.3 In-plane view of a line-defect PCW and a SEM on one hole of a fabricated PCW	69
Figure 3.4 Loss factors as a function of frequency and the contribution from each pair of rows of holes.....	70
Figure 3.5 Comparison of the analytic formula with experimental results.....	75
Figure 3.6 Variation of α_2 with critical device parameters.....	76
Figure 4.1 Schematic configuration of an active silicon photonic crystal waveguide structure based on the SOI platform.....	81
Figure 4.2 Temperature distribution in the top silicon device layer.....	83
Figure 4.3 A typical steady state simulation result with a full substrate thickness.....	85
Figure 4.4 Schematics of the heat spreading model.....	87
Figure 4.5 Temperature profiles in the substrate along z -axis.....	89
Figure 4.6 Fractional delay perturbation due to the substrate.....	91
Figure 4.7 The trend of fractional delay perturbation	93
Figure 4.8 Transient response to a square-wave signal.....	95
Figure 4.9 Influence of some critical device parameters on $f_{\text{sub}}(L \rightarrow \infty)$	97
Figure 4.10 Transient response for a non-optimal configuration.....	99

Chapter 1 Introduction

Silicon photonics is a technology to implement various optical functionalities by silicon [1-3]. It has attracted a great deal of attentions and remarkable progresses have been made during the last three decades [4-7]. Silicon-based photonic systems, due to their capability of providing high bandwidth and low power consumption, are considered to be the leading candidate to overcome the communication bottleneck of the interconnect systems commonly used in the high-performance computing systems and the internet data centers [7,8]. It is anticipated that the interconnect market will gradually transit from the metal-based electronic technology to the silicon-based photonic technology [8].

Research on silicon photonics can be dated back to the mid-1980s and motivated by its compatibility with the mature silicon microelectronics industry [4]. The early works, which mainly focused on some fundamental properties of the basic building blocks of a photonic circuit, such as waveguides, switches, and modulators, laid the foundation of the silicon photonics. The advancement of the micro-processing technology in the last decades made it possible to overcome some traditional limits, such as high propagation loss, high fiber-to-chip coupling loss, low electro-optic coefficient, severe fluctuation of device performance, etc., for practical applications. The state-of-the-art technology enables not only the demonstration of a large number of single-function ultra-compact high-performance photonic components, but also the integration of silicon photonic systems.

1.1 Silicon as the photonic material

Table 1. 1 Comparison on some semiconductor materials [9,10]

	Si	SiO ₂	SiN	Ge	GaAs	GaN
Band gap (eV)	1.12	9	5	0.66	1.42	3.44
Band type	Indirect	NA	NA	Indirect	Direct	Direct
Refractive index (at 1550nm)	3.46	1.46	2.05	4.05 (at 2.8um)	3.3	2.3
Mechanical hardness (Knoop: kg/mm ²)	1150	790	1450	780	750	1200
Thermal conductivity (W/(m·K))	148	1.4	30	59.9	55	130
Thermo-optic effect coefficient (10 ⁻⁶ /K)	200	-2.9	NA	460	250	61

As the most well-understood material in the world, silicon has many superior properties comparing with other candidates [1, 2], as shown in Table 1.1. First of all, it has a band-gap 1.12eV, which makes it transparent for light with wavelength longer than 1.1μm. Experiments show a low-propagation-loss window extending from 1.1μm to 7μm for single-crystal silicon, which makes it quite suitable to implement the near-infrared telecommunication band (1.3-1.55μm) [1]. Secondly, the cost for unit area of high-quality material is low. And because of its superior mechanical properties, wafer with an extremely large diameter (>300mm) can be cost-effectively obtained, which significantly reduces the cost on unit area of devices. Moreover, compared with the III-V materials, for example, GaAs, silicon has superior thermal conductivity (3 times higher) and higher optical damage threshold (10 times higher). When compared with the silicon dioxide, which is widely used in telecommunication systems, silicon has a Raman effect

coefficient 1000 times stronger, which makes the on-chip optical-amplification possible [1,2,5].

The progresses of the silicon-on-insulator (SOI) technology make silicon more preferable, especially after the high-quality SOI wafer became commercially available in late 1990s [11]. In fact, the availability of low-cost, high-quality SOI wafers is one of the most fundamental elements to ignite the study of silicon photonics [4]. One reason that the SOI platform is ideal for the integration of photonic systems comes from the high index contrast between silicon (~ 3.46) and silica (~ 1.45) [1,12-14]. This high index contrast enables a strongly confinement of light on the sub-micron scale, which shrinks the size of photonic devices by orders of magnitude when comparing with that made by doped silica (optical fiber). Propagation loss on the order of 1dB/cm in the 1550-nm wavelength range has been demonstrated by strip waveguide made on SOI with a dimension $\sim 500 \times 200 \text{ nm}^2$ [5,7,14]. Such tight confinement and low propagation loss lay down the foundation for the large-scale integration of photonic circuits. From the point of individual devices, it also enables the implementation of various nonlinear-optical effects on chip [1, 12].

The original, and also the most important, reason to investigate silicon photonics is to utilize the well-developed silicon micro-processing technique and to fabricate photonic circuits in a cost-effective manner [3-7]. Recent advancements in nanofabrication technology make it possible to accurate control the device dimension (on the order of nanometers as shown in Table 1.2) and at the same time to reduce sidewall roughness [14-16]. For waveguide-based photonic devices, such as, ring resonator, Mach-Zehnder Interferometer, directional coupler, arrayed waveguide grating, etc., their performance is

essentially determined by the waveguide's dimension, which makes the dimension control of photonic devices much challenging.

Table 1. 2 International Technology Roadmap for Semiconductors (ITRS) [17]

Year	CMOS generation (Feature size)	Lithography system	Overlay accuracy	Critical dimension control 3σ
1999	180nm	N.A.	65nm	18nm
2001	130nm	248nm	46nm	15.9nm
2004	90nm	N.A.	32nm	11nm
2006	65nm	193nm	N.A.	7.4nm
2008	45nm	193nm	14.9nm	4.7nm
2010	32nm	N.A.	10nm	2.5nm
2011	22nm	N.A.	7.2nm	2.3nm
2012	20nm	N.A.	6.6nm	2.1nm

The main drawback of the all-silicon photonic circuit is the lack of high-efficient light emission and amplification components, which is due to the indirect band structure of silicon [6]. Several strategies have been used to overcome this deficiency [1,2,3]. In 2004, the first silicon Raman laser was demonstrated by utilizing the high Raman gain coefficient of silicon at 1550nm [18]. The quantum confinement effect provides another promising approach to realize lasing from silicon [2]. In nano-crystallined silicon, the emission efficiency can be enhanced by orders of magnitude due to the modification of energy levels by the confinement. Assisted by Erbium doping, nanosilicon can be used to implement broadband signal amplification. An external light source can also be used by coupling light into the photonic circuit, just like the external power source of an electrical circuit [19]. Such kind of configuration is widely used in uncomplicated circuits and the characterization of individual devices. But it suffers low efficiency and large footprint. A more preferable approach is to utilize the hybrid technologies, such as III-V/SOI wafer bonding [20], to implement the light source on chip. The bonded III-V material can be

used as the light source or gain media to realize high-efficiency lasing or optical amplification. Besides the wafer bonding, other hybrid techniques, such as the selective heteroepitaxial growth of GaN, Ge, etc, are also being investigated.

Research on individual devices has made tremendous progress during the last three decades [1-8]. Different kinds of materials, structures, and fabrication techniques are introduced into the silicon photonics and studied. For example, due to the lack of strong linear electrooptical effect, which comes from its centrosymmetric crystal structure, silicon was believed not suitable for active devices, such as modulators and switches [4]. However, R. A. Soref and B. R. Bennett showed that [21], by changing the free carrier concentration in silicon, the refractive index and the absorption coefficient can be modulated. The modulation, at around 1550nm, can be empirically modeled as:

$$\begin{aligned}\Delta n &= \Delta n_e + \Delta n_h = -\left[8.8 \times 10^{-22} \times \Delta N_e + 8.5 \times 10^{-18} \times (\Delta N_h)^{0.8}\right] \\ \Delta \alpha &= \Delta \alpha_e + \Delta \alpha_h = 8.5 \times 10^{-18} \times \Delta N_e + 6.0 \times 10^{-18} \times \Delta N_h\end{aligned}\tag{1.1}$$

here, Δn is the change of the refractive index, ΔN is the change of the free carrier concentration, $\Delta \alpha$ is the change of the absorption loss coefficient, the subscript e/h represents the change corresponding to electron/hole. Following this discovery, silicon-waveguide-based modulators were proposed and realized. In 2004 [22], Intel demonstrated the first CMOS-compatible Si optical modulator with a modulation bandwidth higher than 1GHz by utilizing the metal-oxide-semiconductor (MOS) capacitor structure. In the year following, the slow light photonic crystal waveguide structure was introduced into this field [23]. The modulator dimension was shrunk from mm-scale to 100 μ m-scale. In the same year, the ring-resonator-based modulator was demonstrated [24]. The ring resonator structure further shrunk the device dimension to 10 μ m-scale and

improved the speed to higher than 25Gbit/s. With new materials, structures, and technologies incorporated, the performance of individual devices is continuously improved.

1.2 Integration of photonic circuits

Following with the continuous advancements of the performance and shrinking of the footprint sizes of individual devices, more and more attentions are attracted by the integration of photonic devices on circuit level [3,7,19]. There are several general guidelines for the research on photonic devices: shrinking the device size, improving the power efficiency, increasing the device speed, reducing the optical loss, enhancing the device stability, and improving the fabrication robustness, etc. On system level, there are new concerns, such as the cost, material compatibility, process sequence, power budget, signal integrity, etc [7, 15, 25]. For practical applications, it is necessary to make certain trade-offs when optimizing photonic systems.

Firstly, the improvement on the performance of the photonic system essentially relies on the advancements of individual devices. As a young and quickly growing field, new concepts are springing up in silicon photonics, quite similar to the early years of the integrated circuits (IC) in 1950s. Just like an electronic circuit that is composed by individual electronic devices, such as resistors, capacitors, MOSFETs, Operational-Amplifiers, etc., and connected by metal wire, a photonic circuit is made up by different components [7]. From the point of functionality, its basic components can be divided into passive and active devices that can generate (light source), guide (waveguide), amplify, store (optical buffer), switch/filter, modulate, and detect light. For some applications, couplers are required to couple light on/off the photonic circuit. It is the performance

improvement on each of these individual devices that enables the practical photonic integrated systems.

Secondly, it is critical to choose an appropriate processing technology to fabricate photonic circuits [26]. The 193nm, or even 248nm, lithography equipments are used to pattern photonic structures, due to their relatively large dimensions (on the scale of hundreds of nanometers) [15,19,27]. The most widely used CMOS node is the 130nm technology. Shown in Table 1.2, this node introduces a standard 16nm dimension variation. However, from the point of power efficiency and circuit reliability, it is suggested that nanometer-scale dimension control is necessary for devices utilizing the light interference effect, such as the wavelength-division-multiplexer (WDM) [14]. Experimentally, it has been shown that more advanced control on the processing generally gives better in-chip and die-to-die device uniformity [28]. This is due to that the device performance is strongly influenced by the sub-device structure dimension, such as the waveguide width. At the stage of development and demonstration, the processing technology is mainly limited by the cost of building and maintaining the advanced photonic-fabs [26,29]. As shown in table 1.2, the state-of-the-art CMOS technology can provide a critical dimension control on the nanometer-scale and overlay accuracy better than 10nm [17]. The problem ahead is how to cost-effectively incorporate the photonics fabrication into the more advanced CMOS technology [19].

The third concern is the integration with the electrical circuits [16]. One of the most important applications of the silicon photonics is to realize the on-chip communications, where the photonic circuits and electrical circuits are integrated together (the optoelectronic integrated circuit)[3,6]. The SOI wafer typically used in silicon photonics has a

top silicon layer thicker than 200nm and a buried oxide (BOX) layer thicker than 1 μ m. However, the advanced CMOS technology favors bulk silicon wafer. Even for the IC fabs using SOI wafers, the top silicon layer is usually thinner than 100nm and an even thinner BOX (on the 10-nm scale) is used to guarantee good thermal conductivity [26]. Some compromises must be made between electronic circuits and photonic circuits if they are integrated on the same level. As an alternative approach, the so-called back-side fabrication is proposed and developed [16]. In this method, the bulk substrate side is used to fabricate the high dense electronic circuits. The photonic systems are located on the other side. By the through-silicon vias (TSV) technology, they can be connected. Another promising approach is to utilize the well-developed wafer bonding technique. The electronic and photonic circuits are independently fabricated, then bonded together.

Last but not least, it is still an arguable issue that on what level the photonic system should be incorporated into the whole computing and communicating system [16]. In general, it is clear that, for long distance communication, the photonic technology is the leading choice. When the distance scaled down to sub-meter scale, the current photonic technology has the advantage on high bandwidth, but, at the same time, suffers lower power efficiency. Table 1.3 shows a comparison of different communication technologies based on the state-of-the-art CMOS node. In the future, it is argued that the all-electrical high-speed serial links will not increase significantly beyond 25Gb/s [30]. To meet the continuously increasing bandwidth requirement, communication systems employing new technologies, such as silicon photonics, are in demand. Beside the high bandwidth, the power efficiency of silicon photonics keeps increasing. A power efficiency as high as 2pJ/bit has been demonstrated for on-chip silicon photonic interconnects [31].

Table 1. 3 The efficiency of different communication links [30]

	Efficiency (pJ/bit)	distance	50Tb/s BW power (W)
Electrical	1-3	<1m	50-150
Optical Module	5-8	<100m	350
Silicon Photonics	2-3	km	100-150

Generally, the applications of silicon photonics can be categorized into four areas: telecommunication systems, chip-level optical interconnects, all optical computing systems, and lab-on-chip systems. Among these applications, a significant amount of attention is attracted by the chip-level photonic interconnect technology due to the increasing bandwidth requirement in IC industry [1,7,32]. The power budget and the clock-rate limitation on the ICs give rise to the parallel computation in the form of multi-core processors. The application on multi-core and multi-processor architecture, together with the high-performance computing systems and internet data centers, shows enormous marketing potentials [19]. The optoelectronic integrated circuit [3,6], which combines the advantages of photonic circuits on data communication and that of electronic circuits on data process, are proposed and extensively studied. Modulators and receivers with data rates up to 40Gbps are demonstrated. With the help of WDM technology, transmitting data at the rate of 200Gbps is realized [33] and it is easy to scale it to Tbps-scale. At the same time, power consumption on pJ/bit-scale has been demonstrated by different groups [31]. In December 2012, IBM announced that the optical communication technology based on silicon photonics had been verified in a standard 90nm CMOS manufacturing environment.

1.3 Photonic Crystal

Photonic crystal (PhC) is an important platform to implement different functionalities. In general, a PhC is a photonic structure with periodic arrangement of the refractive index [34]. Light propagating in such structure undergoes periodic perturbation. It is analogous to the case of electrons in a crystal in solid state physics, where a crystal is a three-dimensional periodic array of atoms [35]. With the Bloch's theorem, it is well-known that, under this periodic potential, electrons form the so-called *energy bands*. Similarly, the periodic refractive index leads to the photonic band structure. By proper design, there may be photonic band gaps (PBGs), which means the propagation is prohibited for light in certain frequency ranges. PBG is one of the most important properties of the photonic crystal structures [36].

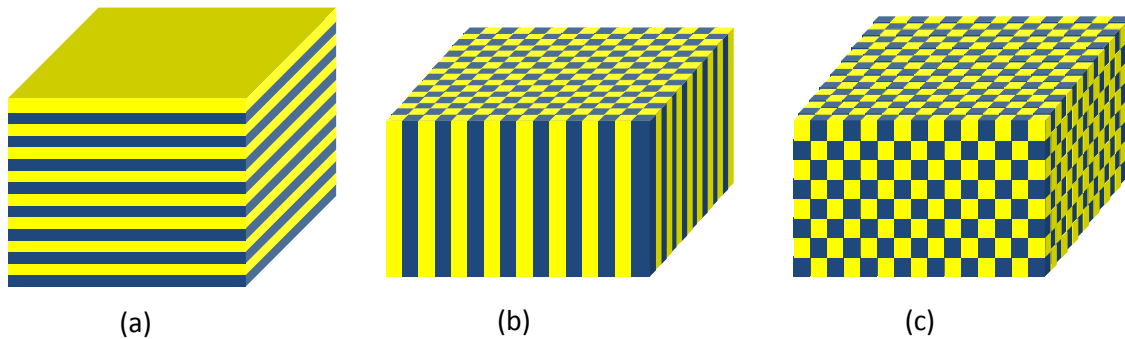


Figure 1. 1 schematics of 1-D (a), 2-D (b), 3-D (c) photonic crystal structures

From the point of the dimensionality of the periodic structure, photonic crystals can be divided into one-dimensional (1-D), two-dimensional (2-D), and three-dimensional (3-D) systems, as shown in Fig. 1.1. The 1-D photonic crystal structure is the simplest one. It can be created by depositing alternating layers of materials with different refractive indexes. Such 1-D PhC structures are widely used as reflection mirrors, such as in the

vertical-cavity surface-emitting laser (VCSEL). Another type of 1-D PhC structure is the grating. For example, based on the SOI platform, gratings can be created by periodically etching away certain width and depth of the top silicon. One important application of the grating structure is to use it as a butt-coupler to couple light from an optical fiber to a silicon photonic circuit.

For 3-D PhCs, theoretically, they can provide complete 3-D band-gap confinements due to their 3-D periodic index structures. However, the lack of precise 3-D fabrication technology impairs the quality of the fabricated 3-D photonic crystals, which in turn makes them leaky [36,37]. The fabrication of 3-D PhC is still a challenging topic.

In contrast, based on the mature SOI platform, the 2-D photonic crystal can be precisely patterned by utilizing the well-developed semiconductor planar-processing technologies. This compatibility enables the fabrication of high-quality PhC structures. The 2-D configuration also makes it easier to create, modify, and tune the functional devices [38,39].

Unlike the 3-D PhC, which has a complete 3-D bandgap confinement, 2-D PhC has a different light confinement mechanism. The 2-D periodic index structure guarantees only the confinement in the horizontal SOI plane, x - y plane in Fig 1.2a. The third dimensional confinement, along the perpendicular z direction, is implemented by the total internal reflection (TIR) effect. This effect is realized by the high index contrast between silicon and the surrounding materials, such as air or silicon dioxide. To optimize the bandgap, the thickness of the top silicon layer is usually chosen to be $\sim \lambda/2n_{eff}$, where n_{eff} is the effective refractive index of the structure.

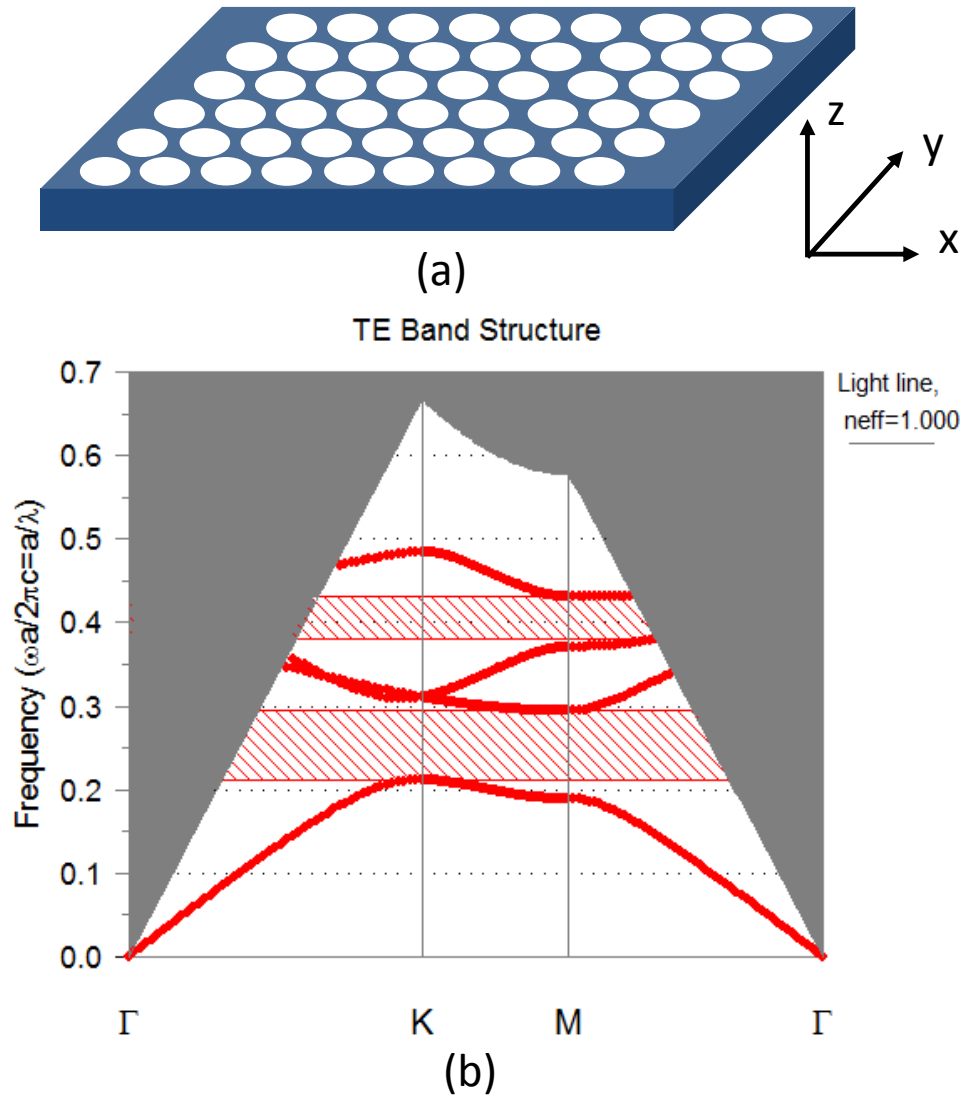


Figure 1. 2 2-D photonic crystal and its band diagram (a) Schematic of the 2-D SOI based photonic crystal and (b) the typical band structure

Photonic crystals, due to their band structures, can be used to implement different functionalities. Due to the spatial dispersion effect, PhCs can be used to modulate the propagation of light [40]. For example, enormous beam steering can be obtained by utilizing the superprism effect, which can be used in the wavelength-division-multiplexing (WDM) technology. The frequency dispersion effect of the PhC can be used

to realize the slow light effect [41]. The high quality PhC also enables the efficient confinement of light into some defect structures to create tiny cavities with ultra-high quality (Q) factors. The capability of strong light confinement in a small cavity makes the PhC structure superior to enhance the light-matter interactions [42], which is critical for nonlinear optics.

1.3 Waveguides and waveguide lattice

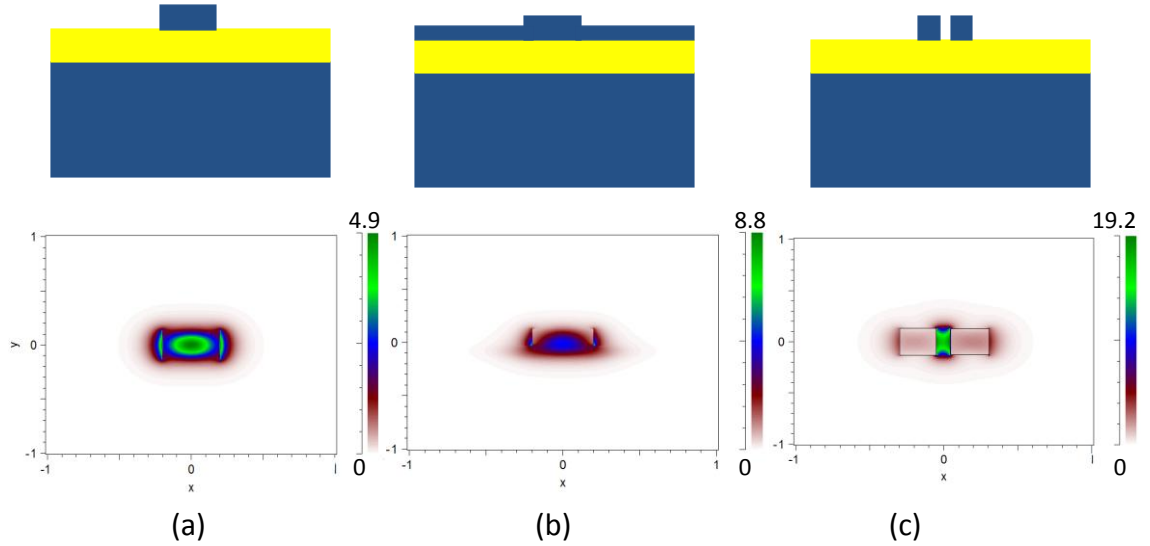


Figure 1. 3 Schematics of strip (a), ridge (b), and slot (c) waveguides and the corresponding electric field distributions

The high refractive index contrast between silicon and silicon dioxide enables strong light confinement waveguides with dimensions on the sub-micron scale [7]. Fig. 1.3 shows three types of waveguides that are frequently used in silicon photonics [5]. Among them, the strip waveguide and ridge waveguide are commonly used as bus waveguides to exchange signals between devices. The strip waveguides are created by completely

etching through the top silicon layer. In contrast, the top silicon layer is partially etched in a ridge waveguide. Due to fabrication imperfections, especially the sidewall roughness, silicon waveguides are suffering the propagation loss. The ridge waveguide, due to the relatively less overlap between the electromagnetic field and the sidewall, shows lower loss ($\sim 0.1\text{dB/cm}$) [43]. However, this is based on the sacrifice of lowering the effective index contrast, which hinders the high density integration.

Following with the trend of the “Moore’s Law for photonics”, more and more photonic devices will be integrated on one chip and the integration density will continuously be increased [44]. This trend is based on the assumption that highly efficient data communication between different photonic devices and circuits can be achieved in a cost-effective and compact way. Analogous to the functions of copper wires in electrical circuits, in photonics, waveguides are used to connect and exchange signals between different devices and circuits. However, when two waveguides are put closely together, light can be coupled from one waveguide to the other. This coupling can be described by the coupled-mode theory [45]. For lossless weakly-coupled two straight waveguides, it can be described as

$$\begin{aligned}\frac{dC_1(z)}{dz} &= -i\kappa_{12}C_2(z)\exp[-i\Delta\beta z] \\ \frac{dC_2(z)}{dz} &= -i\kappa_{21}C_1(z)\exp[i\Delta\beta z]\end{aligned}\quad (1.2)$$

where C_1 and C_2 are the modes amplitudes in these two waveguides, $\Delta\beta = \beta_1 - \beta_2$, accounts for the propagation constant difference between these two waveguides, κ_{12} and κ_{21} are the coupling coefficients, which depend on the structure and the wavelength. Eq. (1.2) can be analytically solved [45]. Results show that, depending on the waveguides structure,

whole or partial of the power bounces between these two waveguides along the propagating z direction. For the case of symmetric structures, where identical waveguides are used, power can be completely transferred between them, which is the working principle of the directional coupler. However, when identical waveguides are used as bus waveguides, this coupling leads to severe crosstalk between them, which will greatly degrade the signal integrity.

If a large amount of identical waveguides are placed periodically and parallel on one plane, as shown in Fig1.4(a), they form a so called waveguide lattice structure [46,47], which can be taken as a 1-D photonic crystal. For such a periodic structure, in weakly coupling regime, the propagation of light can be described by a set of equations in the form of [48]

$$\frac{dC_n(z)}{dz} + j\kappa(C_{n-1}(z) + C_{n+1}(z)) = 0 \quad (1.3)$$

The analytic solution of Eq. (1.3) shows that the incident light is diffracted [47]. The diffraction is strongly influenced by the coupling coefficient, κ . In Fig 1.4 (b), the electric field pattern (on its major polarization direction) is shown when TE polarized light is launched into one of the waveguides. As can be seen, light spreads out quickly.

More rigorous analysis by the Floquet-Bloch theorem shows that the propagation of light has a band structure on k_z - k_x (longitudinal wavevector vs. transverse wavevector) [49]. Modifications on waveguides, which in turn modifies the dispersion relation of k_z - k_x , can be used to manage the diffraction of light in waveguide lattices. Different kinds of structures, such as linear/nonlinear index modulation along the transverse direction, curved waveguide along the longitudinal direction, segmented waveguide arrays, binary

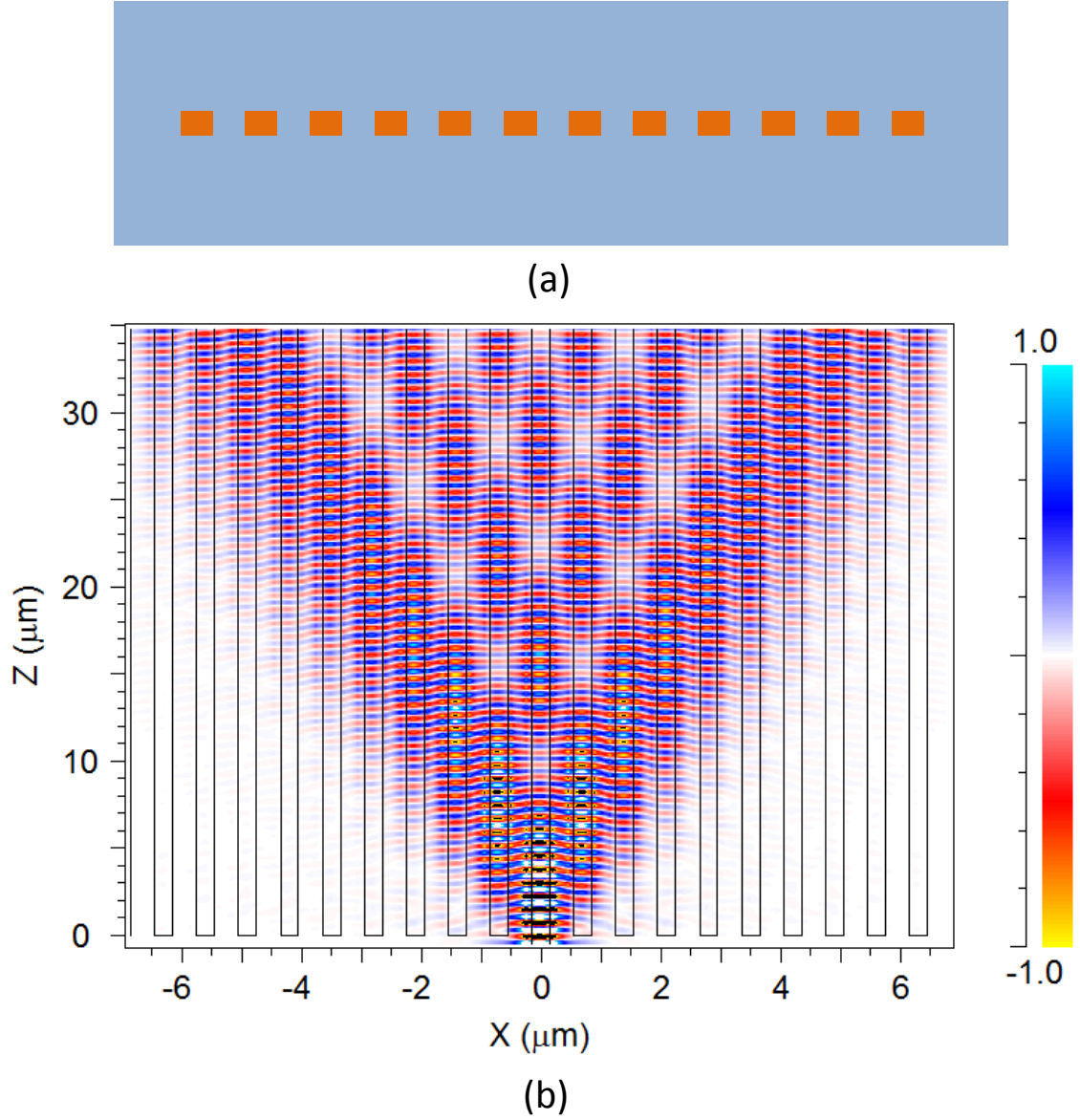


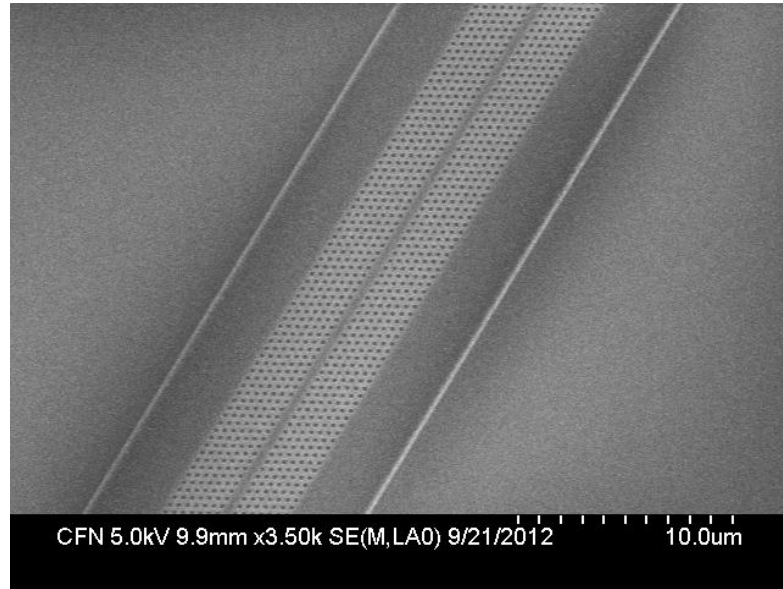
Figure 1. 4 Propagation of light in waveguide lattice. (a) schematic of the cross-section of a waveguide lattice; (b) Contour map of the electric field distribution in a waveguide lattice when light is launched into one waveguide. Parameters used: lattice constant $l=0.75\mu\text{m}$, waveguides dimension $300\text{nm} \times 260\text{nm}$. Electric field is normalized to the peak value.

waveguide structures, loss and gain engineered arrays, etc, are investigated and enormous progresses on the diffraction management have been made[46,47,50].

The management of light diffraction in waveguide lattices is investigated not only because of the interesting and fertile physics phenomena, but also due to its importance in the advanced integrated photonic circuits [32,51]. Following with the trend of “Moore’s Law for photonics”, more and more bus waveguides will be employed in the future photonic circuits and their integration density is expected to be increased to lower the cost. However, the integration density is restricted by the discrete diffraction effect as shown in Fig 1.4(b). For example, in some proposed silicon photonic interconnects, such as the Corona architecture [7], it is expected to use 270 parallel waveguides to control and transfer data. For such a huge bus waveguide array, the increasing of the integration density will directly lead to a huge size reduction of the chip.

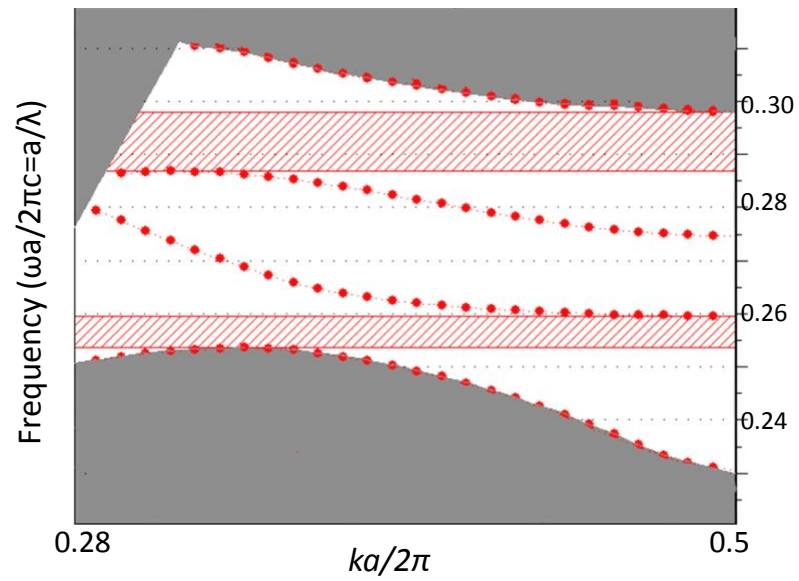
1.4 Photonic crystal waveguide

The photonic crystal waveguide (PCW) structure is another type of waveguide. Basically, for the triangular lattice air-hole PhC, the waveguide is constructed by removing one row of holes along the direction with high symmetry (Γ -K direction) [52], as shown in Fig. 1.5(a). Such a line-defect PhC structure is also called as the W1-PCW. This line-defect leads to several confined modes located in the lowest band gap of the PhC as shown in Fig. 1.5(b). For the defect modes lie under the light-line, they are confined laterally by the PBG and vertically by the TIR, and thus forming a waveguiding structure. Among these modes, for the application in photonic circuits, the most appealing mode is the fundamental TE mode (with the major electric field parallel to the photonic crystal plane).



(a)

Y-even



(b)

Figure 1. 5 PCW based on SOI (a) and the corresponding PCW band diagram

One of the most important properties shown by PCW is the so-called *slow light* effect [41]. From the band diagram of the confined TE mode shown in Fig. 1.5(b), it is evident that there is a strong frequency dispersion. From the definition of the group velocity, $v_g \equiv \nabla_{\mathbf{k}} \omega(\mathbf{k})$, the PCW shows a strong modulation of the group velocity. The group index, defined as $n_g \equiv c/v_g$, is commonly used to evaluate the slow light effect. Comparing with the group index shown by conventional homogeneous materials, which is usually less than 5, (for instance, bulk silicon has a $n_g \sim 3.5$) the group index of PCWs can be orders of magnitude higher. For example, the first experimental demonstration of the slow light effect in PCW structures shows a $v_g \sim c/90$ [53]. Combining with other structures, such as high quality cavities, the same group demonstrated that n_g can be as high as 5×10^4 [54].

Theoretically speaking, when getting close to the band edge, v_g eventually goes to zero. However, from the point of practical applications, the mode at the band edge is not of interest because it is typically accompanied by a strong group velocity dispersion (GVD). For most applications, such as delay lines, a zero-GVD is usually required to eliminate the broadening and distortion of the signal pulses [41]. Numerous works are conducted to reduce the GVD in W1-PCW at a relatively large n_g . Generally, most of the works are based on the principle that modes interactions can be used to reshape the dispersion curves [36,55-57]. By modifying the PCW structures, such as reducing the waveguide width, changing the size/position/shape of the innermost rows of holes, zero-GVD can be obtained over tens of nanometers.

Combining the requirements on the high group index and a wide range of zero-GVD, a figure of merit called the delay-bandwidth product (DBP) is generally used to evaluate the PCW designs [41]. It is defined as,

$$\Delta t \Delta f \cong \frac{L \Delta n}{\lambda}, \quad \text{and in normalized form:} \quad n_g \left(\frac{\Delta f}{f} \right) \cong \Delta n, \quad (1.4)$$

where Δt is the delay of light at the wavelength λ over a propagation length of L , Δf is the frequency bandwidth, and Δn is the change of the refractive index in the range of Δf . In most case, Δf is defined as the frequency range over which the group index variation is less than $\pm 10\%$ [57]. The DBP, especially the normalized form, is usually used to compare the design of PCW devices.

There are a lot of reasons why the slow light effect is so attractive [58]. From the point of the integration density of the photonic circuits, the slow light effect can significantly shrink the size of photonic devices. For example, the size of the widely used Mach-Zehnder interferometer (MZI) can be reduced by orders of magnitude when utilizing this effect. The slow light PCW can also be used to enhance optical non-linear effects. In a PCW, both the tight confinement and the slow light effect contribute to the enhancement of light-matter interactions, which makes it superior for the application in nonlinear optics [42]. From the point of all-optical processing system, the slow light PCW has the potential to fulfill the optical storage/buffer, which is still a missing block for the all-optical computing system.

For practical applications, in photonic crystal waveguides, the group index, n_g , can be engineered to values that is so high that it brings about coupling issues [59]. At the interface between the normal strip waveguide and the slow-light PCW, as shown in Fig. 1.6, the coupling loss increases with the value of n_g due to the enhancement of the modes mismatch [57]. Several methods were proposed and demonstrated to reduce the coupling loss. Firstly, the loss is found to be sensitive to the termination of the PCW [59]. By optimizing the PCW terminating edge, the loss can be significantly reduced. Secondly,

analogous to the widely used tapered butt-coupler structures, adiabatic taper structures are used as the couplers [60]. The third approach is to employ a fast light PCW as a coupler to efficiently convert the strip waveguide mode to the PCW mode [61,62]. The fast light PCW can be easily implemented by changing the lattice constant, hole size/position, or waveguide width. It was demonstrated that a properly designed coupling region with a total length of only several lattice periods can lead to significant improvement on the coupling efficiency [61]. By some optimization processes, the coupling loss is shown to be reduced to as less as 10% for a PCW with a slow light group index as high as 100. Based on these studies, it is generally believed that the coupling loss issue is resolved [57]. Experimental results, employing some of these strategies, show great reductions on the coupling losses [63].

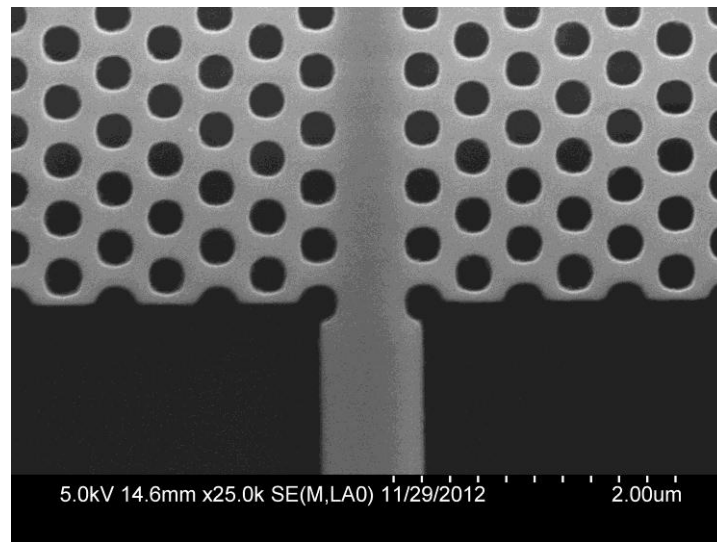


Figure 1. 6 Connector between a strip waveguide and a PCW

1.5 Thermo-optic tuning of the photonic crystal waveguide structure

Due to the centrosymmetric crystal structure of silicon, the linear electro-optic effect is absent in bulk silicon [21]. Other high order electro-optic effects, such as Kerr effect, are relatively weak for active applications in silicon photonic circuits [4,7]. For the optoelectronic integrated circuits, there are two effects, namely the thermo-optic (TO) effect and the plasma dispersion effect, that are commonly used to implement the active devices. The working principle of the plasma dispersion effect based device is shown in Eq. 1.1, where a change of the free carrier concentration results in a change of the refractive index. A device utilizing the TO effect is based on the principle that, by modulating the device temperature, the refractive index of silicon is changed. For both cases, the changing of the refractive index leads to the shift of the dispersion curve. And this shift, in turn, gives rise to the modulation of the light intensity or phase.

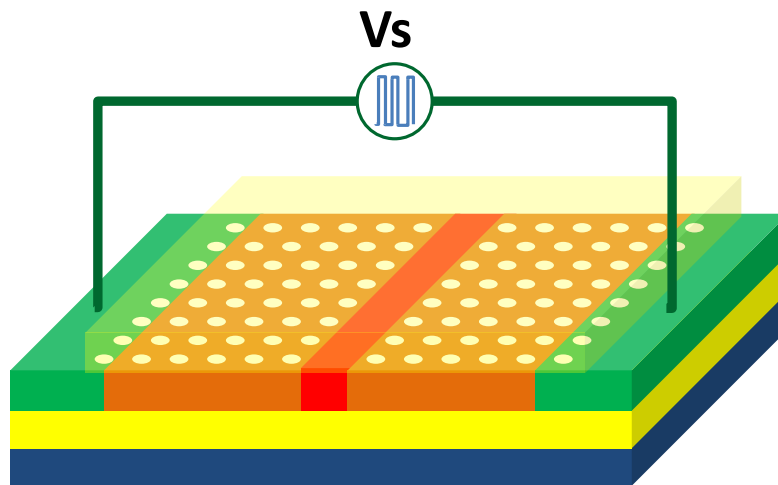


Figure 1. 7 Schematic of a TO tuned PCW

Compared to the plasma dispersion effect, the TO effect has several advantages. First of all, it can provide a larger range of modulation on the refractive index [13,64,65]. For bulk silicon, the thermally induced refractive index modulation coefficient is $\sim 1.86 \times 10^{-4} \text{ K}^{-1}$ at room temperature. Typically, the index tuning required in silicon photonics is less than 10^{-2} , which means the temperature tuning range, less than 50K, lays below the processor thermal budget. In contrast, the index tuning by plasma dispersion effect is limited to $\sim 10^{-3}$.

Secondly, the TO tuning shows lower loss. There are mainly two configurations to implement the TO effect. One is to employ the metallic heater that is microns away from the photonic device. The other one is to directly utilize the Joule heating by creating electrical heating structures through doping ($\sim 10^{14} \text{ cm}^{-3}$). The former configuration is intrinsically lossless and can be cost-effectively integrated with photonic circuit. But due to the separation between the heater and the photonic device, it takes time to heat up the device and the power efficiency is lower. In contrast, the later structure shows higher power efficiency and relatively faster response. On the other hand, it also suffers more complex fabrication and higher optical loss. However, even for the second configuration, the optical loss is still lower than the plasma dispersion based device due to the relatively lower doping level.

These advantages make the TO effect an attractive choice for the applications of active PCWs that do not work at high speed ($< \text{MHz}$) [41,66]. By thermally tuning the refractive index of silicon, the confined band of a PCW is shifted with little distortion. For a non-zero-GVD PCW, this leads to a group index change for the light propagating with a fixed wavelength. For GVD free PCW, the shift gives rise to a significant modulation on the

wave vector, which results in a large phase shift. The TO tuning PCW structure has been used to implement many photonic functionalities, such as optical switches, tunable optical delay lines, MZIs, tunable dispersion compensators, etc.

1.6. Fabrication of photonic devices based on the SOI platform

To fabricate the SOI based photonic devices, one of the most critical steps is the patterning process, which is due to the high sensitivity of their performance to the structure dimension and the sidewall roughness. The commonly used photolithography tools in academic cleanrooms, such as the Karl Suss mask aligners based on the H-line/I-line (405nm/365nm) ultra-violet, are typically not employed [37] in the patterning of micron and sub-micron scale structures. This leads to a significant increase in the fabrication cost for the academic research. One approach is to utilize the advanced photonic foundry services, such as OpSIS and Luxtera, which are just becoming available in recent years. The foundry services have a lot of advantages, such as being capable of complicated processes, high alignment accuracy, high device uniformity, and high yield. But, at the same time, they are suffering from stringent design restrictions, high cost and long fabrication period. It is an appropriate choice for the fabrication of finalized and standardized photonic devices and circuits. For academic researches, especially for the research on individual devices, it is frequently required to do timely adjustments on device structures according to the tested results on the devices fabricated in the previous round. A more flexible process flow is necessary for academic researches. Highly precise control over device dimensions with such flexibility is enabled by the so-called electron-beam lithography (EBL) technique pioneered by IBM in 1970s.

The overall process flow chart employed to fabricate air-bridge PCW structures is shown in Fig. 1.8. The process starts with a blank SOI wafer, typically with a 260nm thick single crystal top silicon layer, a 2 μ m thick thermally-grown buried oxide (BOX) layer, and a 500 μ m thick silicon substrate. After the cleaning processes and baking, the wafer is firstly coated with e-beam resist and followed by a prebaking (Fig. 1.8 (1)). Then the wafer is loaded into the EBL system and exposed by an accelerated (typically 100kV) electron beam (step 2). After the development, the device pattern is created in the resist layer. By dry etching (step (4)), the pattern is transferred to the top silicon layer. Then the e-beam resist is removed (step (5)) by wet chemical remover or dry etching. To construct the air-bridge PCW, which provides a wider bandgap, the BOX underneath the PCW should be removed. At the same time, the strip waveguides should be protected. So, hydrofluoric (HF) etching windows are created by the conventional photolithography due to their relatively large feature size ($\sim 6\mu$ m). The sample is coated with photo-resist (step (6)), exposed (step (7)), and developed (step (8)). Buffered-oxide-etchant (BOE) is then used to remove the beneath silicon dioxide (step (9)). Finally, the photo-resist is removed by acetone and followed by piranha cleaning.

As the most critical step, the EBL patterning determines the device quality. The working principle of the EBL is to use the accelerated and focused electron-beam to expose the coated ebeam-resist. When electrons hit the resist, the inelastic scattering process transfers energy from the incident electrons to the impacted atoms. The excited atoms break (positive resist) or cross-link (negative resist) the molecular chain. By controlling the exposure path, different patterns can be created. Then, after development, the device pattern is formed. As a maskless patterning technique, the EBL provides the great

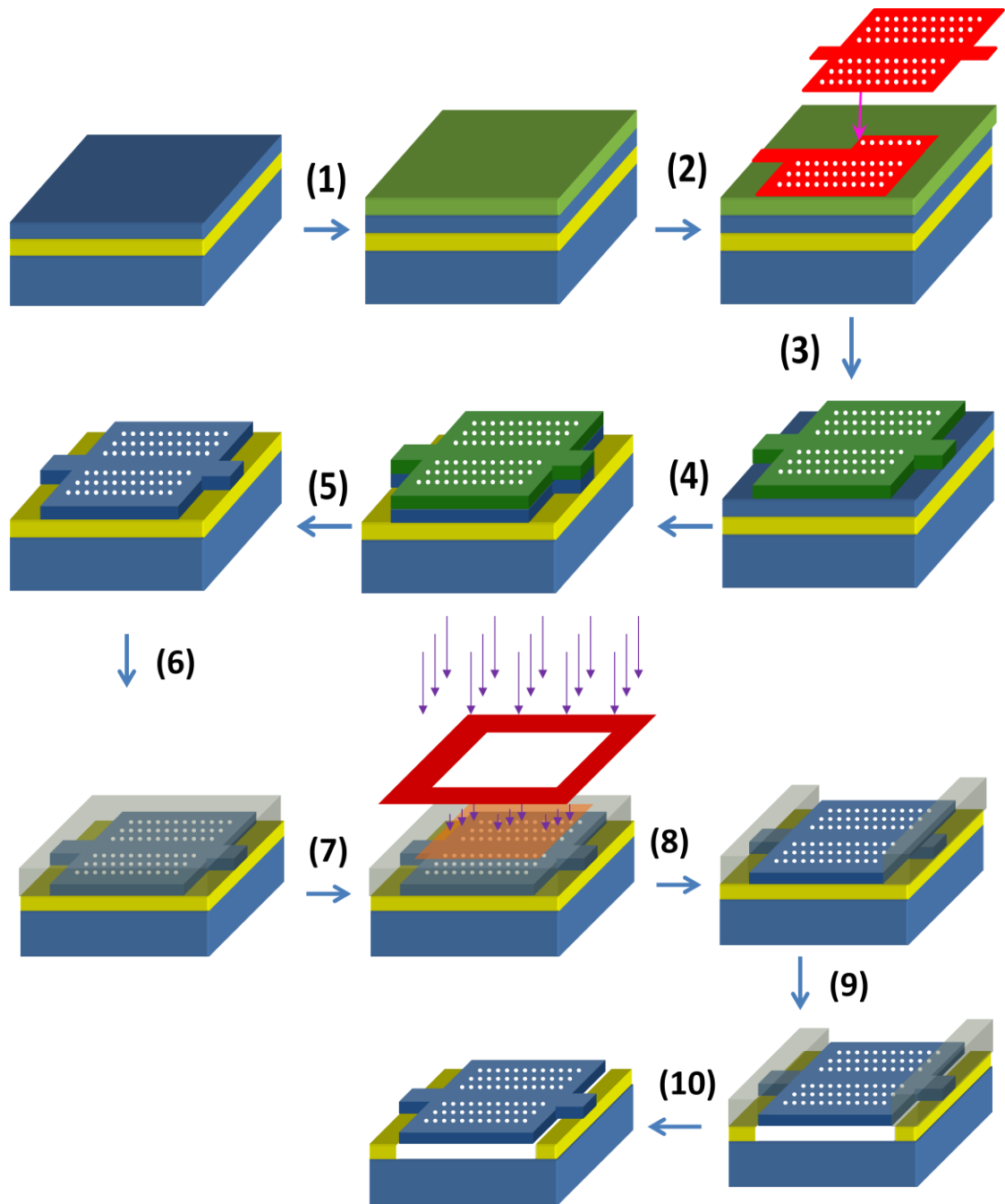


Figure 1. 8 Fabrication process flow chart for the air-bridge PCW structure by anegative EBL resist and a positive photoresist

convenience on pattern modification.

One of the most important characteristics of an EBL tool is its minimum beam size and the feature resolution. Due to the repulsion force between electrons, it is difficult to confine a large amount of electrons in a small volume. In the advanced EBL tools, both electrostatic and magnetic lenses are used to focus the electrons. The JEOL 6300 system we used has a minimum beam size $\sim 2\text{nm}$. When exposing the ebeam resist, there is the so-called proximity effect in the EBL. The proximity effect leads to an effective broadening of the beam [67]. The proximity effect is due to the scattering process in the exposure. To reduce the influence of the scattering, high energy electrons (25keV-100keV) are typically used in advanced EBL systems. Mathematically, the proximity effect can be compensated by solving the deconvolution of the point exposure profile and the desired pattern [68]. Practically, it is corrected by changing the pattern width and/or modifying the exposure dose at the pattern edges. Commercial softwares, like LayoutBEAMER used in BNL, are available for the proximity effect correction. In the practical exposing stage, the beam size is typically on the 10nm scale.

As the exposure is carried out point-by-point in the EBL, its key limiting factor is its throughput. The exposure time should be carefully estimated before one starts the EBL process. For a chosen resist, its minimum exposure dose (D) is fixed. Practically, the dose value of a resist is empirically determined by creating a dose test matrix then choosing the best dose. The time (T) required to completely expose the pattern with certain area (S) can be calculated as:

$$T = \frac{D \cdot S}{I} \quad (1.5)$$

where I is the exposure current. As shown in Eq. 1.5, resists with lower dose requirement

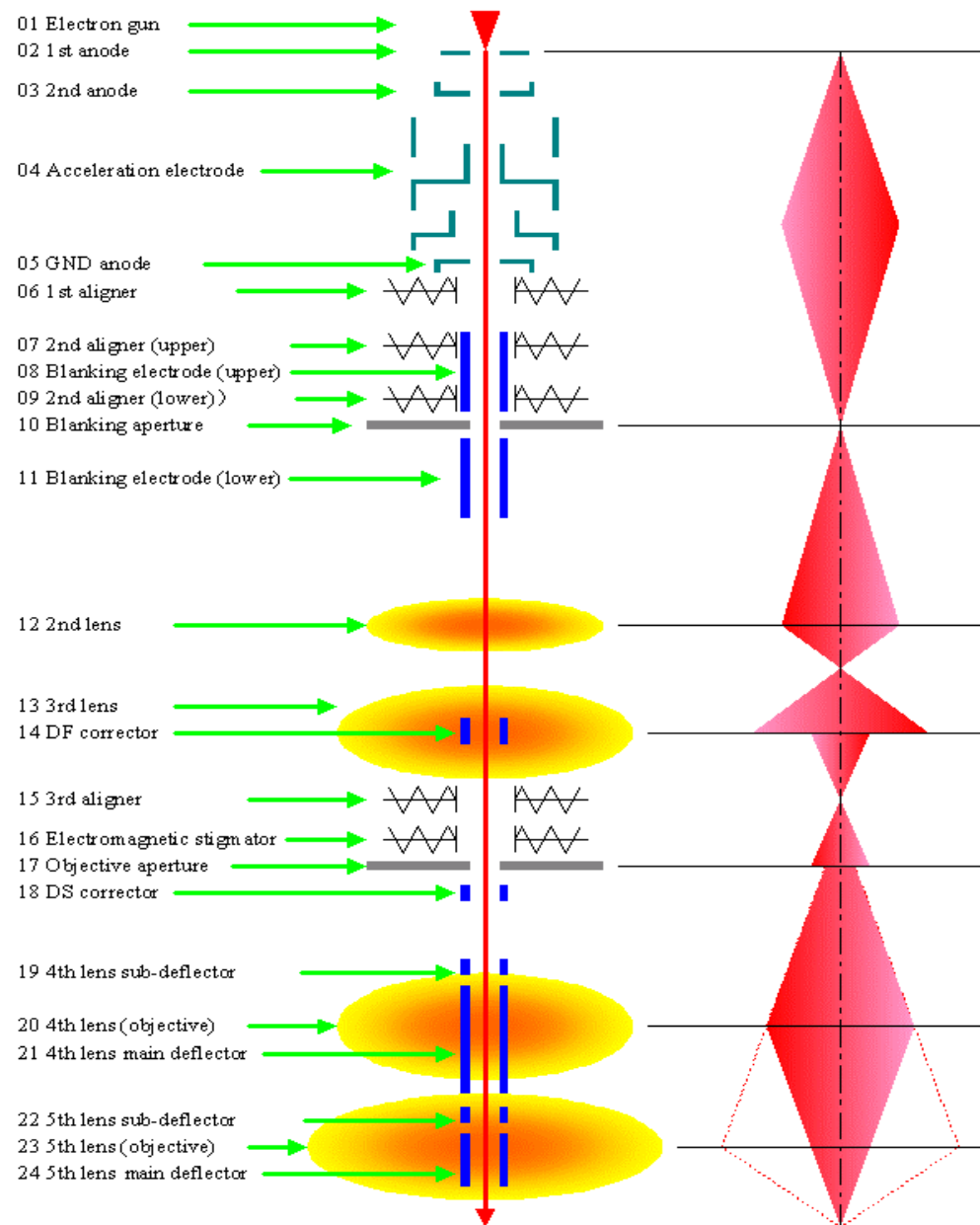


Figure 1. 9 Schemic diagram of the JEOL 6300 EBL system. Reprinted with permission from A. Stein [69].

is more preferred. By increasing the e-beam current, the exposure time can be reduced. However, higher current also brings in the beam size expansion. For example, the minimum beam size of the JEOL 9300FS system at 100keV is increased from 4nm at 200pA to 20nm at 20nA. The limited scanning speed of the EBL system gives another restriction on the choice of the exposure current,

$$I_{\max} = D \cdot A \cdot f_{\max} \quad (1.6)$$

here, A is the pixel area of one shot and f is the scanning speed. The Eq. 1.6 shows that, to fulfill certain dose requirement, the e-beam must provide enough charge for each pixel before it moves to the next point. The higher the current, the shorter the time needs to fully expose one pixel. The maximum scanning frequency, f_{\max} , gives the shortest response time of the system and, then, determines the maximum current that can be used.

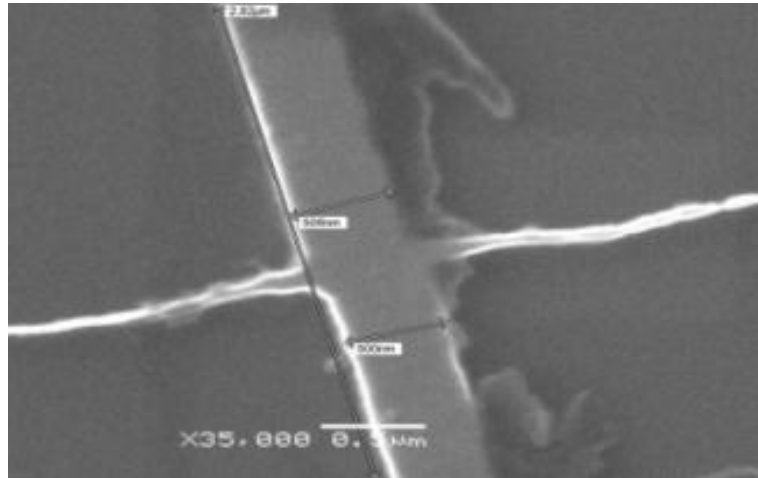


Figure 1. 10. The stitching problem of EBL for positive resist [70]

Another important issue for EBL is the alignment of different writing fields. Scanning of the e-beam is controlled by the electrostatic/magnetic deflectors. The maximum area that the deflectors can accurately control and move the e-beam is defined as one writing

field. The size of one writing field is typically on the order of 1mm^2 . For patterns larger than this size, it is necessary to move the sample-holding stage and do alignments on neighboring fields. This so-called stitching process requires high accuracy (on nm-scale) for the stage movements on mm-scales. Misalignments result in the stitching problems as shown in Fig. 1.10. In JEOL 6300, the stage movement is monitored by the laser interferometer with an accuracy of 0.6nm, which gives an overall field stitching accuracy better than 30nm. This value is comparable with the effective beam size inside the resist, which makes the large pattern exposure seamless.

The etching process is another critical step for the fabrication of photonic devices. Both the wet etching and dry etching processes are developed to pattern photonic structures. Typical wet etching processes are isotropic and can not be used to pattern structures with a line-width comparable with the layer thickness. Although some techniques have been developed to create highly anisotropic etching profile, they are just suitable for certain crystal orientation and are not compatible with the commonly used (100) silicon wafer. On the other hand, the dry etching process has the advantage of highly anisotropic etching profile. The advanced plasma-based reactive ion etching (RIE) tools provide excellent control on the etching process and the etching profile.

The inductively coupled plasma (ICP) RIE is a relatively new dry etching technique. Comparing with the conventional RIE, the ICP divides the plasma etching process into two steps, the plasma generation and the plasma acceleration [71]. As shown in Fig. 1.11, the plasma is generated in the ceramic chamber through a time-varying radio frequency (RF, 13.56MHz) source. Power is delivered to the plasma in an inductive manner through the metal coil encircling the ceramic tube. By tuning the ICP power, the incident ion

density can be modulated. The second RF source (forward power source), which generally takes the sample holding stage as the anode, is used to adjust the energy of the incident ions. By separating these two steps, it is possible to obtain high density plasma with relatively low bombardment energy, which significantly increases the etching selectivity and reduces the bombardment-induced damages.

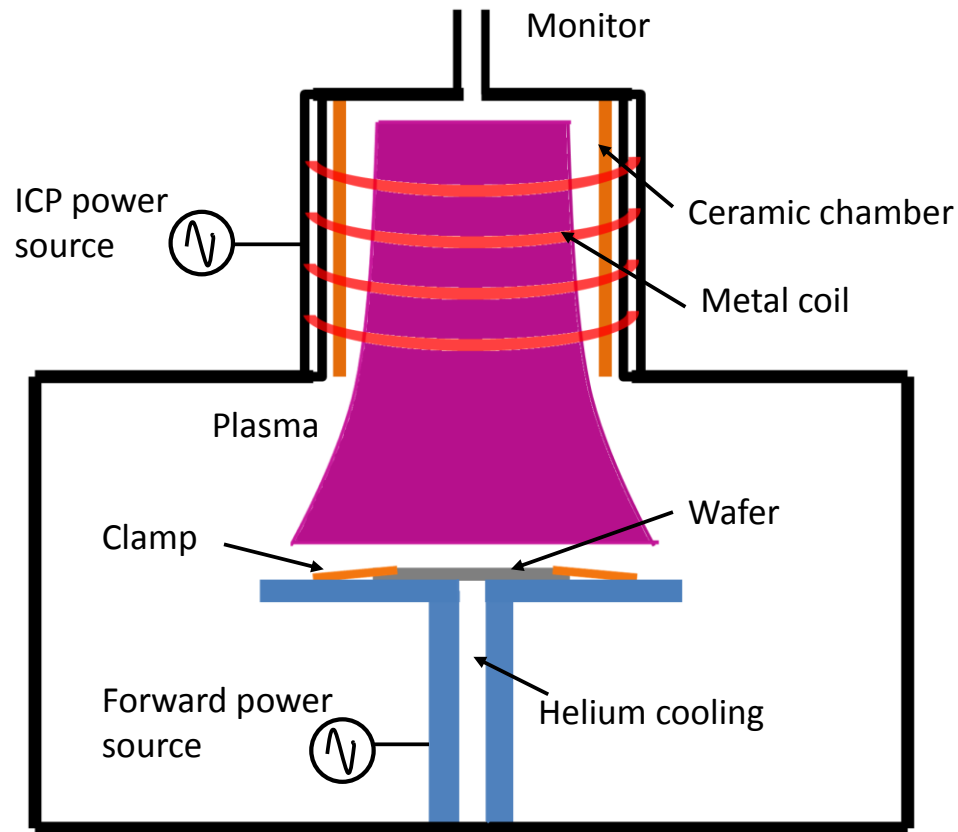
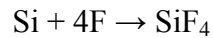


Figure 1. 11. Schematics of the ICP-RIE

Mainly two etching recipes are developed for our fabrication of silicon photonic devices. In the first recipe, a combined gas, $\text{SF}_6 + \text{O}_2$, are used as the etchant. The etching process can be described as:



At room temperature and low forward power, such an etching process shows an isotropic etching profile. To enhance its anisotropy, $-100\text{ }^{\circ}\text{C}$ is used as the processing temperature (cryogenic etching). At such a low temperature, a thin passivate layer, composed by SiO_xF_y , is formed on the sidewall during the etching process. By tuning the ratio between SF_6 and O_2 , different etching profiles can be obtained. As a general rule, less O_2 results in weaker protection on the exposed silicon surface, which means steeper the sidewall is.

The standard cryogenic etching recipe is not suitable for the fabrication of SOI-based silicon photonic devices due to its extremely high etching rate ($>100\text{nm/s}$). Reducing the etching rate is critical for silicon photonics patterning. Because the SOI wafers used in silicon photonics usually have a top silicon layer $\sim 200\text{nm}$ thick, the processing time is less than 3 seconds if the standard recipe is employed. This makes it difficult to accurately control the etching process. Once the top silicon layer is etched through, there is the notching effect, which brings in the pattern deformation and extra losses due to its non-uniformity.

Modifications are made on both the plasma generation process and the acceleration process, by lowering the ion density and reducing the incident energy. In the standard recipe, to maintain a stable plasma, the ICP power is set at or above 1200W . In the new recipe, the etching process is divided into two steps, the plasma ignition and the plasma maintenance. The ignition step uses the standard process recipe but just for a short period ($< 3\text{s}$). In this period, the plasma is ignited and a thin layer of silicon ($20\sim 40\text{nm}$) is etched. In the plasma maintenance step, the ICP power is lowered to 800W and the forward

power is lowered from 40W to 15W. The maintenance step shows an etching rate $\sim 30\text{nm/s}$ (depending on the etchant gas combination).

The second etching recipe employed is relatively straightforward. $\text{HBr} + \text{Cl}_2$ are used as the etchant [72]. It is shown that, under proper conditions, the etching is highly anisotropic and vertical etching profiles can be achieved. For the patterning of silicon photonic devices, the most significant advantage of this etching recipe is its relatively slow etching rate ($\sim 2\text{nm/s}$). Such etching rate makes the process control and monitoring more convenient when comparing with the SF_6 . It also eliminates the cross-link of the polymers of organic ebeam resists and eases the subsequent stripping process.

1.7. Characterization of the photonic devices

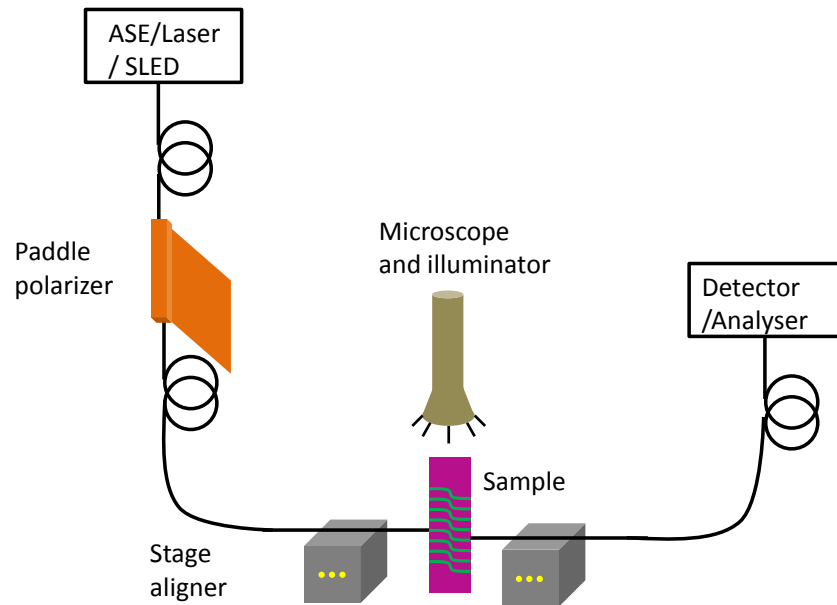


Figure 1. 12. Schematics of the testing system

Testing of the fabricated silicon photonic devices are carried out on the end-fire stage shown in Fig 1.12. For testing, several different light sources are available, including

tunable lasers, amplified spontaneous emission (ASE) sources, and superluminescent diodes (SLEDs). It is convenient to switch between different sources, which enables the broadband characterization, ranging from 1350nm to 1580nm. In the system, light is first coupled into a single mode fiber, then passing through a polarization controller. Depending on the specifications, both the extinction ratio and the polarization direction can be adjusted by the controller (a paddle polarizer). Then lens fibers are used to couple light into/out of the fabricated photonic devices. The working distance of the lensed fiber employed is 14 μ m with a spot size around 2 μ m. A CCD assisted microscope is placed on top of the chip to monitor the alignment. Due to the small dimension of the silicon bus waveguides (with a typical size at 450nm \times 260nm), an accurate control of the fiber movement is necessary to make a good alignment. Piezo-stages with a minimum step size of 20nm are employed in the set-up. Because of the mode mismatch between the lens fiber and the bus waveguide, there is a typically \sim 9dB loss on each coupling facet if no coupling structures, such as the spot-size converter, are employed. At the output side, light is collected by another lens fiber and then detected by a multimeter or a spectrum analyzer. It would be worthy to note that, almost all of the system components can be controlled by Matlab programs through one GPIB card, including light sources, piezo-stages, the microscope monitor, multimeters, and the spectrum analyzer.

1.8. Organization of the Dissertation

In the first chapter, the developments and recent progresses of silicon photonics, especially about the periodic photonic structures are briefly reviewed. Also included are the technology backgrounds on the fabrication and characterization of silicon photonic devices based on the SOI platform. In Chapter 2, the design, fabrication, and

characterization of the asymmetric-waveguide-array based bus waveguide structure are detailed discussed. In Chapter 3, an analytical theory on the propagation loss in photonic crystal waveguide structure is developed. The influence of some critical device parameters is discussed in the aim of reducing the slow light propagation loss. Chapter 4 is focused on the substrate influence of the thermo-optic tuning PCW active devices. Analytic model is developed and strategies for reducing the substrate influence are pointed out. In the final chapter, Chapter 5, a brief summary of the dissertation and some discussions on future works are presented.

Chapter 2 High-density bus waveguides based on the asymmetric-waveguide-array structure

Tremendous progresses have been made on individual silicon photonic devices during the last several decades [1-7]. Following the advancement on the performance of individual devices, more and more attentions are attracted by the integration of photonic circuits that contain multiple functional components [25-32]. It is anticipated that more and more devices will be integrated on one chip and the integration will follow the Moore's Law for photonics to lower its cost [44]. The increasing complexity of photonic circuits raises the question on how dense the circuits can be. As one of the most important and basic components, the integration density of bus waveguides will be discussed in this chapter.

The most straightforward and also the most widely studied arrangement of a large number of waveguides is to lay out the bus waveguides parallel and periodically to form the waveguide lattice structure [46,47]. In such a periodic structure, the integration at high density typically raises up the discrete diffraction problem which comes from the evanescent coupling between waveguides. Enormous works have been done to manage such diffractions [73 - 79]. But the proposed structures are either composed by complicated curved segments, which may require ultra-fine controls of the fabrication and also bring in extra losses, or working just in a narrow wavelength range. In this chapter, we propose and demonstrate a novel design based on the asymmetric-waveguide-array (AWA) structure, which is scalable and also enables an integration density on the sub-micron scale.

2.1. Constrains on high-density waveguide integration

Study on the propagation of light in parallel and periodically arranged waveguides has been intriguing and fruitful [47,50,80]. The discrete nature of such systems distinguishes them from the light propagation in bulk materials, such as the tight confinement of light in discrete waveguides. At the same time, the evanescent coupling between waveguides connects these discretized sites together and shows universal phenomena, for example the Bloch oscillation [46]. Optimization of the waveguide lattice structure can therefore be divided into two strategies: (i). design of the individual cell and (ii). design of the lattice configuration. In the proposed AWA structure, each cell is composed by waveguides with different widths and the periodic arrangement of such cells constructs the lattice. Some general design constrains will be discussed in this section.

2.1.1 Constrains on the waveguide geometry

For the integration of silicon photonic systems based on the SOI platform, typically two waveguide structures, strip and ridge waveguides, as shown in Fig. 1.3, are used as bus waveguides. Other types of waveguides, such as the slot waveguides and PCWs, are suffering high propagation loss, which eliminates their applications as bus waveguides. Comparing with strip waveguides, the ridge waveguides have the advantage of lower loss, but suffers larger device size. To achieve low loss, the waveguide width is typically chosen to be wider than $2\mu\text{m}$ [43]. The relatively high EM field in the un-etched silicon slab further hinders its application for high-density integration. In contrast, the typical width of a strip waveguide is $\sim 0.4\mu\text{m}$ and the EM field decays quickly in the exponential form as shown in Fig 2.1(a). So, from the point of potentially higher integration density, the strip waveguide is preferred.

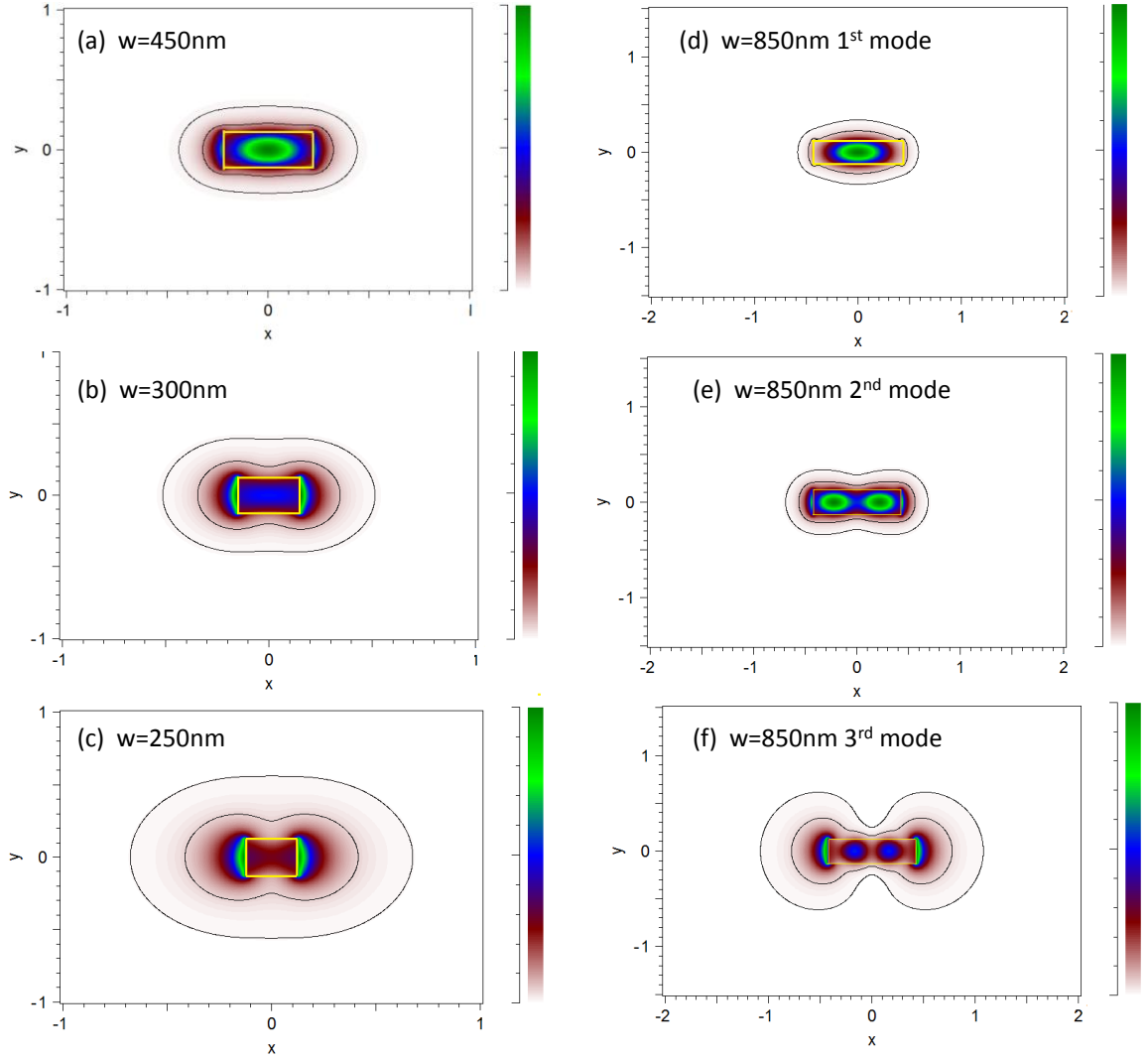


Figure 2. 1 EM field distributions of the confined modes for waveguides at different sizes. Contour curves show the position where the field intensity drops to 10% (inner curve) and 1% (outer curve) with respect to the peak intensity of the 450nm wide waveguide.

Single mode strip waveguides are more preferred in high-density integration. Besides the obvious reason that the single mode waveguide is geometrically smaller than the multimode waveguide, this comes from several other disadvantages shown by multimode waveguides. The first one is that higher order mode shows slower EM field decay outside the waveguide, as shown in Fig 2.1(d)-(f), which is not desired. For multimode waveguides, higher order mode means the EM field of the mode is more spread outside of the waveguide. This leads to an increasing of the mode-overlap with other waveguides, which in turn enhances the waveguide coupling. The second reason is that single mode waveguides show the capability of compact bending structures. For the single mode waveguide, loss on the scale of $\pm 0.005\text{dB}/90^\circ$ has been demonstrated for TE mode with a bending radius of $5\mu\text{m}$ [81]. Typically, multimode waveguides shows higher loss due to their higher leakage to the radiation modes. Moreover, bending of multimode waveguides also brings in the inter-mode mixing, which will significantly degrade the signal integrity [82].

At the same time, to minimize the propagation loss, it is preferred to employ silicon waveguides with relatively large size. The confinement of light weakens with the decreasing of the waveguide size, as shown in Fig 2.1(a)-(c). The increasing of the EM field intensity at the edge of the strip waveguide leads to an enhancement of the scattering from the sidewall roughnesses. To reduce this scattering, single mode waveguides are typically designed to be wide and working at the edge of the single mode (which means all the waveguides with wider width will support multimodes). For the design of the AWA structure, this means the narrowest waveguide should be as wide as possible to function as a low-loss bus waveguide. Based on the SOI wafer available in

our group, which has a top silicon layer thickness at 260nm, the individual waveguide widths are chosen to be in the range of 300nm-450nm.

2.1.2 Constrains on the adjacent waveguides coupling

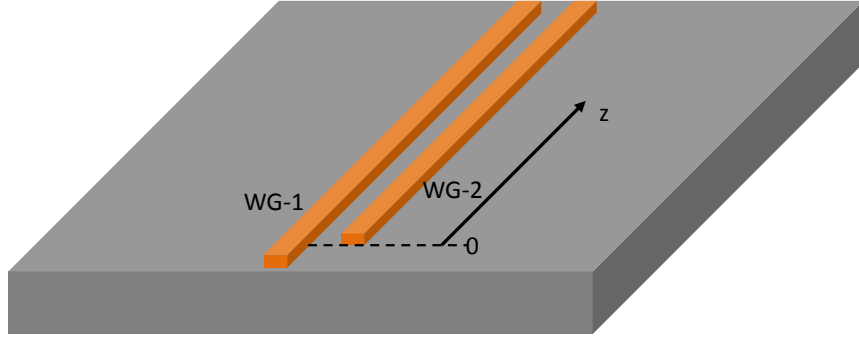


Figure 2. 2 Schematics of a directional coupler structure

To achieve low-crosstalk between waveguides in one AWA, as the first principle, coupling between adjacent waveguides should be weak. The coupling between two parallel evanescent-coupling single-mode waveguides has been extensively studied. From the coupled-mode theory [45], the power transfer between two weakly coupled waveguides can be formulated as

$$\frac{P_{1,2}(z)}{P_1} = \frac{1}{(\Delta\beta/2\kappa_{1,2})^2 + 1} \sin^2(\sqrt{(\Delta\beta/2)^2 + \kappa_{1,2}^2} z) \quad (2.1)$$

here, light is launched into waveguide 1 (WG-1), coupling starts at $z=0$, P_1 is the total power in the system, $P_{1,2}$ is the power transferred to waveguide 2 (WG-2) at a position z , $\Delta\beta$ is the propagation constant difference between these two waveguides, and $\kappa_{1,2}$ is the coupling coefficient for the transferring of power from WG-1 to WG-2. In the case of pair waveguides that are slightly different and the coupling is weak, it can be taken that $\kappa_{1,2} = \kappa_{2,1}$. Then the coupling is symmetric. The maximum value of the ratio, $P_{1,2}/P_1$, is

defined as the coupling strength and its logarithmic form, $\log (P_{1,2} / P_1)$, is defined as the crosstalk.

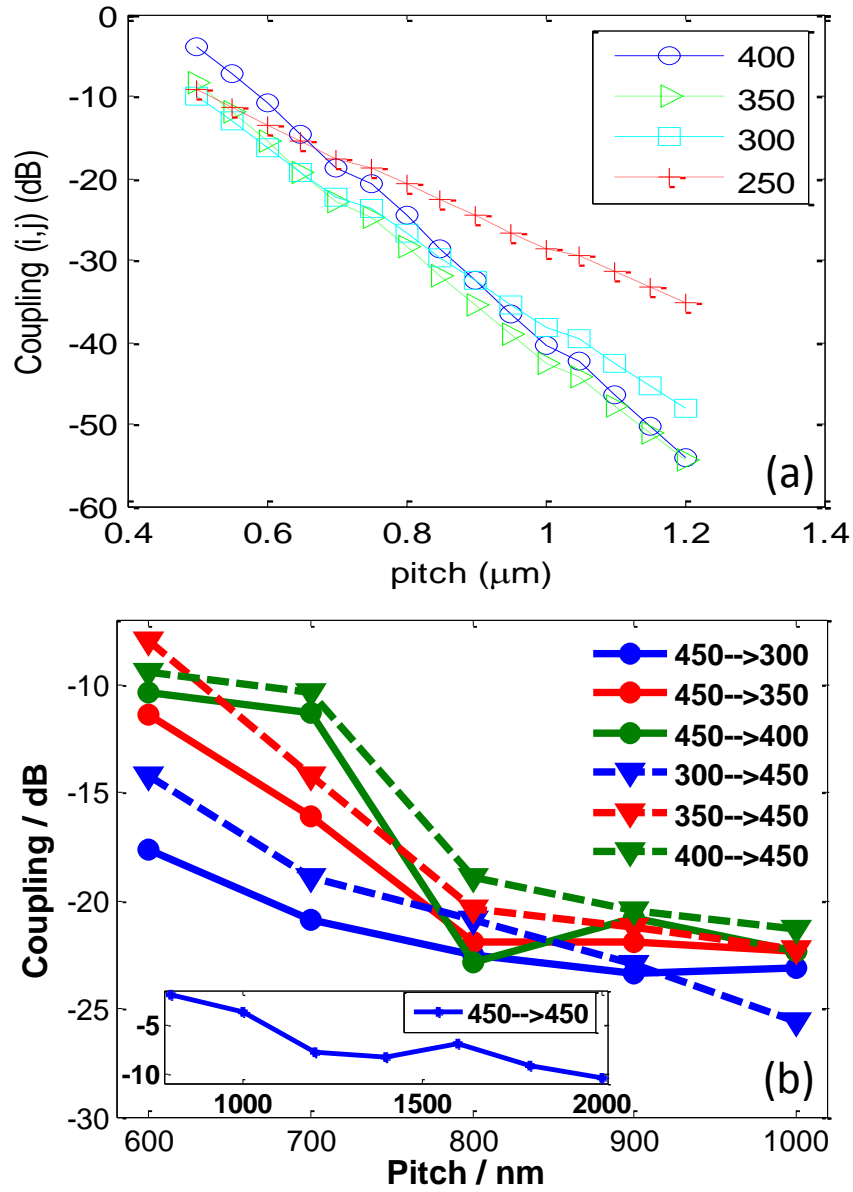


Figure 2. 3 Crosstalk between parallel waveguides with different width

As shown in Eq. 2.1, the crosstalk is determined by the value of $\Delta\beta/\kappa$. By increasing this ratio, the crosstalk can be weakened. Eq. 2.1 implies two strategies that can be used to reduce the coupling: (a) increasing the difference of the propagation constants, such as maximizing the geometric difference of the coupled waveguides; (b) reducing the coupling coefficient, for example, widening the gap between waveguides.

Simulation results on the crosstalk between two parallel waveguides, one with a fixed width at 450nm and varying the width of the other one, are plotted in Fig. 2.3(a). Clearly, crosstalk exponentially drops with the pitch size. When the pitch value is increased to 0.8 μm , the crosstalk is reduced to lower than -23dB for all the waveguide width between 300nm and 400nm. The high crosstalk level between 250nm-450nm waveguide pair is due to the high leaky EM field outside the 250nm wide waveguide. Such kind of relatively higher leaky mode also results in the smoother slope of the 300nm-450nm waveguide pair when compared with the 400nm-450nm pair. The drop of the crosstalk between parallel waveguides is experimentally demonstrated, as shown in Fig 2.3(b).

Interestingly, asymmetric coupling is shown in all the waveguide pairs. The coupling from narrower waveguide to wider waveguide is stronger than the reverse coupling. The coupling strength difference decreases with the increasing of the gap between waveguides. This is due to the difference between $\kappa_{1,2}$ and $\kappa_{2,1}$. In rigorous analysis [45], $\kappa_{m,n}$ is a function of not only the mode overlap between these two waveguides, which is symmetric, but also the mode field distribution over the other waveguide region, which is asymmetric for pair waveguides with different width. A parameter defined as

$$\chi_n = \frac{\omega \epsilon_0 \int_{-\infty}^{\infty} \int_{-\infty}^{\infty} (N^2 - N_n^2) \mathbf{E}_n^* \cdot \mathbf{E}_n dx dy}{\int_{-\infty}^{\infty} \int_{-\infty}^{\infty} \mathbf{u}_z \cdot (\mathbf{E}_n^* \times \mathbf{H}_n + \mathbf{E}_n \times \mathbf{H}_n^*) dx dy} \quad (2.2)$$

is used to characterize this difference. Here, N is the refractive index distribution of the whole system, N_n is the index distribution when only the n th waveguide is presented. $N^2 - N_n^2$ is the net permittivity difference distribution (relatively to the background), which is zero just at the site of the waveguide n . Due to the exponential decay of the field of the well-confined mode, χ_n is a small value and quickly decays with respect to the gap in the form of the square of the exponential function. That explains why the coupling strength difference is reduced at larger pitch size. When the pitch is larger than $0.8\mu\text{m}$, χ_m can be approximated as 0.

The coupling between identical waveguide is shown as the inset of Fig. 2.3(b) with the coupling length fixed at $200\mu\text{m}$. Significant power transmission, with a crosstalk level higher than -10dB , is observed over this relatively short coupling length even when the pitch is increased to $2\mu\text{m}$. The bus waveguide pitch size should be high above this value, $4\mu\text{m}$ or even wider suggested [7], to get a crosstalk level lower than -20dB . This clearly indicates that the symmetric waveguide lattice structure is not suitable for high density integration.

It is worth noting that tests on the fabricated devices show a saturation of the crosstalk reduction at $\sim -23\text{dB}$. This is due to the limited power of the light source and the detection limitation of the spectrum analyzer used.

2.1.3 Constrains from the system level and the signal integrity

On system level, research on optical interconnects [83] suggests that a crosstalk level lower than -25dB is required for coherent beam and a level lower than -12dB is tolerable for the incoherent light. For on-chip communication, with an ideal detector, to achieve a 10^{-12} bit-error-ratio (BER), the photonic interconnection network requires a signal-to-

noise ratio (SNR) at $\sim 17\text{dB}$ [84], where the SNR in optical system is defined as the ratio of the signal power over the power of the noise. If non-ideal factors [85], such as the coupling loss, finite detection efficiency, etc, are taken into account, a SNR above 20dB may be necessary. The requirement from the signal integrity on system level sets the fundamental restriction on the bus waveguide array design. No matter how the array is designed, crosstalk between any of the two waveguides should be lower than -20dB .

The low crosstalk level between waveguides should be sustained over a broad wavelength range. It has been clarified that the wavelength-division-multiplexing (WDM) technology is critical for the next-generation high speed communication networks [7,15,19]. To support the WDM technology, it is necessary that the designed bus waveguide array is capable of maintaining a high SNR over a broad wavelength range. The broadband requirement distinguishes the bus waveguide array design from the waveguide lattice targeting at the monochromatic beam localization [47].

The design should also be scalable for the convenience of being applied to different photonic systems. Different photonic circuits and their internal structures may need different numbers of bus waveguides and different SNR requirements. A good design should be capable of supporting different size of waveguide array. Its performance doesn't degrade with this scaling.

As a brief summary of these constrains, to achieve high density integration, single mode strip waveguide with a width ranging between 300nm and 450nm (based on the wafer with 260nm thick top silicon layer) are preferred to compose the AWA structure. The coupling between parallel waveguide pair indicates that the maximum integration density would be $\sim 0.8\mu\text{m}$ based on our wafer. From the point of the signal integrity, it is

required that the highest crosstalk level between all the coupled waveguides should be lower than -20dB. The array should be scalable and sustain the low crosstalk level over a wide wavelength range.

2.2. Design of asymmetric waveguide array

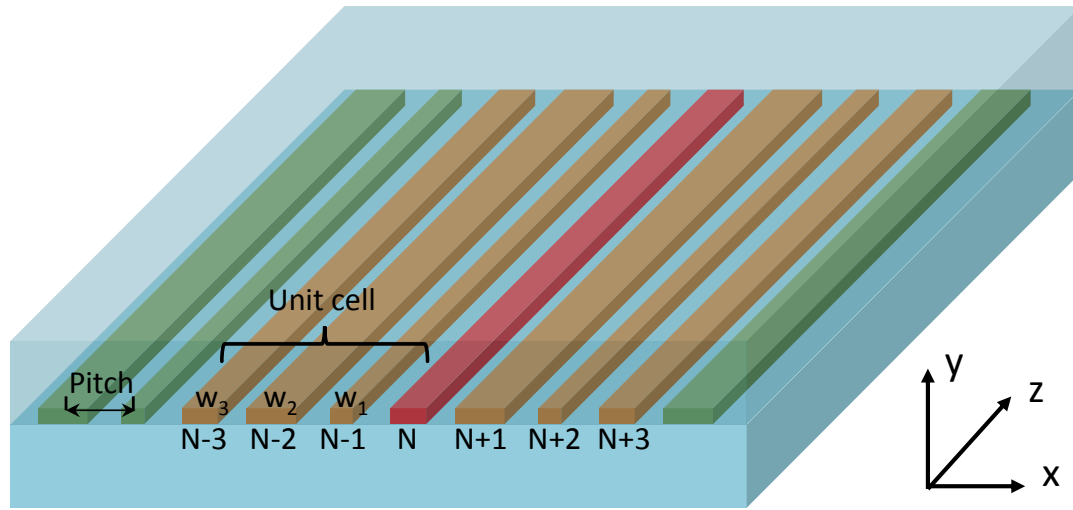


Figure 2. 4 Schematics of the asymmetric-waveguide-array. Unit cell is composed by 3 waveguides with different width. When the waveguide N is excited (marked as red), the nearest-neighbor coupled waveguides are marked as orange.

To describe the light propagation in periodically arranged waveguide lattice structure, the coupled-mode theory is developed from its original format [49]. For lattices composed by waveguides with good confinements of light, coupling can be approximated by tight-bonding, which means the mode profile outside certain range is taken as 0. The coupling can be further approximated by the nearest-neighbor tight-bonding (NNTB) approximation, where only the coupling between adjacent waveguides is taken into account [46]. In the NNTB approximation, couplings between waveguides that are

separated by other waveguides are realized by indirect-coupling, which means light hops site-by-site.

Here, we generalize the NNTB approximation for the periodic AWA structure. In the generalized NNTB (GNNTB) approach, if one waveguide is excited, coupling with the waveguides in the two nearest-neighbor cells are all taken into account. A schematic periodic AWA structure and the GNNTB approximation are shown in Fig. 2.4, where the unit cell is composed by three waveguides with different width. When the waveguide N (WG- N) is excited, the two nearest-neighbor cells are marked by orange. In general, for an ideal lossless periodically arranged AWA structure, light propagation under the GNNTB approximation can be described as

$$\frac{dA_N}{dz} = -j \sum_{-M < l < M, l \neq 0} \kappa_{N,N+l} A_{N+l} \exp(-j\Delta\beta_l z), \quad (2.3)$$

here, A_N is the mode amplitude in the WG- N , M is the total number of individual waveguides in one unit cell, $\kappa_{N,N+l}$ is the coupling coefficient accounting for the power transmitting from WG- N to WG- $N+l$, $\Delta\beta_l = \beta_{N+l} - \beta_N$ is the propagation constant difference between waveguides $N+l$ and N .

Theoretically, for an ideal waveguide lattice wherein no disturbance, such as width variations and sidewall roughnesses, happens to the waveguides, strong power exchange between identical waveguides can still be achieved if the lattice is sufficiently long. In practice, there are always certain degrees of perturbation. For example, waveguides are always lossy and there are always small width variations due to sidewall roughness, whose control is still a challenging topic for the integrated circuit. Depending on the strength of the disturbance with respect to that of the coupling, power exchange between identical waveguides can be eliminated.

When loss and the waveguide non-uniformities are taken into account, the GNNTB model has the form of

$$\frac{dA_N}{dz} = -\alpha_N A_N - j \sum_{-M < l < M, l \neq 0} \kappa_{N,N+l}^* A_{N+l} \exp(-j\Delta\beta_l^* z), \quad (2.4)$$

here, α_N is the amplitude attenuation constant, $\kappa_{N,N+l}^*$ and $\Delta\beta_l^*$ are the modified form of the coupling coefficient and the propagation constant difference, which depend on the non-uniformity. The coupling coefficient, κ , can be calculated by the effective index approximation when the waveguides are separated by other structures [86].

Numerical calculations are carried out to show the power transmission between waveguides. Firstly, the unit cell is designed in the form of equally spaced three waveguides with different width. The pitch size, defined as the center-to-center distance of two adjacent waveguides, as shown in Fig. 2.4, is chosen to be $1\mu\text{m}$ to guarantee a low crosstalk level. Couplings between waveguides in two unit cells, where are totally $2 \times 3 + 1$ waveguides arranged in the form of $450\text{nm}-380\text{nm}-330\text{nm}-450\text{nm}-380\text{nm}-330\text{nm}-450\text{nm}$, are calculated. In one set of calculation, one specific waveguide is excited by monochromatic light at $z=0$. The power distribution at different waveguide sites are then calculated at different propagation length L . The normalized power confined in each waveguide site is plotted in Fig. 2.5 with respect to the propagation length L . Each subplot of Fig 2.5 shows the discrete power distribution when one waveguide channel is excited. Note that the maximum propagation length in all the subplots is set at 1mm . This is because the evanescent power coupling shows periodic oscillations with L and, here, only the maximum power that can be coupled to other waveguides is what we concern about. For all the cases calculated, maximum power transmissions show up within 1mm .

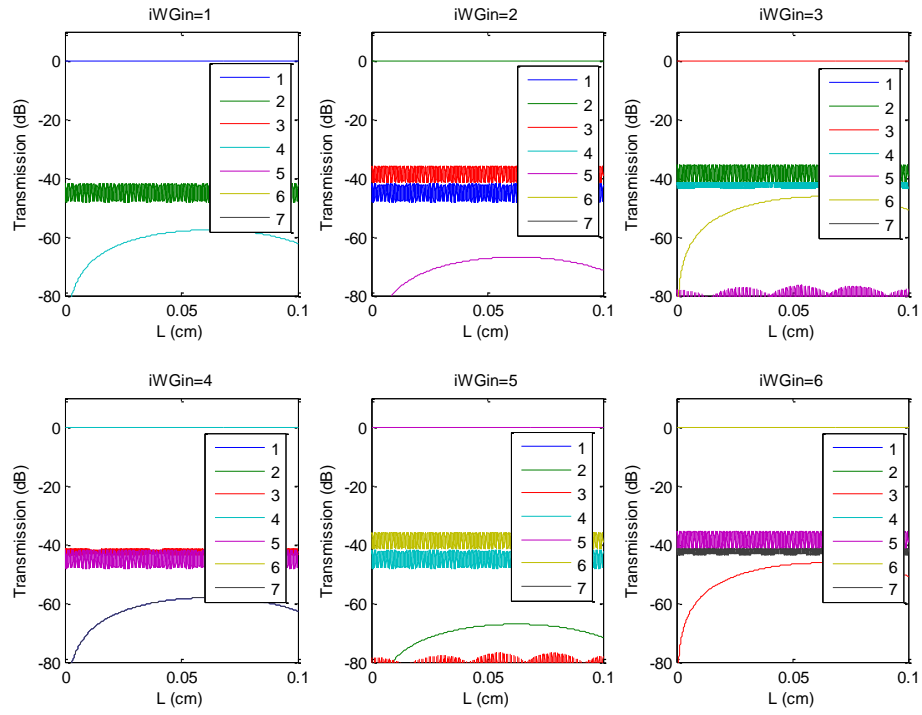


Figure 2. 5 Coupling between waveguides in two unit cells. Each unit cell is composed by waveguides with widths arranged as 450nm-380nm-330nm. The pitch is 1 μ m.

It is evident that the 3-AWA structure shows an overall crosstalk level lower than -35dB. All the sub-plots show that the strongest coupling occurs between adjacent waveguides. And the coupling between identical waveguides is successfully suppressed to the level lower than -40dB. All the other couplings, besides that between the adjacent waveguides and that between identical waveguides, are lower than -75dB which is negligible. In all the cases of consideration, the strongest coupling happens between 380nm-330nm adjacent waveguides. This is due to the relatively weak EM field confinement of these two waveguides. And the same reason leads to the strongest identical waveguides coupling between 330nm-330nm waveguides.

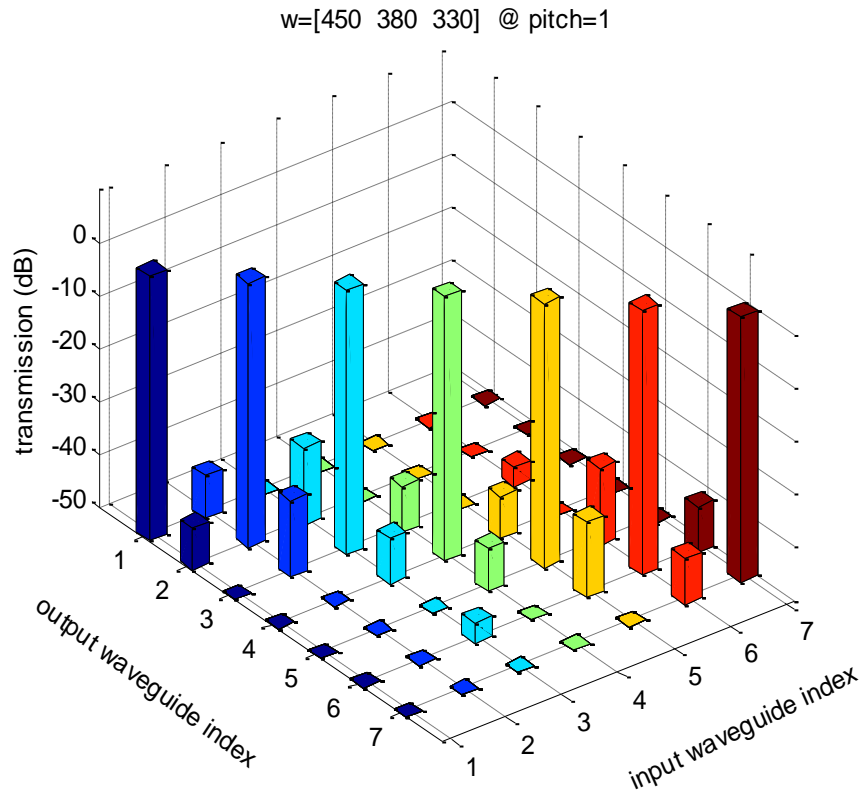


Figure 2. 6 Broadband transmission response of the 3-AWA bus waveguide

To show that the designed AWA structure sustains the low crosstalk level over a broad wavelength range, broadband response of the AWA structure needs to be studied. When monochromatic light is launched into one specific waveguide, for example, WG- N , the power transmission with respect to the propagation length is first calculated as the cases shown in Fig. 2.5. Then the maximum power that can be obtained in each waveguide is extracted and marked as $P_{N,N+1}(\lambda_0)$. By changing the wavelength of the incident light, the maximum-power with respect to different wavelength, $P_{N,N+1}(\lambda)$, is obtained. After that, the maximum value of $P_{N,N+1}(\lambda)$ are extracted to represent the broadband response of the device. In practice, simulating long waveguide propagation over a multitude of wavelengths can be very time-consuming. However, one can easily show that the transmission magnitudes of oscillation peaks and valleys on the wavelength spectra are roughly same as the magnitude of the oscillation peaks and valleys in the transmission versus propagation length as shown in Fig. 2.5. This allows for easy estimation of the maximum crosstalk over a wavelength range. Based on this approach, we extract the peak crosstalk from Fig. 2.5 for each channel and plot them in Fig. 2.6. Evidently, Fig. 2.6 captures the critical characteristics of Fig. 2.5, including the overall crosstalk level lower than -30dB, the strongest couplings occur between adjacent waveguides, and the coupling between identical waveguides are suppressed.

2.3. Fabrication and characterization of the 3-AWA bus waveguides

Bus waveguides based on the 3-AWA structure shown in the last section were fabricated on the SOI platform. The wafer used has a top Si layer with a thickness of 260nm and a buried oxide layer of 2 μ m thick. After the e-beam lithography patterning, dry etching, and resist-stripping discussed in Sec. 1.6, a 2 μ m thick SiO₂ layer was

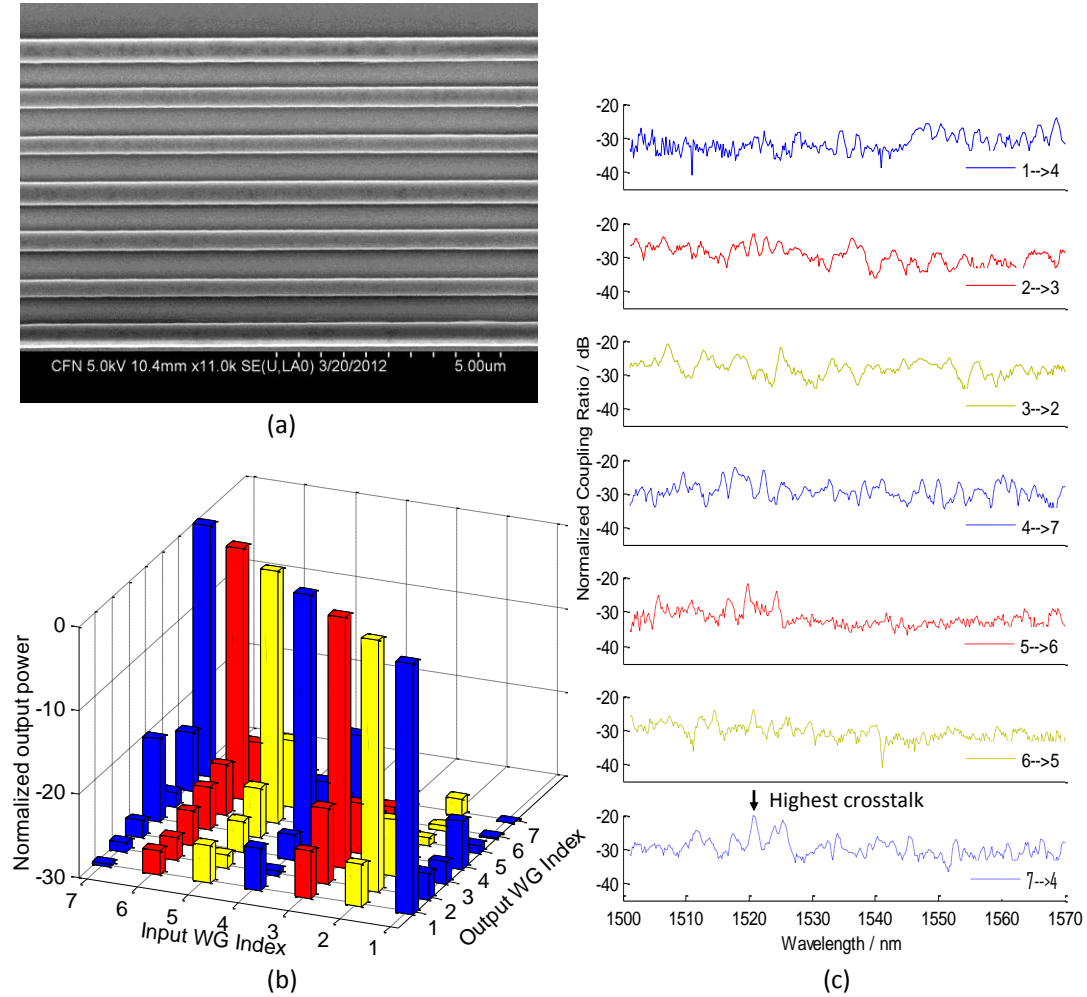


Figure 2. 7 Characterization of the 3-AWA bus waveguides (a) SEM image on the 3-AWA bus waveguide with a pitch size at 1 μm . (b). the broadband response of the bus waveguide array. (c) selected normalized-crosstalk spectra for each input channel.

deposited as the top cladding by the plasma-enhanced-chemical-vapor-deposition (PECVD). After all these processes, samples are cleaved and characterized by the testing stage described in Sec. 1.7. One SEM image on the planar view of the bus waveguides before the deposition of SiO_2 is shown in Fig. 2.7(a).

For the convenience of testing, special designs are added outside the AWA bus waveguide structure. First, the separations between waveguides are gradually increased to 100 μm -scale by bendings with radii around 100 μm (large radii are used to reduce the bending loss). Second, outside the bending structure, tapers are immediately added on both the input and output sides to minimize the propagation loss difference shown by waveguides with different width. Outside the tapers, all the waveguides have the same width at 450nm and this width is kept for all the bus-waveguides used to couple light from-fiber-to-device and vice versa.

A SLED source, centered at $\sim 1538\text{nm}$ with a relatively flat output band over 70nm, was used to characterize the fabricated samples. Each set of the output spectra, corresponding to one specific excited waveguide channel, for example, WG- N , were normalized to the straight-through (WG- $N \rightarrow \text{WG-}N$) spectrum at the output end. Same as in Sec. 2.2, the maximum value of each normalized spectrum was extracted and used to characterize the coupling.

Results are shown in Fig. 2.7(b). Evidently, the overall crosstalk level of the whole system is lower than -20dB. Consistent with the numerical results, the highest crosstalk for each input channel occurred mostly between adjacent waveguides. The crosstalk keeps decaying when waveguides get away from the excited channel. For identical waveguides at the widths of 330nm and 380nm, based on the facilities we have, there is

no evident coupling between them. This confirms that the coupling between identical waveguides can be suppressed by the non-ideal factors of waveguides.

Discrepancies occur on the waveguides with width at 450nm. Theoretically, such waveguides give the best EM field confinements and the least sidewall influence, which should lead to the lowest crosstalk. However, experimentally, they show the highest crosstalk (~ -20.1 dB from WG-7 to WG-4 as shown in Fig. 2.7(c)).

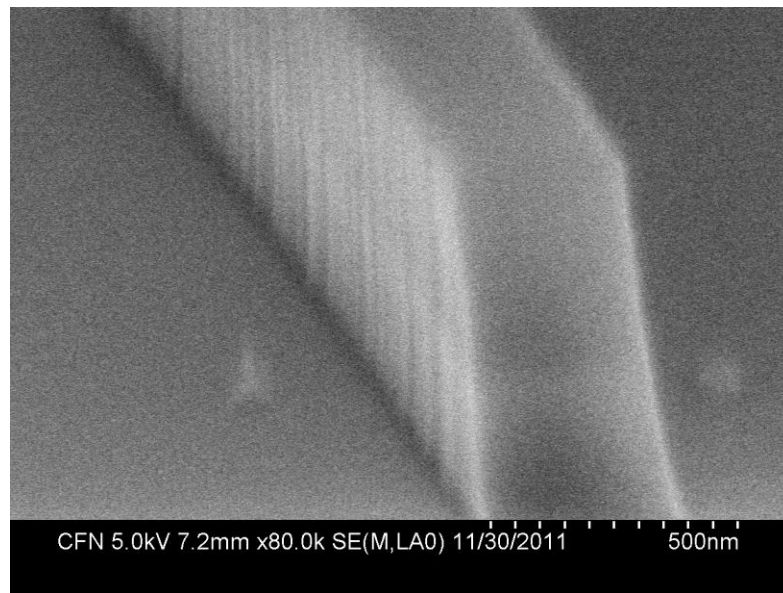


Figure 2. 8 SEM images on sidewall roughness

One possible mechanism that might account for this deviation is the resonant coupling due to the sidewall roughness [45,48]. Study shows that resonant structures, such as gratings, can be used to enhance/reduce waveguides coupling [47]. Unlike the sinusoidal-oscillating spectrum typically shown by evanescent coupling, resonant coupling spectrum shows isolated peaks/valleys in short wavelength ranges. The normalized spectra with the highest crosstalk value for each input channel are plotted in Fig. 2.7(c). From these

spectra, no long-range periodic oscillation or trend is observed, which shows the evanescent-coupling is weak and is covered by other noises. For the highest crosstalk of the whole system, coupling from WG-7 to WG-4 at 1521nm, the spectrum shows a sharp peak with a quality factor (Q) ~ 1900 . SEM image, shown in Fig. 2.8, shows the sidewall roughnesses after the dry-etching process. Certain degree of ordered pattern shows up on the sidewall.

Fig. 2.8 also reveals that the roughness is strongly correlated with the ebeam resist employed. This indicates that the device performance, shown in Fig. 2.7(b), can be improved by optimizing the fabrication processes.

2.4. Performance improvement and discussion

To further increase the integration density and suppress the coupling between identical waveguides, waveguide array with five asymmetric waveguides in one unit cell (5-AWA) is designed. In one 5-AWA cell, waveguides are arranged as: 450nm-380nm-320nm-410nm-350nm. Numerical calculations show that when the pitch equals $0.8\mu\text{m}$, the highest crosstalk of the whole system is $\sim -23\text{dB}$ in the wavelength range of our concern.

High resolution e-beam resist, Hydrogen silsesquioxane (HSQ), was employed to pattern the structure. A SEM image on the cross-section of the sample after dry-etching is shown in Fig. 2.9(a). A top-view on a $2 \times \text{Unit} + 1$ (two unit cells plus one waveguide) structure is shown in Fig. 2.9(b). The 5-AWA bus waveguide with a total length of $500\mu\text{m}$ was characterized by SLED broadband light source ranging from 1480nm to 1580nm and the results are plotted in Fig. 2.9(c).

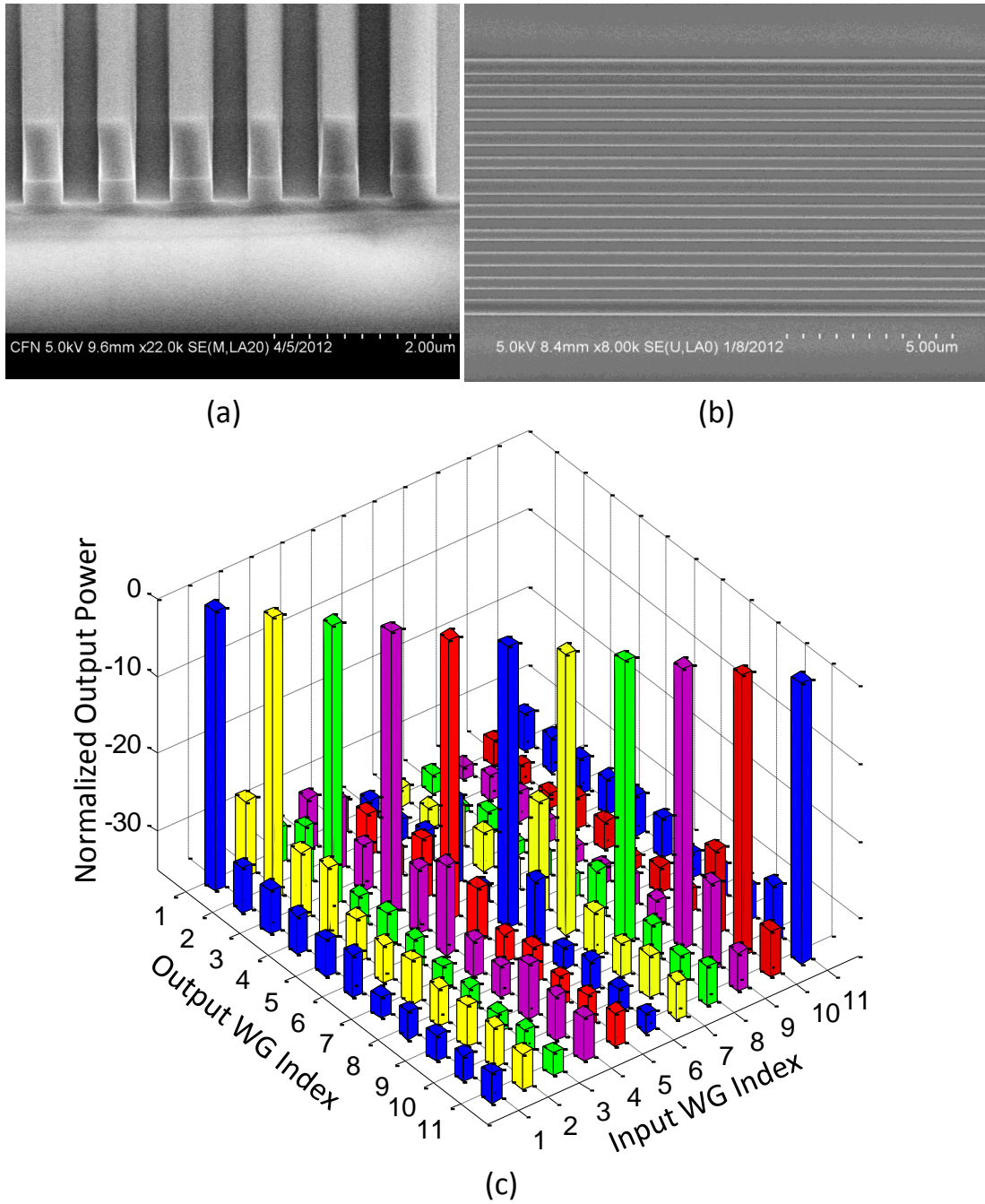


Figure 2. 9 Characterization of the 5-AWA bus waveguide (a) SEM on the cross-section of one unit cell before the coating of cladding. (b) Top view of the waveguide array. (c) Broadband transmission characterization of the 5-AWA structure.

From the results, firstly, the overall crosstalk level of the structure is -21.7dB, better than the targeted -20dB for on-chip communication. Secondly, compared to the results shown by 3-AWA structure with a pitch size at $1\mu\text{m}$, crosstalks between adjacent waveguides are enhanced due to the reduction of both of the low-index gaps and the adjacent waveguides width differences. Thirdly, the strongest couplings occur between adjacent waveguides for all the incident channels except the WG-4 (with a width at 410nm), which may be due to the fabrication imperfections on WG-4. Fourthly, coupling between identical waveguides are successfully suppressed. All of the identical-waveguide coupling are below -29dB (with the strongest one from WG-4 to WG-9, which confirms the imperfection of WG-4).

Robustness in silicon photonics refers to the consistency of the performance of one structure with respect to the fabrication imperfections [28]. Structures with high robustness are always preferred due to the high sensitivity of photonic structures to the device dimension [15]. Study on the robustness of the crosstalk of the AWA structures shows that the device performance varies insignificantly with the changing of the waveguide width. For a same reduction or increase of 10nm on the width of all the waveguides, the crosstalk level is hindered by less than 2dB. Unit cells composed by waveguides with widths other than the one shown in Fig. 2.9(a) were also studied, and characterizations show that the system level crosstalk also lies in a reasonable range. Further studies are necessary to identify the boundary of the waveguides combination that can be employed.

Note that the scattering of light due to the waveguide non-uniformity has two effects. One is the scattering to the radiation modes and backward propagating modes. This leads

to the propagation loss and is taken into account as part of the total loss in the GNNTB model. The other one is the scattering to the confined modes on other lattice sites, which leads to crosstalk. In weakly coupling regime, recent studies on the crosstalk of lossy polymer waveguides [87,88] show that there is a strong correlation between the coupling and the scattering. The coupling is also strongly related with the field distribution of the mode profile. For the waveguide array of our concern, the planar structure, the good confinement, and the discrete nature of the system result in a small contribution of the scattering to the coupling. So it is not taken into account in this model.

It is worthy to note that the linear-indexed waveguide lattice structure has been studied for a while [47]. The main difference is that the typical index difference generated by thermo-optic effect or electro-optic effect is much smaller than the dimension engineered structure studied here. The small index difference leads to a small $\Delta\beta$ between adjacent waveguides, which has little influence on the coupling strength. In fact, in the studies that are not targeting at high density integration, a gradually and smooth modulation is just what required to ensure a high power transmission ratio. However, here, the $\Delta\beta$ is desired to be as large as possible to reduce the power exchange between waveguides.

2.4. Summary

In summary, we proposed and demonstrated a novel, AWA-based design for the high density on-chip integration of bus waveguides. Couplings between asymmetric-waveguide pairs are firstly studied. Results show that, by tuning the waveguide width difference, a crosstalk level lower than -23dB can be achieved at a pitch size of 0.8 μm . Based on the asymmetric-waveguide structure, periodic AWA bus waveguides are designed under the constraints of -20dB system level crosstalk and a sub-micron pitch size.

An overall crosstalk value of -20.1dB with a pitch size at $1\mu\text{m}$ was firstly demonstrated in the 3-AWA structure. After optimizing the fabrication processes and the waveguide arrangement, in the 5-AWA bus waveguides, crosstalk level at -21.7dB was achieved at an integration pitch size as small as $0.8\mu\text{m}$.

Chapter 3 Optical propagation loss properties of PCW

PCWs can slow down light significantly, which has important applications, such as optical switching and modulation [89] and all-optical storage [90]. However, significant optical loss in the slow light regime stymies further advance in this field. Investigations show that the fabrication imperfections, such as shape distortion, structure displacement, sidewall roughness, etc, account for this propagation loss [91-96]. State-of-the-art nanofabrication technology is capable of regulating the distortion and displacement on nanometer-scale. However, it is still a challenging topic to reduce the sidewall roughness. The scattering from a single sidewall irregularity was theoretically studied at first [92]. Then random sidewall roughness with spatial correlation was later introduced to account for loss characteristics in real photonic crystal waveguide structures [95,96]. To get pertinent insight into the loss-generation process, a systematic study should be conducted.

In this chapter, we develop a theoretical framework for calculating PCW scattering loss based on the coupled mode theory in the fixed eigenmode basis. Here we will prove an interesting cross-sectional eigenmode orthogonality relation, which allows us to significantly simplify the coupled mode theory in the fixed eigenmode basis. Assisted by this simplification, analytic loss formulas can be obtained with reasonable assumptions despite the complexity of PCW mode fields. We will introduce the radiation and backscattering loss factors α_1 and α_2 , such that the loss coefficient α can be expressed as $\alpha = \alpha_1 n_g + \alpha_2 n_g^2$, where n_g is the group index. By finding analytic formulas for α_1 and α_2 , and examining their ratio, we show *why* the backscattering loss dominates the radiation loss under fairly general conditions. The analytic study provides further insight into the underpinning physics, such as how the mode-field characteristics (e.g. spatial phase)

interact with roughness to produce loss. The dependences of loss on the structure/roughness parameters are simulated to corroborate the analytic results. Unlike numerical studies that are limited to several instances of structures with specific structure/roughness parameters, this analytic study reveals *general* loss characteristics and fresh insight into the loss-generation process, helping identify new pathways to loss-reduction.

3.1. Propagation loss in PCWs

For an ideal PCW, the confined propagating mode is intrinsically lossless. However, due to fabrication imperfections, light propagation in fabricated PCWs shows significant loss. Experimental and theoretical studies show that there is a strong correlation between the group index, n_g , and the propagating loss. It is found that the basic mechanism is the scattering loss to the backward propagating mode (backscattering loss) and to the radiating modes (radiation loss). Although the scaling of the slow-light loss with respect to the group velocity, v_g , has been examined [91,97-102], it has been difficult to reach a conclusive answer. Theory predicted $1/v_g$ scaling for the radiation loss and $1/v_g^2$ scaling for the backscattering loss [94,95] in the absence of multiple scattering. While experimentalist usually fitted the loss data with a simple power law $v_g^{-\nu}$, where ν was found to vary widely [96,97,103]. To explain these variations, a systematic study is necessary to give a global picture on how the backscattering and radiation losses (and their relative strength) vary with a wide range of structure and roughness parameters commonly used in experiments.

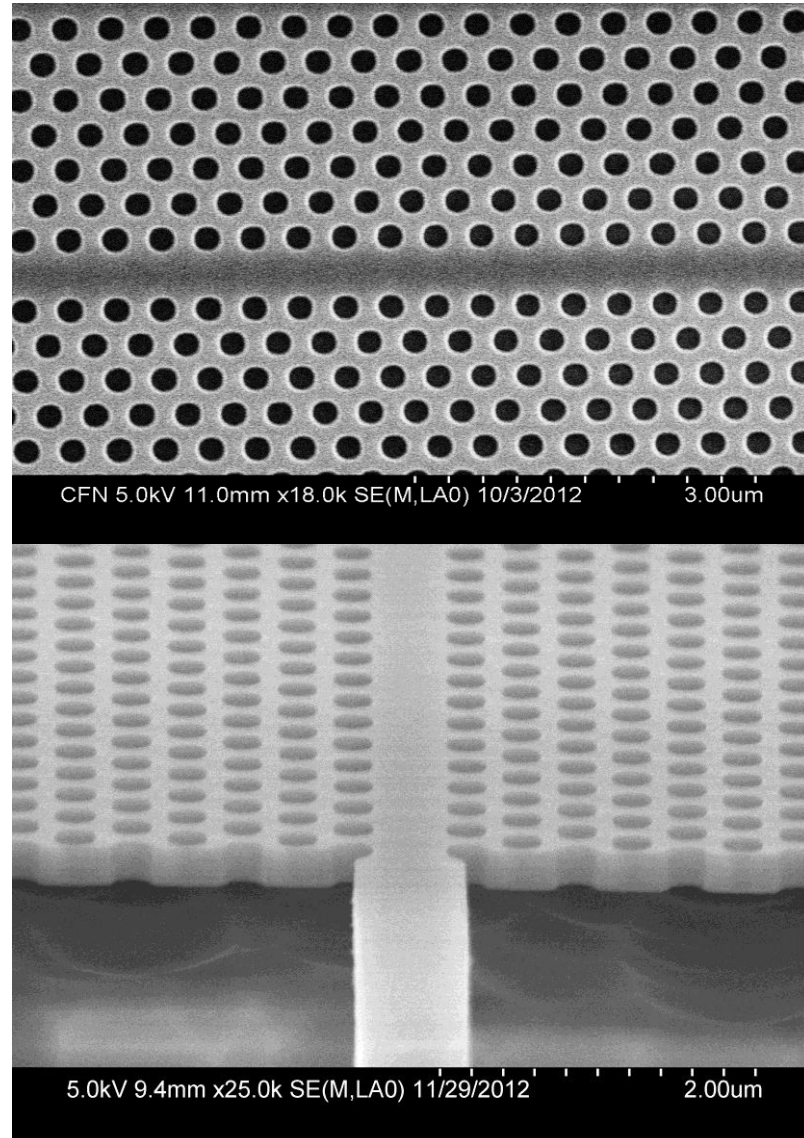


Figure 3. 1 SEM images on the plane view and the cross section of an air-bridge PCW.

3.2. Theory on Scattering Loss

3.2.1. Coupled mode theory and mode orthogonality in a PCW crosssection

The coupled mode theory of a photonic crystal waveguide can be written concisely with Dirac notation. This particular form of coupled mode theory was first developed by Johnson et al. for taper transitions in photonic crystals [104], and was later applied to the disorder-induced scattering problem [98]. The theory can use the fixed eigenmode basis or the instantaneous eigenmode basis. It has the advantage of giving clear dependence of mode coupling on the group velocity through the mode normalization factor.

The differential form of Maxwell's equations can be written as

$$\begin{aligned}\nabla \cdot \mathbf{D} &= \rho & \nabla \times \mathbf{E} &= -\frac{\partial \mathbf{B}}{\partial t} \\ \nabla \cdot \mathbf{B} &= 0 & \nabla \times \mathbf{H} &= \mathbf{J} + \frac{\partial \mathbf{D}}{\partial t}.\end{aligned}\quad (3.1)$$

In the dielectric system of our concern, there is no free charge or current, $\rho=0$ and $\mathbf{J}=0$.

For monochromatic EM waves, the fields can be expressed as:

$$\begin{pmatrix} \mathbf{E}(\mathbf{x}, t) \\ \mathbf{H}(\mathbf{x}, t) \end{pmatrix} = \begin{pmatrix} \mathbf{E}(\mathbf{x}) \\ \mathbf{H}(\mathbf{x}) \end{pmatrix} \exp(-i\omega t). \quad (3.2)$$

Take Eq. 3.2 into Eq. 3.1, the $\frac{\partial}{\partial t} \Rightarrow -i\omega$.

$$\begin{aligned}\nabla \cdot \mathbf{D} &= 0 & \nabla \times \mathbf{E} &= i\omega \mathbf{B} \\ \nabla \cdot \mathbf{B} &= 0 & \nabla \times \mathbf{H} &= -i\omega \mathbf{D}.\end{aligned}\quad (3.3)$$

The Maxwell's Equations can be further simplified by separating the transverse and longitudinal components. Setting

$$\mathbf{E} = \mathbf{E}_t + \mathbf{E}_z, \quad \mathbf{H} = \mathbf{H}_t + \mathbf{H}_z. \quad (3.4)$$

and taking them backing into the Maxwell's Equations, it can be shown that the longitudinal components, \mathbf{E}_z and \mathbf{H}_z , can be expressed by the transverse components, \mathbf{E}_t and \mathbf{H}_t , in the form of [105]

$$\begin{aligned}\mathbf{E}_z &= \frac{ic}{\omega\epsilon} \nabla_t \times \mathbf{H}_t, \\ \mathbf{H}_z &= -\frac{ic}{\omega\mu} \nabla_t \times \mathbf{E}_t.\end{aligned}\quad (3.5)$$

So, the EM field can be completely described by four functions, E_x , E_y , H_x , and H_y . By defining

$$|\psi\rangle = \begin{pmatrix} \mathbf{E}_t(\mathbf{x}) \\ \mathbf{H}_t(\mathbf{x}) \end{pmatrix}, \quad \mathbf{E}_t \equiv \begin{pmatrix} E_x \\ E_y \end{pmatrix}, \quad \mathbf{H}_t \equiv \begin{pmatrix} H_x \\ H_y \end{pmatrix}. \quad (3.6)$$

Maxwell's equations can be rewritten as [104]

$$\hat{A}|\psi\rangle = -i \frac{\partial}{\partial z} \hat{B}|\psi\rangle, \quad (3.7a)$$

$$\hat{A} = \begin{pmatrix} \omega\epsilon - \omega^{-1} \nabla_t \times \mu^{-1} \nabla_t \times & 0 \\ 0 & \omega\mu - \omega^{-1} \nabla_t \times \epsilon^{-1} \nabla_t \times \end{pmatrix}, \quad (3.7b)$$

$$\hat{B} = \begin{pmatrix} 0 & -\hat{\mathbf{z}} \times \\ \hat{\mathbf{z}} \times & 0 \end{pmatrix} = \begin{pmatrix} & & 1 \\ & -1 & \\ -1 & & \\ 1 & & \end{pmatrix}. \quad (3.7c)$$

where $\epsilon(\mathbf{x})$ is the dielectric function, and μ is the permeability.

The system described by Eq. 3.7 is an eigenmode problem. The eigenmodes,

$|\psi_\beta\rangle = e^{i\beta z} |\beta\rangle$, satisfy

$$\hat{C}|\beta\rangle \equiv (\hat{A} + i \frac{\partial}{\partial z} \hat{B})|\beta\rangle = \beta \hat{B}|\beta\rangle. \quad (3.8)$$

Here we consider guided and radiation modes with real β . The inner product is defined as

$$\langle \psi | \hat{B} | \psi' \rangle = \hat{\mathbf{z}} \cdot \int \mathbf{E}_t^* \times \mathbf{H}_t' + \mathbf{E}_t' \times \mathbf{H}_t^* dx dy. \quad (3.9)$$

A rigorous formulation of the coupled mode theory must be established upon a complete set of orthogonal modes [104,106]. For an ordinary waveguide, whose structure is invariant along z , it is straightforward to show that any two eigenmodes at a given frequency ω must be orthogonal [106]

$$\langle \beta | \hat{B} | \beta' \rangle = \eta_\beta \delta_{\beta\beta'}. \quad (3.10)$$

For a PCW periodic along z , solid state theory suggests that the eigenstate orthogonality can be obtained only by further integration along z ,

$$\int e^{i(\beta' - \beta)z} \langle \beta | \hat{B} | \beta' \rangle dz = \eta_{\beta'} \delta_{\beta\beta'}. \quad (3.11)$$

Such an orthogonality relation cannot be directly used in a rigorous PCW coupled mode theory because the modal coupling coefficients also have z -dependence and will appear in the above integral. To overcome this problem, a complicated virtual coordinate theory was previously developed [105].

Here we show that Eq. 3.10 still holds for a PCW in any z -section. By partial integration, one can readily show $\langle \beta | \hat{C} | \beta' \rangle = (\langle \beta' | \hat{C} | \beta \rangle)^* + i \frac{\partial}{\partial z} \langle \beta | \hat{B} | \beta' \rangle$. Therefore,

$$(\beta' - \beta) \langle \beta | \hat{B} | \beta' \rangle = i \frac{\partial}{\partial z} \langle \beta | \hat{B} | \beta' \rangle. \quad (3.12)$$

This is a differential equation of $\langle \beta | \hat{B} | \beta' \rangle_z$ with a solution $\langle \beta | \hat{B} | \beta' \rangle_z = e^{-i(\beta' - \beta)z} \langle \beta | \hat{B} | \beta' \rangle_{z=0}$. However, $\langle \beta | \hat{B} | \beta' \rangle_{z+a} = \langle \beta | \hat{B} | \beta' \rangle_z$ according to Bloch

theorem. Therefore, $\langle \beta | \hat{B} | \beta' \rangle = \eta_\beta \delta_{\beta, \beta' - (2n\pi/a)}$, which gives Eq. 3.10 for β and β' in the first Brillouin zone (1BZ).

The orthogonality relation, Eq. 3.10, for a photonic crystal waveguide is an interesting result. According to the Bloch theorem, the eigenstate orthogonality in a generic 1D-periodic system should be obtained by integrating $\int \psi_b^* \psi_a dz = 0$ along the periodicity direction (z in this case). However, the above proof has shown that if there are multiple eigenstates with different on-axis wavevectors at a given frequency (or photon energy), they must be orthogonal by integrating $\int \psi_b^* \psi_a dx dy$ in any cross-section perpendicular to the periodicity axis. Note an equivalent form of this orthogonality was proved in a different theoretical framework based on the Lorentz reciprocity [107], which is limited to electromagnetic wave. The proof given here is generally valid for any scalar or vector wave satisfying Eq. 3.8.

The coupled mode theory in the fixed eigenmode basis can now be established easily based on Eq. 3.10 for a photonic crystal waveguide. With a potential perturbation $\Delta \hat{A}$, the mode equation becomes

$$(\hat{A} + \Delta \hat{A})|\psi\rangle = -i \frac{\partial}{\partial z} \hat{B}|\psi\rangle, \quad (3.13)$$

where $|\psi\rangle = \sum_n c_n(z) e^{i\beta_n z} |n\rangle$, and $|n\rangle$ are the eigenmodes of the unperturbed system.

The coupled mode theory generally requires to use $\langle m |$ to select c_m for a particular mode from Eq. 3.13. If the conventional orthogonality relation, Eq. 3.11, is applied, the evaluation of $\int \langle m | \frac{\partial}{\partial z} \hat{B} | \psi \rangle dz$ will be problematic because $c_m(z)$ depends on z . With the

orthogonality relation Eq. 3.10, however, it is straightforward to show that the coupling coefficients are governed by the following equation

$$\frac{\partial c_m}{\partial z} = (i/\eta_m) \sum_n e^{i(\beta_n - \beta_m)z} \langle m | \Delta \hat{A} | n \rangle c_n. \quad (3.14)$$

We should emphasize that although it appears similar to the equation for a conventional waveguide homogenous along z , this simplified Eq. 3.14 can be *rigorously* established for a PCW only with the help of Eq. 3.10. This simplification enabled by the cross-sectional orthogonality relation, Eq. 3.10, is the main improvement for the coupled mode theory used in this work. This simplification allows us to derive analytic loss formulas that can be calculated almost by hand, as we shall see in the next section, and provides a clearer physical picture.

3.2.2. Separate calculation of backscattering loss and radiation loss

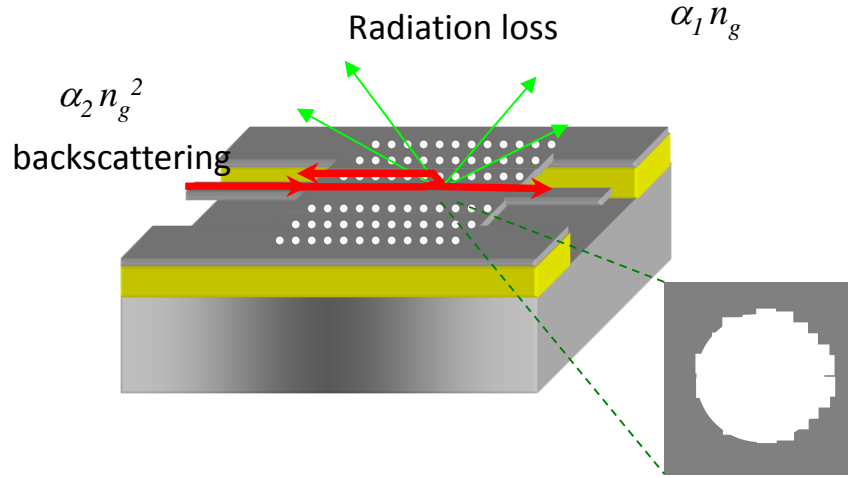


Figure 3. 2 Schematics of the propagation losses in a PCW.

In one specific PCW, the eigenmodes, $|n\rangle$, can be separated into forward propagation modes, backward propagation modes, and radiation modes. The scattering loss can be introduced through a random potential $\Delta\hat{A}$ due to dielectric perturbation $\Delta\epsilon$ and $\Delta(\epsilon^{-1})$ from the ideal structure.

For a frequency range with a single guided mode $|\beta\rangle$, the perturbed mode is given by

$$|\psi\rangle = c_\beta(z)e^{i\beta z}|\beta\rangle + c_{-\beta}(z)e^{-i\beta z}|-\beta\rangle + \sum_k c_k(z)e^{ik_z z}|k\rangle. \quad (3.15)$$

where $|k\rangle$ are radiation modes, and $c_m(z)$, $m=\pm\beta, k$, are the coupling amplitudes. With Eq. 3.10, it is straightforward to solve the coupled mode equations to the first order. For unit input, the output amplitudes are given by

$$c_m = (i/\eta_m) \iiint e^{i(\beta-\beta_m)z} (\Delta\hat{A})_{m\beta} dx dy dz,$$

where $(\Delta\hat{A})_{m\beta} \equiv \phi_m^* \Delta\hat{A} \phi_\beta$, $\phi_m = \langle \mathbf{x} | m \rangle$. The loss coefficient is given by the conservation of the power flux [106]

$$\alpha = (1/L_z) [\langle |c_{-\beta}|^2 \rangle + \sum_k \langle |c_k|^2 \rangle | \eta_k / \eta_\beta |], \quad (3.16)$$

where the ensemble average $\langle \cdot \rangle$ over the random roughness has been applied. To show explicit dependence on the group velocity $v_{g,\beta}$ of mode β , we introduce $U_\beta \equiv \frac{1}{4} |\eta_\beta / v_{g,\beta}|$, the time averaged mode energy per unit length along the z axis. For a radiation mode $|k\rangle$, we define $U_k \equiv \frac{1}{4} |\eta_k / v_{gz,k}|$, where $v_{gz,k}$ is the z -component of $\mathbf{v}_{g,k}$. Then the η_m terms in Eq. 3.16 can be replaced by U_m and v_g . Assuming that the sidewall roughness of different holes is uncorrelated [95], the ensemble averaged α of a PCW is a

sum of the ensemble averaged loss contribution from each hole. For roughness-related calculation, it is more convenient to use the polar coordinates (r, θ) in each hole in place of (x, z) . After some calculations, we find the propagation loss can be written as:

$$\alpha = \alpha_1 n_g + \alpha_2 n_g^2, \quad (3.17a)$$

$$\alpha_1 = (1/a) \sum_k \sum_{n_x} I(k, \beta, n_x) (c/v_{gz,k}) |U_k/U_\beta|, \quad (3.17b)$$

$$\alpha_2 = (1/a) \sum_{n_x} I(-\beta, \beta, n_x). \quad (3.17c)$$

where n_x and n_z are the indices of holes along x and z , respectively (see Fig. 3.3). The PCW has a lattice constant a , mean hole radius r_0 , and slab thickness t_{slab} . The integral for the n_x -th hole is

$$I(m, \beta, n_x) \equiv (r_0 t_{\text{slab}} / 4U_m c)^2 \int_{\Omega_{n_x}} e^{i(\beta - \beta_m) r_0 (\sin \theta - \sin \theta')} \hat{\Delta A}_{m\beta, n_x}^*(\theta') \hat{\Delta A}_{m\beta, n_x}(\theta) \langle \Delta r(\theta') \Delta r(\theta) \rangle d\theta' d\theta, \quad (3.18)$$

where $\hat{\Delta A}_{m\beta, n_x}(\theta) = (1/t_{\text{slab}}) \int \Delta A_{m\beta} \Big|_{r=r_0^+} dy$. A typical autocorrelation function is given by

$\langle \Delta r(\theta') \Delta r(\theta) \rangle = \sigma^2 e^{-|\theta - \theta'| r_0 / l_c}$, where σ and l_c are the rms roughness and correlation length, respectively. Note that the coordinates (r, θ) are centered in each cell Ω_{n_x} .

Now the loss coefficients can be numerically calculated using Eqs. 3.17 and 3.18. Instead of directly calculating the loss coefficient α , we will calculate the radiation and backscattering loss factors α_1 and α_2 . Note that α diverges as the frequency approaches the band edge whereas α_1 and α_2 are *slowly varying functions* even near the band edge. Thus the calculation of α_1 and α_2 generally leads to significantly more stable numerical results than directly calculating α .

Here we consider the TE guided modes (i.e. electric field primarily in the xz plane) of a Si air-bridge PCW. The guided modes can be obtained by a preconditioned eigensolver [108] with a tensorial average of the dielectric constant near interfaces [109]. The perturbation potential is evaluated using the continuous components on interfaces [110].

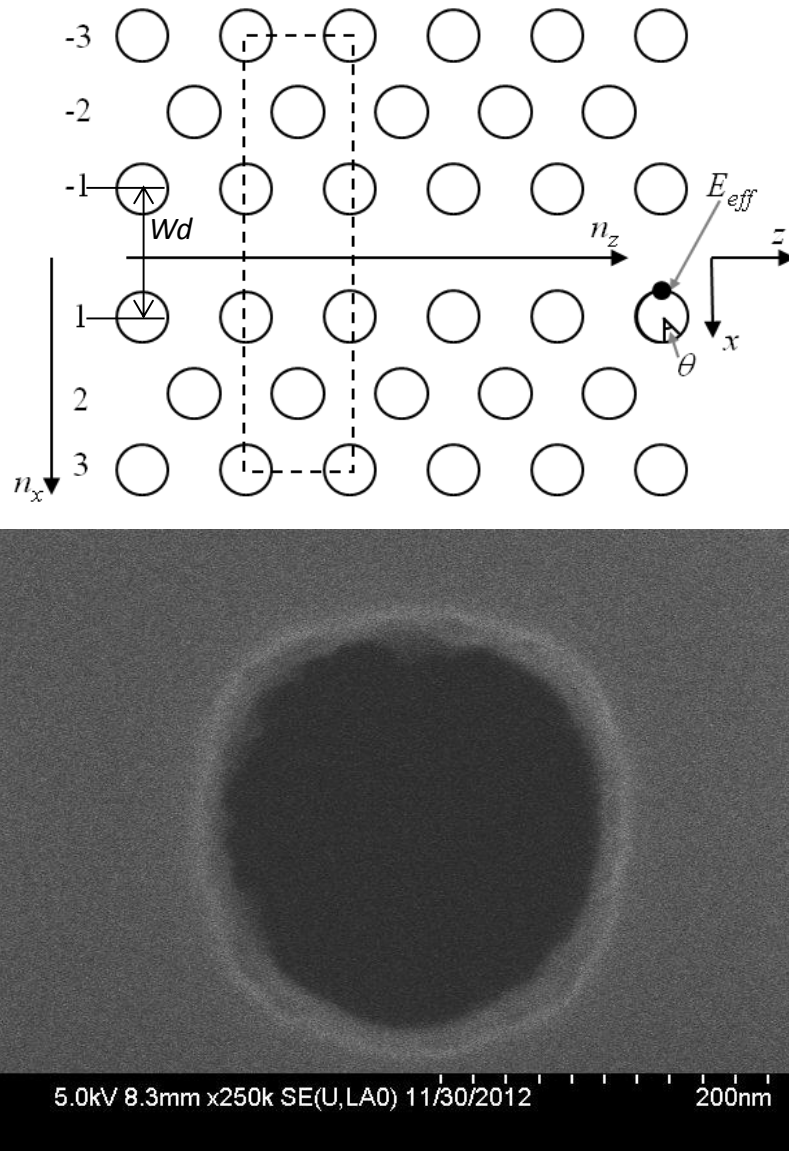


Figure 3. 3 In-plane view of a line-defect PCW (top) and a SEM on one hole of a fabricated PCW (bottom).

The radiation modes are calculated by considering the PCW supercell delineated in dashed lines in Fig. 3.3 (the one used in actual calculation is much longer along x) as one period of a 2D grating in the x - z plane. The mode field for a given plane wave incident upon the PCW top surface can be obtained by any grating diffraction theory [111,112]. Due to the artificial x -periodicity imposed by the grating theory, this treatment is equivalent to calculating the radiation loss for an array of parallel PCWs.

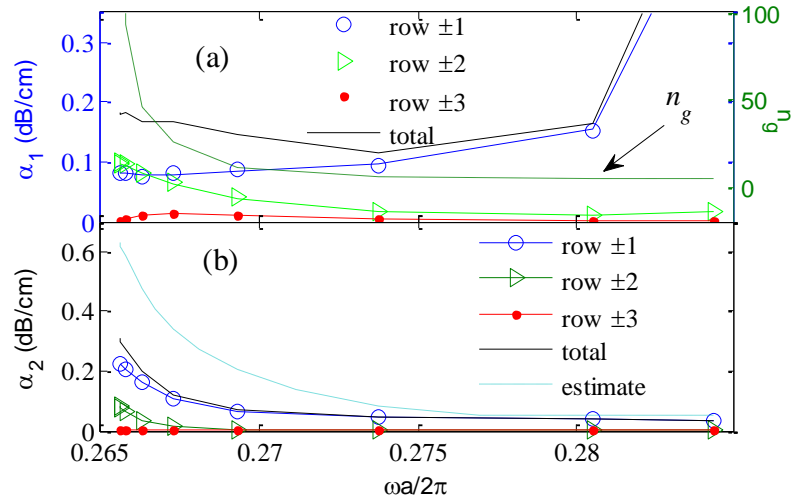


Figure 3. 4 Loss factors as a function of frequency and the contribution from each pair of rows of holes. (a) Radiation loss factor α_1 ; (b) Backscattering factor α_2 and the analytic estimate. PCW parameters: $a=430\text{nm}$, $r_0/a=0.25$, $t_{\text{slab}}=200\text{nm}$, $\sigma=3\text{nm}$, and $l_c=40\text{nm}$.

For a sufficiently large spacing between waveguides, the radiation losses of adjacent waveguides are independent of each other for weak scattering. Fig. 3.4(a) clearly shows that only the first two rows ($n_x=\pm 1, \pm 2$) contribute significantly to the radiation loss. For each row, data plotted in symbols and lines are obtained by two supercell sizes differing by 50%. Their small differences of α_1 confirm that adjacent waveguides do not affect

each other. The backscattering loss shows even stronger dominance by the first row (Fig. 3.4(b)). Obviously, this can be attributed to the fact that the scattering matrix elements $\langle -\beta | \Delta \hat{A} | \beta \rangle$ and $\langle k | \Delta \hat{A} | \beta \rangle$ involve $\phi_\beta(x)$, which decays very fast with x .

3.3. Analytic formulas for backscattering and radiation losses

Interestingly, the factors α_1 and α_2 roughly have the same order of magnitude in Fig. 3.4. As a consequence, the backscattering loss ($\alpha_2 n_g^2$) dominates the radiation loss ($\alpha_1 n_g$), which can be seen from their ratio

$$\frac{\alpha_2 n_g^2}{\alpha_1 n_g} \sim n_g \gg 1 \text{ (for } n_g > 10\text{)}.$$

Numerical simulations of a few other PCW structures showed similar dominance [95,113]. Mathematically, the n_g^2 term surely dominates the n_g term in Eq. 3.17a for a sufficiently large n_g . But the n_g threshold for the onset of this dominance depends on α_1 and α_2 and could be too large to be observed (e.g. $n_g > 1000$). To ascertain the universal dominance of backscattering in practically observable n_g ranges and to explore the underpinning mechanism of this dominance, an *analytic* study is needed. Moreover, such a study may offer insight into the interaction between the mode field and roughness.

We have performed analytic calculation of the factor α_2 with some simple reasonable assumptions. As a first step, we assume a guided mode field of the form $E_\beta \sim e^{-\alpha_x x/2} e^{i\beta x}$.

After some calculation, we find

$$I(-\beta, \beta, n_x) = (\omega r_0 t_{slab} / 4U_m c)^2 (\Delta \varepsilon_{12})^2 |E_{eff, n_x}|^4 \sigma^2 I_{ang}, \quad (3.19)$$

$$I_{ang} = \int e^{i(2\beta r_0)(\sin \theta - \sin \theta') - \alpha_x r_0 (2 + \cos \theta + \cos \theta')} e^{-|\theta - \theta'| r_0 / l_c} d\theta' d\theta,$$

where $\Delta\epsilon_{12}$ is the dielectric constant difference, E_{eff,n_x} is the effective field at the hole's inner edge ($\theta=\pi$ in Fig. 3.3). Typically, the correlation length l_c is small. For $e^{-r_0/l_c} \ll 1$, $\alpha_x l_c \ll 1$, and $2\beta l_c \ll 1$, one finds

$$I_{ang} \approx (4\pi l_c / r_0) \mathcal{J}_0(2\alpha_x r_0), \quad (3.20)$$

where $\mathcal{J}_0(x) = I_0(x)\exp(-x)$ and I_0 is the modified Bessel function of the first kind. One can show that Eq. 3.20 still holds for a more general form of the field $E_\beta \sim e^{-\alpha_x x/2} \sum_G u_G e^{i(\beta+G)z}$ under two scenarios: (1) the mode is dominated by Fourier terms satisfying $Gl_c \ll 1$ so that the phase of each e^{iGz} varies little within one correlation length; (2) near the bandedge where $\phi_\beta(\mathbf{x}) \approx \phi_{-\beta}(\mathbf{x})$. For the second scenario, the phases of $\phi_\beta(\mathbf{x})$ and $\phi_{-\beta}^*(\mathbf{x})$ almost exactly cancel each other in $\langle -\beta | \Delta \hat{A} | \beta \rangle$ and become irrelevant. When these conditions are not satisfied, the spatial phase variations tend to reduce I_{ang} below the value given in Eq. 3.20.

For a guided mode, we can define a modal field amplitude, $\bar{E}_{sp,\beta}$, by $U_\beta = \epsilon_0 \bar{E}_{sp,\beta}^2 w_d t_{slab} / 2$ and normalize the effective field as $e_{eff,\beta} = E_{eff,\beta} / \bar{E}_{sp,\beta}$. Then combining Eqs. 3.17c, 3.19, and 3.20, we obtain

$$\alpha_2 \approx 2N_{x,back} \pi (n_1^2 - n_2^2)^2 (k_0^2 \sigma^2 l_c r_0 / a w_d^2) |e_{eff,\beta}|^4 \mathcal{J}_0(2\alpha_x r_0), \quad (3.21)$$

where $k_0 = 2\pi/\lambda$, $n_1^2 - n_2^2 = \Delta\epsilon_{12} / \epsilon_0$, and $2N_{x,back}$ is the *effective* number of rows of holes contributing to backscattering. For numerical estimate, we assume $N_{x,back} \approx 1$, $w_d = w_0 \equiv \sqrt{3}a$. In addition, $E_{eff,\beta}$ is obtained by averaging $|E_\beta|^2$ at the inner hole edge across the slab thickness. We find that $e_{eff,\beta}$ typically varies around 0.3~0.4 in the slow

light regime. The decay constant $\alpha_x \approx 0.77(2\pi/a)$ is obtained by fitting the mode energy against x near the band edge. Note $\mathcal{J}_0(2\alpha_x r_0)$ is a slowly varying function for this parameter range of interest. Figure 3.4(b) shows that Eq. 3.21 gives a reasonable estimate of the order of magnitude of α_2 and its trend. There is an overestimate of 2 to 3 times because we have neglected the following factors: (a) the vector nature of the field; (b) the high- G Fourier components; (c) the variation of the field along y .

For the radiation modes, considering two polarizations ($\mu=1,2$) and two propagation directions ($s_z=\pm z$), the sum over k in Eq. 3.17b becomes $\sum_k \rightarrow \sum_{\mu, s_z} \frac{L_x L_y}{(2\pi)^2} \int dk_x dk_y$, where L_x and L_y are the transverse dimensions of the normalization volume. Note the final result of α_1 is independent of $L_x L_y$ because $I(k, \beta, n_x) \cdot |U_k| \sim (L_x L_y)^{-1}$ in Eq. 3.17b. One can then show that

$$\alpha_1 \approx 2N_{x,rad}(n_1^2 - n_2^2)^2 n_{sub}^3 (k_0^4 \sigma^2 l_c r_0 t_{slab} / a w_d) |e_{eff,\beta} \bar{e}_{eff,k}|^2 \mathcal{J}_0(\alpha_x r_0). \quad (3.22)$$

where $\bar{e}_{eff,k}$ is the normalized field amplitude at the hole inner edge averaged over all k states, $n_{sub}=1$ is the substrate refractive index, and $2N_{x,rad}$ is the *effective* number of rows of holes contributing to radiation loss. Comparing Eq. 3.21 and Eq. 3.22, we find

$$\frac{\alpha_1}{\alpha_2} \approx \frac{N_{x,rad} n_{sub}^3 k_0^2 w_d t_{slab}}{\pi N_{x,back}} \cdot \frac{|\bar{e}_{eff,k}|^2}{|e_{eff,\beta}|^2} \cdot \frac{\mathcal{J}_0(\alpha_x r_0)}{\mathcal{J}_0(2\alpha_x r_0)}. \quad (3.23)$$

With $N_{x,rad}, N_{x,back} = 1 \sim 2$, $w_d = w_0$, $t_{slab} \sim 220\text{nm}$, $\alpha_x \sim 0.5(2\pi/a)$, and normalized fields $e_{eff,\beta}, \bar{e}_{eff,k} \sim 0.5$, each ratio in Eq. 3.23 is on the order of unity. This equation therefore predicts that α_1 and α_2 are *generally* on the same order. Therefore, this analytic study explains *why* the backscattering *generally* dominates, $\alpha_2 n_g^2 \gg \alpha_1 n_g$, in the slow

light regime $n_g \geq 10$. Note that Eqs. 3.21 and 3.22 contain no fast-varying functions, which implies that α_1 and α_2 should be fairly insensitive to most structure parameters for a typical PCW.

Note that prior scattering loss formulas still involve the photonic crystal mode field and the Green's function [95], which must be obtained through further computation. Our analytic loss formulas, Eqs. 3.17a, 3.21 and 3.22, do not have these terms, and can be evaluated almost by hand. More importantly, the ratio of α_1 and α_2 derived from these formulas, as presented in Eq. 3.23, gives a *general mathematical* proof of the dominance of the backscattering loss over the radiation loss, along with a predicted dominance threshold $n_g \sim 10$. Prior numerical studies discovered this dominance in a limited number of structures with specific parameters [95,113]. However, the generality of the dominance and its threshold n_g were not clearly determined in numerical studies.

3.4 Comparison with experiments

In Fig. 3.5, we compare with experimental results from Ref. [96] using $\sigma=3\text{nm}$ and $l_c=40\text{nm}$ suggested therein. Evidently, our theory agrees well with experiments for $\tilde{\omega} < 0.273$, including the up-swing of the $\alpha/n_g^2 (\approx \alpha_2)$ curve near the band edge. This can be partially explained by the fact that the integral of the guided mode intensity $|E_{\beta}(\mathbf{x})|^2$ over the hole surface increases with the group index [114]. A full explanation must be based on the characteristics of the random potential matrix element $\langle -\beta | \hat{\Delta} | \beta \rangle$, which will be discussed in the following section. Because α_1 and α_2 are not constant *in general*, a simple power law fitting $\alpha \sim n_g^\nu$ of experimental data would unlikely give consistent ν

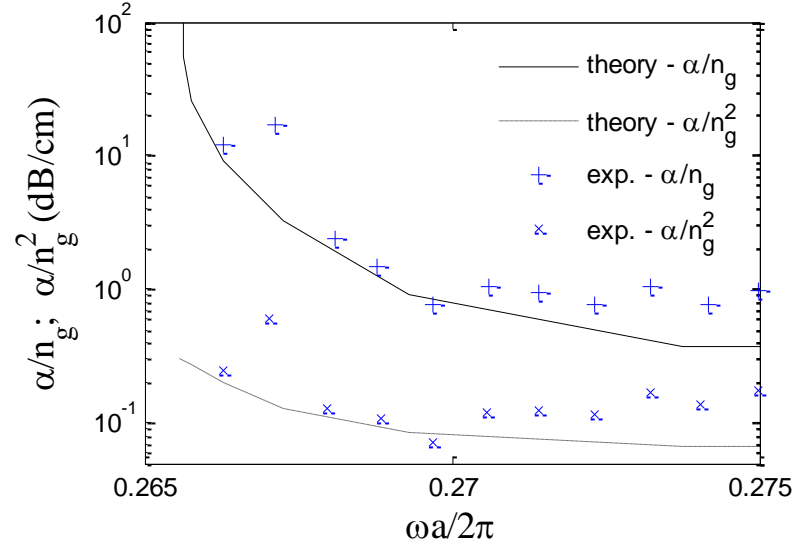


Figure 3. 5 Comparison of the analytic formula with experimental results in Ref. [96].

The experimental spectrum is shifted to align the bandedge with the theory.

values, which agrees with the findings of Ref. [114]. Note that if the coupling loss [115] is included, the $loss-n_g$ relation could even become sub-linear (or logarithmic), especially for short waveguides. Above $\tilde{\omega} = \omega a / 2\pi c = 0.273$, the localized bandtail states [108,116] of the second guided mode (bandedge $\tilde{\omega} \approx 0.281$) introduce in the experimental spectrum a broad resonance accompanied by a “softened” v_g at the nominal bandedge [117]. This effect is beyond the scope of this study. Fortunately, this effect can be avoided by designing the second mode above the useful spectral range of the first mode. Below a sufficiently small v_g , multiple-scattering occurs for the first mode, accompanied by undesirably high loss. The studies presented here could help reduce scattering losses and delay the onset of this regime.

3.5 Loss dependence on structure and roughness parameters and loss reduction strategies

As the backscattering loss dominates, we focus on the dependences of α_2 on several key roughness/structure parameters. The tensorial average technique used to calculate the dielectric function near interfaces is found to significantly improve the convergence with the spatial grid size, as shown in Fig. 3.6(a). This allows us to study small structure parameter changes. First, we examine the limitation of the preceding analytic results due to the assumption of small l_c . The dependences of α_2 on l_c for various normalized β values are plotted in Fig. 3.6(b). For guided modes near the band edge ($\beta a/2\pi \sim 0.5$), $\alpha_2(l_c)$ is almost perfectly linear. As discussed above, this linearity predicted in Eq. 3.21

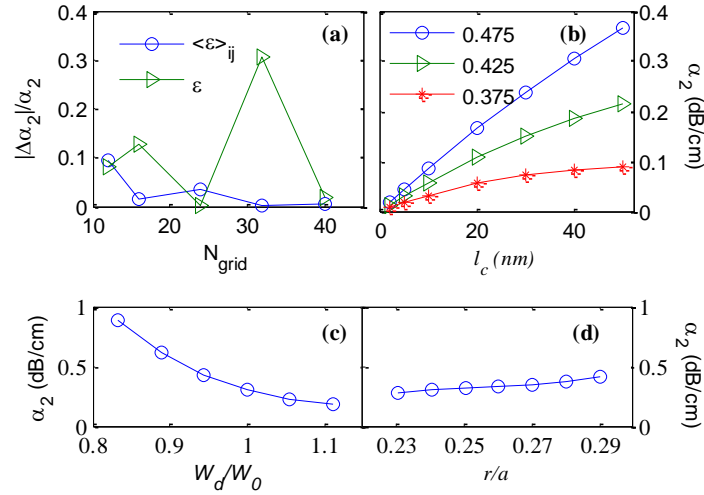


Figure 3. 6 Variation of α_2 with (a) grid size per edge of the unit cell, with tensorial average $\langle\epsilon\rangle_{ij}$ and without (up to 30% oscillation); (b) correlation length l_c , for modes at different $\beta a/2\pi$, (c) PCW width; and (d) hole radius. PCW parameters: $a=420\text{nm}$, $r_0/a=0.25$, $t_{\text{slab}}=220\text{nm}$, $\sigma=3\text{nm}$, and $l_c=40\text{nm}$.

is due to $\phi_\beta(x) \approx \phi_{-\beta}(x)$ near the bandedge, which causes phase cancellation in $\langle -\beta | \Delta \hat{A} | \beta \rangle$. Away from the bandedge, the phase variation causes the integral I_{ang} to become sub-linear at large l_c values (but Eqs. 3.21 and 3.22 remain useful as estimates), which is also confirmed in Fig. 3.6(b). Second, the dependence on the waveguide width is studied in Fig. 3.6(c). The loss factor α_2 could be reduced by a factor about 5 from $w_d=0.83w_0$ to $1.1w_0$ near the mode edge. Third, in most experimental works, the air hole diameter and slab thickness usually spread over certain ranges (e.g. r_0/a : 0.23~0.29, t_{slab} : 0.19~0.25 μm) and the exact values may vary due to uncertainties in fabrication processes. Our simulations show that α_2 varies insignificantly over the typical ranges of a , r_0 , and t_{slab} . The variation of α_2 ($\beta a / 2\pi \sim 0.5$) is plotted against r_0/a in Fig. 3.6(d).

The analytic and computational studies offer insight into the loss mechanism and point to promising pathways to loss reduction. First, among four essential geometric parameters (r , a , t_{slab} , w_d), w_d appears to be the *only* one that allows for substantial loss reduction. Second, the spatial phase analysis in the derivation of Eq. 3.21 suggests that designing guided modes with accentuated high-wavenumber Fourier components might help reduce the loss due to *random* roughness. As shown in Fig. 3.6(b), the phase cancellation in $\langle -\beta | \Delta \hat{A} | \beta \rangle$ causes an increase of I_{ang} and α_2 near the bandedge. Due to the interplay between the spatial phase of the mode and the roughness, this upswing is stronger for larger correlation lengths. But the eigenfrequency and other *deterministic* characteristics of such a mode also tend to be sensitive to the variations of structure parameters (mean value). Thus, ingenious designs are needed to account for both statistical and deterministic properties. Third, manipulating the polarization, through

introducing anisotropic materials for example, could yield loss much lower than that predicted in Eq. 3.21, which neglects the polarization. Lastly, Eqs. 3.21-3.22 and the spatial phase analysis may offer new insight into the mode shaping effect [117].

In this section, we have considered loss introduced by guided and radiation modes with real β values. In a non-perturbed photonic crystal structure (including a PCW), modes with complex β values generally arise locally near the end-faces and affect the end-face coupling loss [118] but not the propagation loss of a truly guided mode. The propagation loss is generally more important for a sufficiently long photonic crystal waveguide. Also within the photonic bandgap of a PCW, those modes with complex β values usually do not carry away energy themselves and thus may not introduce propagation loss directly. Some higher order (multiple) scattering processes in a PCW with random perturbations may involve these modes as an intermediate step. These multiple scattering processes are usually negligible in practically useful (relatively low loss) spectral ranges of photonic crystal waveguides, as discussed in the comparison with experimental data above.

3.6 Summary

In summary, we developed an analytic theory to study the roughness induced scattering loss in photonic crystal waveguides. Analytic formulas of the PCW scattering losses can be obtained despite the complexity of the PCW mode fields. With these formulas, the loss of a typical photonic crystal waveguide can be estimated by hand. By separately calculating the backscattering loss and radiation loss, we proved that, in slow light region, the backscattering loss dominates. The analytic study reveals that the interplay between the mode characteristics and the structure roughness may hold the key

to loss reduction. These results are corroborated by systematic simulations with varying structure parameters. As a byproduct, the cross-sectional eigenmode orthogonality relation for a 1D periodic system may be applicable to other problems, such as electrons in a polymer chain or a nanowire.

Chapter 4 Influence of substrate on PCW thermo-optic devices

The thermo-optic (TO) effect is an attractive option to implement high power efficiency photonic circuit tuning, optical switches and tunable delay lines if high speed is not a requirement, because it avoids free carrier absorption of light that is present in the electro-optic devices. Furthermore, understanding of the TO effect also helps in the design of silicon electro-optic modulators because the current flow associated with carrier movement is usually accompanied by heat generation [119]. The incorporation of photonic crystal (PC) structures in these devices results in significant reduction of the interaction length due to the slow light effect [119-125]. Ultra-compact optical switches and modulators utilizing different PC structures have been widely studied recently.

A thermo-optic PC device is based on the principle that the temperature variation in the structure induces a change of its refractive index, which in turn leads to a phase shift and a time delay for an optical signal. In an SOI PC structure, the total temperature rise (and thus the total phase shift or time delay) comprises contributions from the temperature rise across the oxide layer as well as that in the substrate. In prior simulations and theoretical studies, the substrate effect is usually assumed to be small and only a relatively thin substrate layer (e.g. $<20\mu\text{m}$) is included in simulations [121]. The effect of a full substrate (e.g. $\sim 500\mu\text{m}$ in actual SOI wafers) has not been studied. In this chapter, we investigate the influence of the substrate as a function of a number of key physical parameters such as the heater length, the substrate thickness (t_{sub}) and the thickness of the buried oxide layer (t_{ox}). Our work reveals some important aspects/scenarios in which the influence of the substrate can be surprisingly high and cannot be neglected in device design. As numerical simulation of a full substrate can be extremely time-consuming, we

have developed a semi-analytic theory that can be used for quick assessment of the substrate effect in thermo-optic device design. Guided by this theory, strategies of minimizing the influence of the substrate will be discussed.

4.1 Model used for multi-scale device

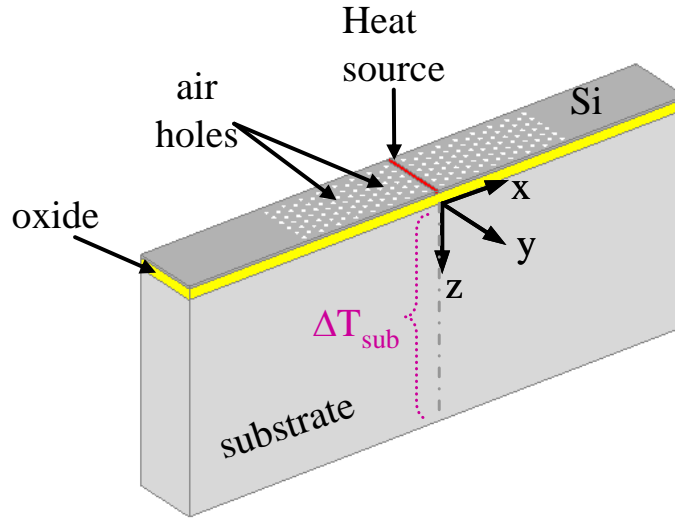


Figure 4. 1 Schematic configuration of an active silicon photonic crystal waveguide structure based on SOI platform (not drawn to scale) [126].

The schematic device structure studied is shown in Fig. 4.1 [126]. It comprises an active PC structure on an SOI wafer with a heat source of width W and length L embedded in the core of the photonic crystal waveguide (PCW). The heat source can be constructed from a lightly doped (e.g. $\sim 10^{14} \text{ cm}^{-3}$) Si strip surrounded by relatively highly doped (e.g. $\sim 10^{17} \text{ cm}^{-3}$) silicon on both sides [66,125]. Concentrated ohmic heating can be produced in the center strip by passing current laterally through this structure.

For a thermo-optic PC device based on the SOI platform, it is typically composed by structures scaling over several magnitudes. For example, the hole radius of the PC is

usually $\sim 200\text{nm}$, the thickness of the buried oxide layer is on the order of $1\mu\text{m}$, the device length is on the order of $100\mu\text{m}$, and the substrate thickness is $\sim 500\mu\text{m}$. Such a multi-scale property makes it challenging to accurately simulate the thermal response of the device. Due to the limitation on computing resources, all the simulations are performed under some simplification, such as assuming the substrate has little influence and using a $20\mu\text{m}$ thick substrate [121,124], assuming the structure is infinitely periodic along the waveguide and simulating just one or several periods of the PC structure along the waveguide [125].

Our previous work developed an efficient method to study the thermo-optic PC devices. In the model, due to the high thermal conductivity of silicon, the heat conduction in the top silicon PC structure can be effectively modeled by that of a homogeneous slab with an effective thermal conductivity κ_{eff} . As shown in Fig 4.2, the temperature distribution along the transverse direction in the top PC layer outside the heater can be expressed as [125]

$$T \approx \exp[-(|x| - W/2) / X_{spr}(r)], \quad \text{for } |x| > W/2 \quad (4.1)$$

here, $X_{spr}(r)$ is the thermal spreading length, which can be expressed as

$$X_{spr} = (t_{Si} t_{Ox} \kappa_{eff} / \kappa_{Ox})^{1/2} \quad (4.2)$$

where t_{Si} is the thickness of the top Si layer, t_{Ox} and κ_{Ox} are the thickness and the thermal conductivity of the buried oxide layer. Both X_{spr} and κ_{eff} are functions of the hole radius and can be determined empirically. For a PC with the hexagonal lattice which has a lattice constant $a = 400\text{nm}$, $t_{Si} = 250\text{nm}$, and $t_{Ox} = 2\mu\text{m}$, corresponding values of X_{spr} and κ_{eff}/κ_{Si} are shown in Table 4.1.

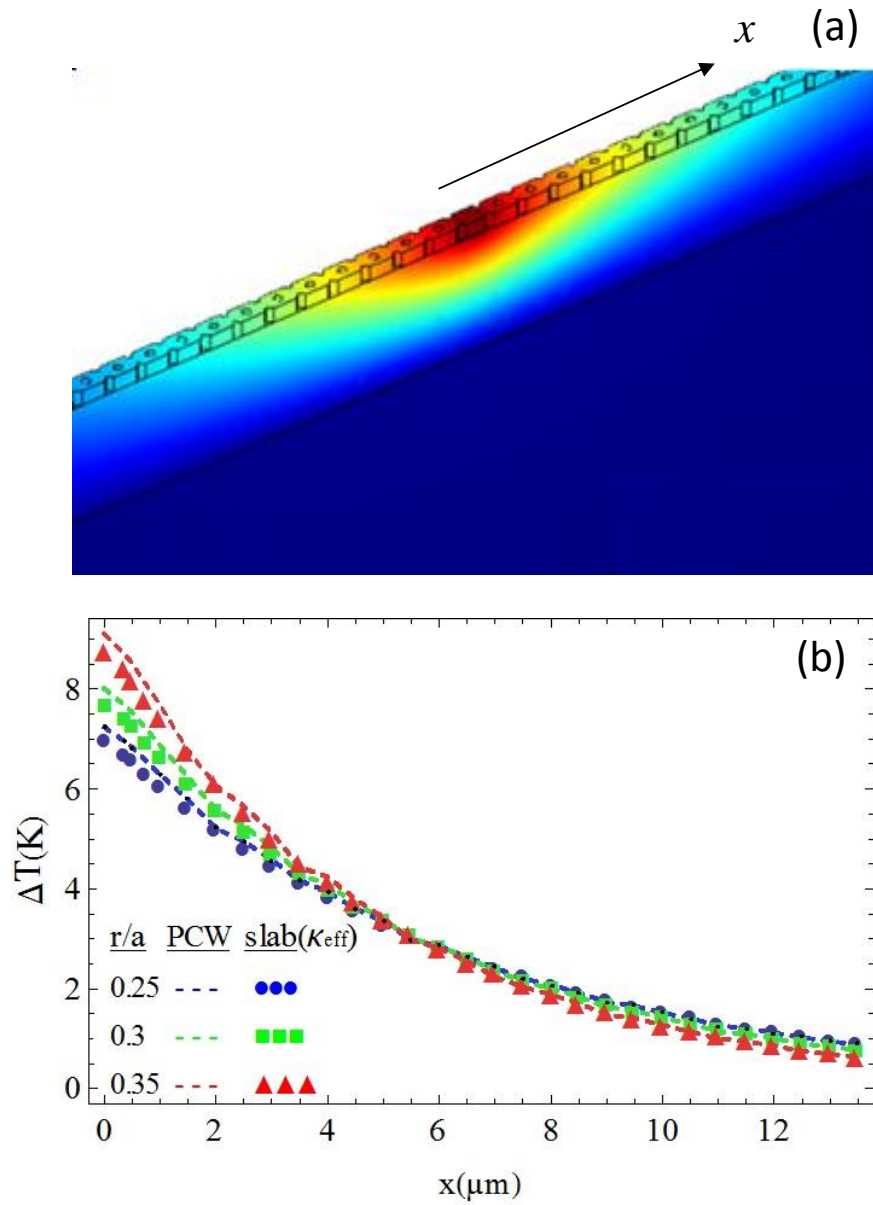


Figure 4. 2 Temperature distribution in the top silicon PC layer. (a). Temperature distribution for a PCW with $r/a=0.25$. Periodic boundary condition is used to simplify the simulation. (b). Temperature profiles along the transverse direction in the top Si layer of PCWs with various hole radii and that with homogenized slab model [125].

Table 4. 1 Empirically values of X_{spr} and $\kappa_{eff} / \kappa_{Si}$ for different hole size [125]

r / a	0.25	0.275	0.3	0.325	0.35
$X_{spr} (\mu\text{m})$	6.3	6.0	5.7	5.3	4.9
$\kappa_{eff} / \kappa_{Si}$	0.68	0.61	0.55	0.48	0.41

By utilizing this effective thermal conductivity κ_{eff} , it becomes possible to simulate the thermal response of a PC device with a full substrate thickness of 500 μm . A typical 3-D steady state FEM simulation result is shown in Fig. 4.3(a). The bottom surface of the device is kept at $T_0=300$ K to emulate a heat sink under the substrate. Because the heat dissipation from the top and side surfaces is negligible due to the small thermal conductivity [127] and a small heat transfer coefficient in natural convection of air [128], adiabatic boundary conditions are used for these surfaces [124,125]. The values of the thermal conductivities of silicon (κ_{Si}), silicon oxide (κ_{ox}) and photonic crystal κ_{eff} are taken from our previous work [125].

4.3 Analogy between steady heat conduction and electrostatics problems

To avoid the cumbersome Fourier-transform, which is commonly used in solving the heat transfer problems, and simplify the calculation, it is helpful to conduct an analogy between the heat conduction and the electrostatics. From the electromagnetic field theory, an electrostatic field can be fully described by two differential equations [129]:

$$\nabla \cdot \mathbf{D} = \rho, \text{ and } \nabla \times \mathbf{E} = 0, \quad (4.3)$$

where $\mathbf{D} = \epsilon(\mathbf{r})\mathbf{E}$. ϵ is the permittivity of the material.

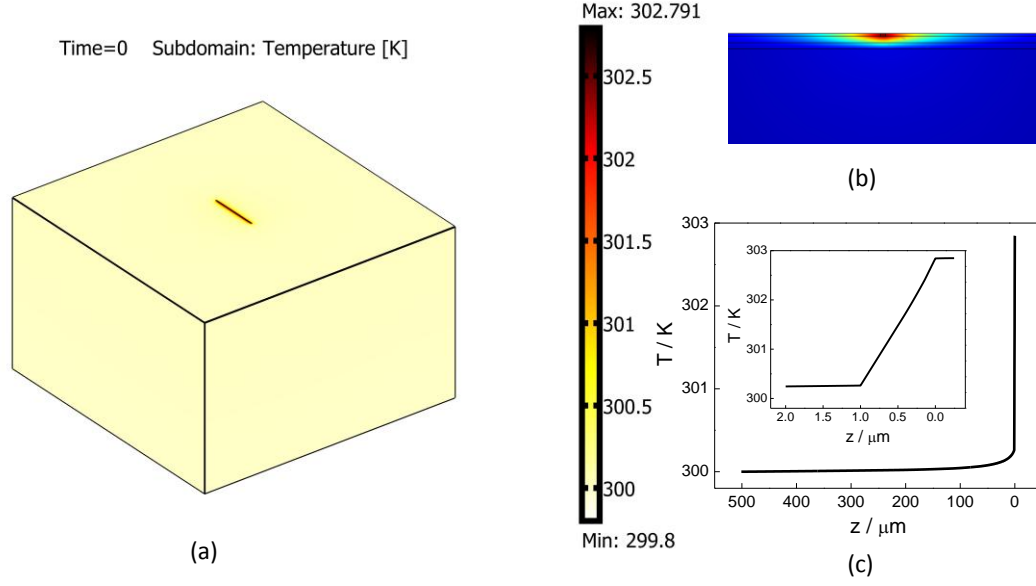


Figure 4. 3 A typical steady state simulation result with a full substrate thickness. (a) A typical structure and steady state 3-D FEM simulation result for a simulation area of $800\mu m \times 800\mu m$ with $t_{Si}=250nm$, $t_{ox}=2\mu m$, $t_{sub}=500\mu m$, $L=150\mu m$, and $W=400nm$. The power of the heater is set as 5mW. The corresponding photonic crystal structure has a hole radius $r=0.25a$, where $a=400nm$ is the lattice constant. (b) Zoomed in cross-section around the center part of the heater. (c) Temperature distribution below the center of the heater.

These equations can be combined into one partial differential equation by defining the scalar potential $\Phi(\mathbf{r})$. For linear, isotropic, homogeneous medium, where ε is a constant, it can be expressed as Poisson's Equation [129]:

$$\nabla^2\Phi = -\rho/\varepsilon, \text{ where } \mathbf{E} = -\nabla\Phi \quad (4.4)$$

Similarly, for the problem of a steady-state temperature system, the heat conduction can be characterized as [130,131]:

$$\nabla \cdot \mathbf{q} = A, \text{ and } \mathbf{q} = -\kappa \nabla T \quad (4.5)$$

where q is the flow rate of heating energy, A is the heating power density, T is the temperature distribution, and κ is the thermal conductivity. For thermally linear, isotropic, homogeneous medium, they can also be written in the form of the Poisson's Equation:

$$\nabla^2 T = -A/\kappa \quad (4.6)$$

By comparing these equations, it is evident that the steady state heat conduction equation resembles the static electric field equation. For the key components, κ plays the role of the local permittivity, T the potential, and A the external charge density [132]. This analogy makes it possible to infer the solutions of the steady-state heat conduction problems from the known results in electrostatics [131].

4.4 Simulation and Analytic Results

4.4.1 Semi-analytical model and a comparison with FEM simulation results

To gain insight into heat conduction in the substrate and develop a semi-analytic model, we first consider the effective cross-sectional area (in the x - y plane) of the vertical

heat flux, and then utilize the electric field analogy to obtain the vertical temperature profile in the substrate.

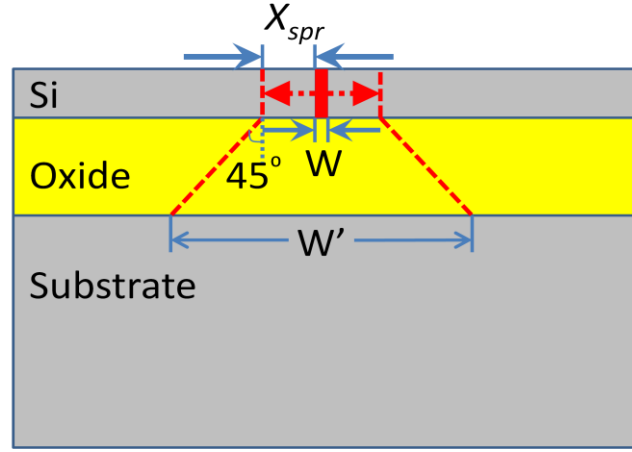


Figure 4. 4 schematics of the heat spreading model in the cross section of the TO PC device.

Our previous work [125] showed that the heat flux on the top surface of the buried oxide layer has an effective width of $W+2X_{spr}$ due to the lateral thermal spreading in the silicon PCW cladding, where X_{spr} is given by $X_{spr} = \sqrt{t_{Si}t_{ox}K_{eff}/K_{ox}}$ and t_{Si} is the thickness of the top Si layer. As the heat flows down through the oxide layer, it also spreads laterally. With a fixed-angle heat spreading model [133,134], we can readily show that the effective width and length of the heat flux cross-section are increased by $\Delta W=\Delta L=2t_{ox}\tan 45^\circ$ after passing through the oxide layer and reaching the top surface of the substrate. A schematic diagram of the cross-section of this model is shown as the Fig. 4.4. On the top surface of the substrate, the effective heat flux cross-section has the dimensions of

$$W' = (W+2X_{spr}+2t_{ox}) \text{ and } L' = (L+2t_{ox}). \quad (4.7)$$

here, L' doesn't contain the $2X_{spr}$ part due to the limited PCW length. Using the above effective width and length of the heat flux at the top surface of the substrate, the temperature distribution in the substrate can be modeled separately using an electric field analogy. In electrostatics, the potential drop along the z -axis due to a finite sheet of charge uniformly distributed on the x - y plane and centered at the origin is given by [135]

$$V(z) - V(0) = -\int_0^z \frac{\rho_s}{\pi\epsilon} \arctan \left[\frac{(L/2)(W/2)}{z' \sqrt{(L/2)^2 + (W/2)^2 + z'^2}} \right] dz', \quad (4.8)$$

where ρ_s is the external charge density, ϵ is the permittivity, and W and L are the width and length of the charge sheet. By the thermal-electrical analogy shown above, it can readily be shown that for a similar heat source of width W' and length L' , the temperature profile along the z -axis in a semi-infinite ($z > 0$) homogeneous medium is given by

$$T(z) - T(0) = -\frac{2Q/W'L'}{\pi\kappa} \int_0^z \arctan \left[\frac{(L'/2)(W'/2)}{z' \sqrt{(L'/2)^2 + (W'/2)^2 + z'^2}} \right] dz', \quad (4.9)$$

where Q is the power of the source, and κ is the thermal conductivity of the medium. Note the z axis points downward and $z=0$ is assumed to be on the top surface of the substrate. The factor 2 is due to the semi-infinite medium (the mirror image of the half space of $z > 0$ in the other half space of $z < 0$ that will add a source at $z=0^-$ so that this half space problem corresponds to a full space problem with a source of $2Q$). The integration in Eq. 4.9 has a fairly lengthy result,

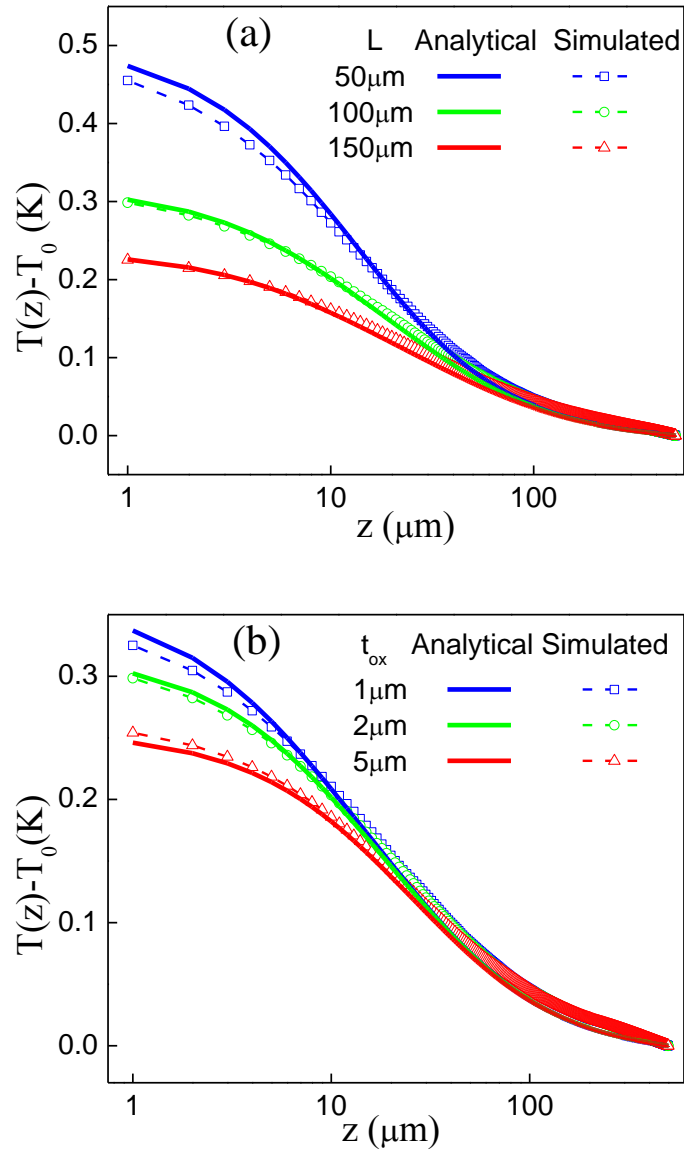


Figure 4. 5 Temperature profile in the substrate along z -axis with a heat source of 5mW.

(a) Results for a chip with $t_{ox} = 2\mu\text{m}$, $t_{sub} = 500\mu\text{m}$ and L as a parameter; (b) Results for a chip with $L = 100\mu\text{m}$, $t_{sub} = 500\mu\text{m}$ and various t_{ox} .

$$\begin{aligned}
& \int_0^z \arctan \left[\frac{(L'/2)(W'/2)}{z' \sqrt{(L'/2)^2 + (W'/2)^2 + z'^2}} \right] dz' \\
&= \left\{ z \arctan \left[\frac{L'}{2} \cdot \frac{W'}{2} \cdot \frac{1}{z\mu(z)} \right] - \frac{L'}{2} \operatorname{arc} \coth \left[\frac{\mu(z)}{W'/2} \right] - \frac{W'}{2} \operatorname{arc} \coth \left[\frac{\mu(z)}{L'/2} \right] \right\}_0^z
\end{aligned}$$

$$\text{where } \mu(z) \equiv \sqrt{(L'/2)^2 + (W'/2)^2 + z^2}.$$

The FEM simulation and semi-analytic results for the temperature profile in the substrate along the z -axis are plotted in Fig. 4.5(a) for three different values of heat source length. Note that the temperature of the substrate bottom surface, $T(t_{sub})=T_0$, is used as the reference. In addition, simulations are performed for different values of t_{ox} , as plotted in Fig. 4.5(b) along with the analytic results. Evidently, the vertical temperature profiles given by semi-analytic theory agree well with the FEM simulations. As could be expected, the (total) temperature rise in the substrate, $\Delta T_{sub} \equiv T(0) - T(t_{sub})$, increases as L or t_{ox} decreases. Comparing the FEM simulation results with that from the semi-analytic calculation, the difference between them is less than 10% which confirms the applicability of the semi-analytic theory.

4.4.2 Fractional thermo-optic tuning due to the substrate

Estimation of the temperature rise in the substrate is important because the temperature change in the top silicon device layer is affected by the temperature rise across the buried oxide layer as well as that of the substrate ($\Delta T_{tot} = \Delta T_{ox} + \Delta T_{sub}$). For example, in thermo-optic tunable delay lines, the total change of the delay time in the PCW ($\Delta \tau_{tot}$), which is proportional to the total temperature rise in the waveguide (for small change of refractive index $\Delta n \ll 1$), is also affected by the temperature rise in the

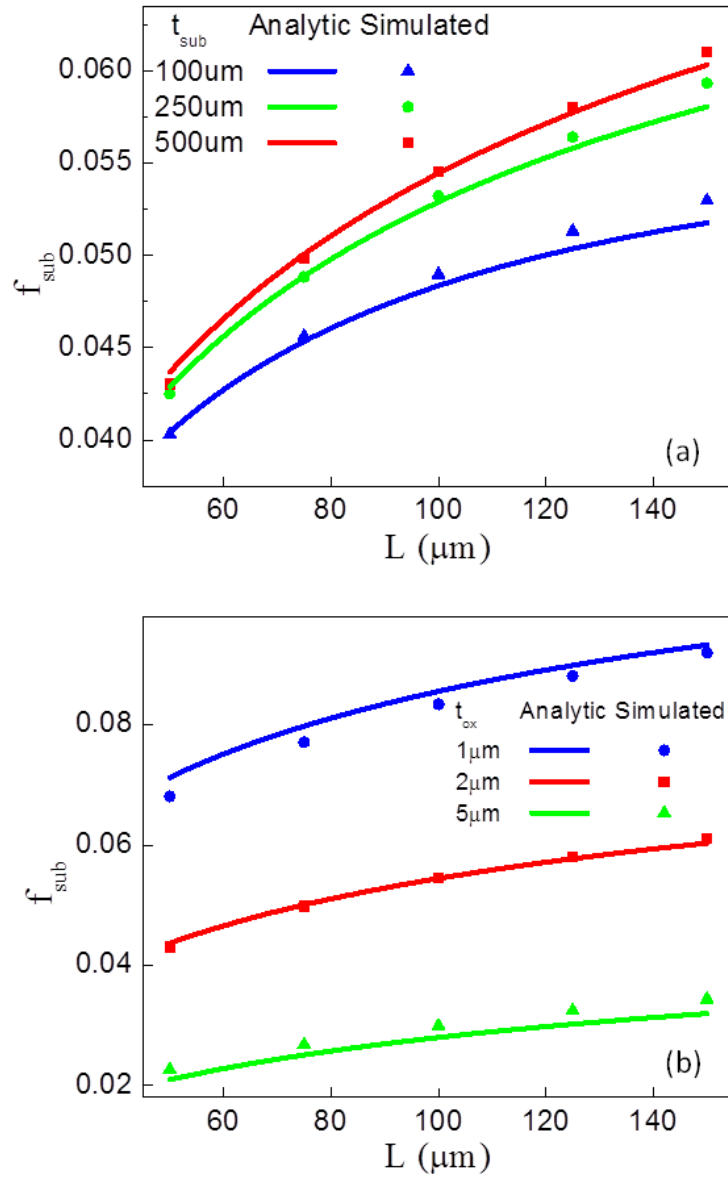


Figure 4. 6 Fractional delay perturbation due to the substrate as a function of L ; (a) For $t_{ox}=2\mu m$ with t_{sub} as a parameter; (b) For $t_{sub}=500\mu m$ with t_{ox} as a parameter.

substrate. Assume $\Delta\tau_{tot}=\mu\Delta T_{tot}$, where μ is a constant depending on the thermo-optic coefficient of silicon. Because $\Delta\tau_{tot}=\mu\Delta T_{ox}+\mu\Delta T_{sub}$, we can define the substrate-induced delay tuning as $\Delta\tau_{sub}=\mu\Delta T_{sub}$ (note that $\Delta\tau_{sub}$ does not mean the time delay of light in the substrate, but the delay in the waveguide due to the substrate temperature). Note that, by assuming fixed-angle heat spreading [133,134], ΔT_{ox} can also be analytically expressed as [125]

$$\Delta T_{ox} = Q t_{ox} / (\kappa_{ox} L [W + 2X_{spr}]) . \quad (4.10)$$

To assess the substrate's contribution in a general manner, it is more convenient to introduce a relative quantity, fractional thermo-optic tuning, $f_{sub}=\Delta\tau_{sub}/\Delta\tau_{tot}$.

Simulations are performed to estimate the fractional thermo-optic tuning due to the substrate. First, the influence of the substrate thickness is investigated. Simulations and semi-analytic calculations are carried out for three different substrate thicknesses and varying heat source lengths. As shown in Fig. 4.6(a), analytic results agree well with the FEM simulation. Their difference in f_{sub} is less than 5%. From the plot, it is evident that as the substrate thickness increases, f_{sub} increases as expected. In Fig. 4.6(b), simulation and analytic results are plotted for different buried oxide layer thicknesses. As t_{ox} increases, ΔT_{sub} decreases (and ΔT_{ox} increases); consequently f_{sub} decreases.

For some slow-light delay line applications in the nanosecond range or beyond, the PCW length may reach the millimeter scale or beyond, assuming group indices n_g in the range of 30~100 [125,136]. For thermo-optic delay tuning, similar heater lengths are required. It can be observed in Fig 4.6(b) that the value of f_{sub} increases as the heater becomes longer. To explore its upper limit for very long heaters, f_{sub} is calculated semi-analytically for L up to 10mm and the trend is shown in a semi-log plot in Fig. 4.7.

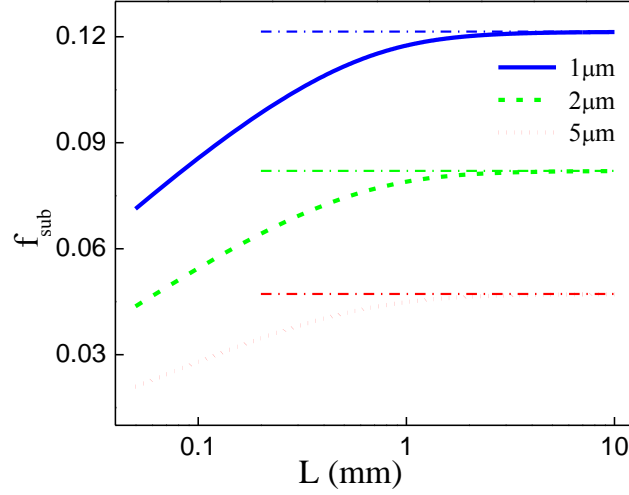


Figure 4. 7 The trend of fractional delay perturbation: Semi-analytic results for finite L with different oxide layer thicknesses for $t_{sub}=500\mu\text{m}$.

Interestingly, as L continues increasing, f_{sub} increases asymptotically towards a finite upper limit whose value depends on t_{ox} . This upper limit occurs because for $L \rightarrow \infty$, the structure can be treated as a two-dimensional problem in the x - z plane. For $L \rightarrow \infty$, it is necessary to define the linear power density as $Q_{Den} = \lim_{L \rightarrow \infty} Q/L$. From Eq. 4.9, by some calculation, the temperature rise across the substrate for $L \rightarrow \infty$ can be expressed as

$$\Delta T_{sub, L \rightarrow \infty} = \frac{Q_{Den}}{\pi \kappa_{Si}} \left[\frac{t_{sub}}{W'/2} \arctan\left(\frac{W'/2}{t_{sub}}\right) + \frac{1}{2} \ln\left(1 + \left(\frac{t_{sub}}{W'/2}\right)^2\right) \right]. \quad (4.10)$$

Horizontal dashed lines in Fig. 4.7 show the upper limit of f_{sub} calculated with Eq. 4.10. Evidently, they agree very well with the results from Eq. 4.9 at long L . In typical SOI devices, t_{sub} is on the order of hundreds of microns and W' is on the order of tens of microns, thus $t_{sub} \gg W'$. This can be used to further simplify Eq. 4.10 to

$$\Delta T_{sub,L \rightarrow \infty} \approx \frac{Q_{Den}}{\pi \kappa_{Si}} \left(1 + \ln \frac{2t_{sub}}{W + 2X_{spr} + 2t_{ox}} \right). \quad (4.11)$$

Calculations show that the Eq. 4.11 is a good approximation for Eq. 4.10. The difference between them is typically very small (e.g. <1%) for $t_{sub} > 3W$. Thus, Eq. 4.11 is useful in estimation.

4.4.3 Transient response of the TO PCW devices

Although 10% contribution from the substrate might be inconsequential in some digital applications, it can be a significant issue for many analog applications. For example, for tunable optical delay lines used in phased array antennas, the beam angle is proportional to the delay difference between adjacent elements [137]. A 10% variation of the delay difference (which is tuned thermo-optically) will cause a 10% deviation of the beam angle, which represents a significant issue for high-resolution radars (requiring accuracy of $\sim 0.25^\circ$ for up to 60° scanning angles [138]).

Furthermore, in transient from one delay state to another state, the substrate temperature profile generally takes a very long time to reach its steady state whereas the oxide temperature profile stabilizes very fast. For precision analog applications, the slow response of the substrate may play a dominant role in determining the overall response time of the device. Consider the example shown in Fig. 4.8, where the time-dependent ΔT_{ox} , ΔT_{sub} , and ΔT_{tot} data are extracted from a FEM simulation of the transient response of a structure. Note that ΔT_{ox} and ΔT_{sub} defined in this work do not refer to a uniform temperature increase in the oxide and the substrate, but the temperature difference between the upper and lower surfaces of these two regions. The rise time (10% to 90%)

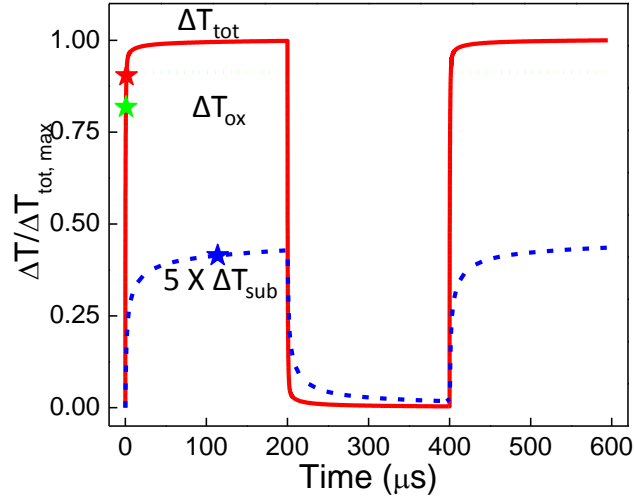


Figure 4. 8 Transient temperature response to a square-wave heating power with a period of $400\mu\text{s}$, a duty cycle of 50%. $L=150\mu\text{m}$, $t_{\text{sub}}=250\mu\text{m}$, and $t_{\text{ox}}=1\mu\text{m}$. All temperature values are normalized by the steady-state temperature $\Delta T_{\text{tot,max}}$. The ΔT_{sub} trace is magnified 5 times for ease of view. For each trace, the 90% point of the rising edge is marked with a star. (10% points of the rising edges of these curves are all close to $t=0$, they are not marked to avoid cluttered view).

for ΔT_{sub} is on the order of $100\mu\text{s}$ whereas the rise time (10% to 90%) for ΔT_{ox} is on the order of $1\mu\text{s}$. Note that the 10% point of these traces are all very close to $t=0$ and their difference in time is very small. On the other hand, the time difference of the 90% points of the ΔT_{sub} and ΔT_{ox} traces is very large; thus only the 90% points are marked. The fall time of each curve is on the same order as its respective rise time. The rise/fall time can be estimated from $\tau \sim Z^2 \rho c / \kappa$ where ρ is the density and c the specific heat capacity of the material and Z is the heat conduction length in this material [125]. For ΔT_{ox} , the

pertinent material is the silicon dioxide, Z is the thickness of the buried oxide layer. For ΔT_{sub} , the pertinent material is silicon, Z is on the order of the substrate thickness. Silicon and SiO_2 have comparable ρc ; and κ_{Si} is about two orders of magnitude higher than κ_{ox} . The substrate thickness is usually two orders larger than the buried oxide thickness. Based on these values, the transient response of the substrate is expected to be roughly two orders of magnitude slower than the buried oxide layer. Assume an analog application requires 1% delay tuning accuracy. Then the device analyzed in Fig. 4.8 is considered stable only after ΔT_{sub} reach ~90% of its steady-state value (so that ΔT_{tot} reaches 99% of its steady-state value because this device has $\Delta T_{sub} \sim 0.09 \Delta T_{tot}$ in the steady-state). Therefore, for this analog application, the device response time is practically ~100 μs . This is much longer than the intrinsic response time of the oxide layer.

4.4.4 Minimizing the substrate-induced thermooptic effect

According to the above discussions, it would be desirable to minimize the influence of the substrate in order to speed up the device response and improve the device stability/precision for many analog applications. To this end, it would be useful to analyze how the upper limit of f_{sub} ($L \rightarrow \infty$) varies with key physical parameters. Results are plotted in Fig. 4.9 for different substrate thicknesses and oxide thicknesses. It can be seen that the influence of the substrate can be reduced by increasing the thickness of the buried oxide layer. This reduction can be attributed to two trends: ΔT_{ox} increases as $t_{ox}^{1/2}$ [125] and ΔT_{sub} decreases with t_{ox} due to the term $\ln[2t_{sub}/(W+2X_{spr}+2t_{ox})]$ in Eq. 3.11. When the oxide layer is thicker than 5 μm , f_{sub} is less than 5% for all cases shown in Fig. 4.9(a). Furthermore, reducing the substrate thickness can also reduce ΔT_{sub} according to

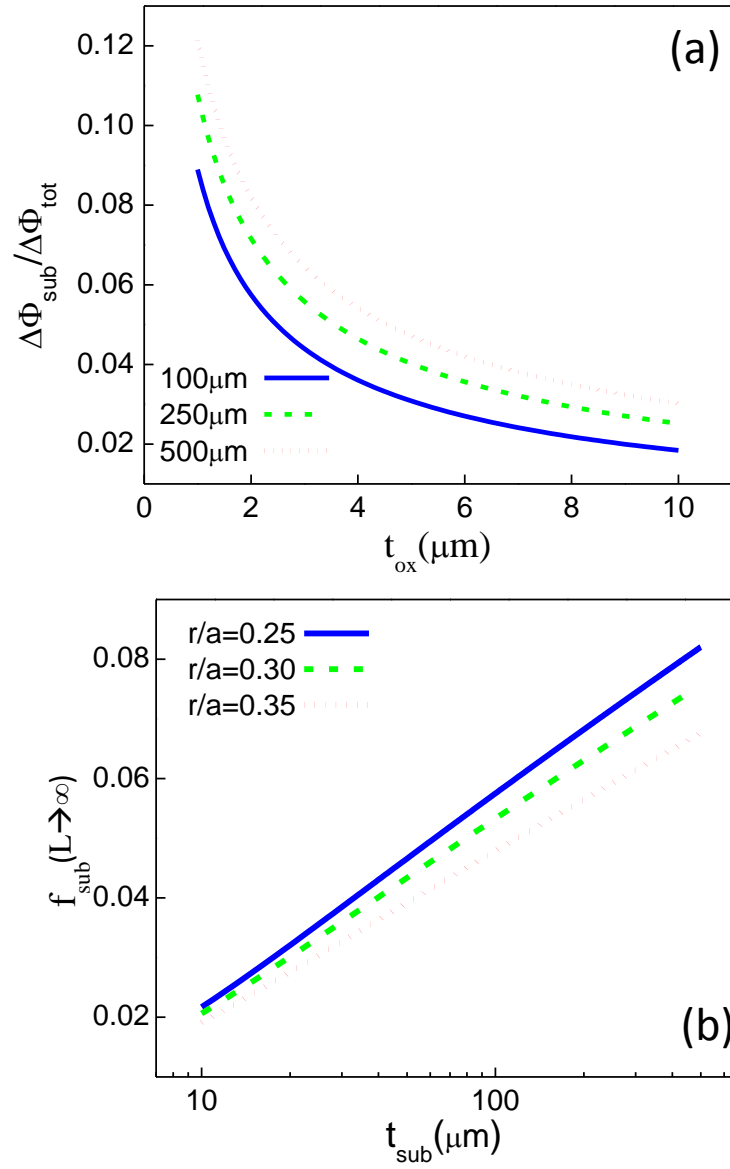


Figure 4. 9 Influence of some critical device parameters on $f_{\text{sub}}(L \rightarrow \infty)$ (a). Analytic results for $f_{\text{sub}}(L \rightarrow \infty)$ with t_{ox} as the variable for different substrate thicknesses. (b). the influence of the hole radius (with $t_{\text{ox}} = 2\mu\text{m}$).

Eq. 4.10. It can be readily shown that f_{sub} varies faster than $t_{ox}^{-1/2}$ with respect to the oxide thickness and varies logarithmically with t_{sub} . Thus, mathematically, f_{sub} can be more effectively reduced by increasing t_{ox} .

However, in practice, thicker oxide layers are less preferable for a number of reasons. First, it would be challenging and costly to achieve $t_{ox} > 5\mu\text{m}$ in making high-quality SOI wafers. Second, by increasing t_{ox} , the heat conductance between source and sink becomes smaller, which hampers device heat dissipation. Third, thicker oxide will lead to an increase of response time, which is not desirable for many active devices. On the other hand, a thinner substrate will provide better heat conductance and thus reduce the response time. Moreover, with the recent advance of membrane technology [139,140], the substrate can be easily reduced to less than $10\mu\text{m}$. Thus membrane based devices could help to reduce the substrate-induced thermo-optic tuning.

It should be noted that the structure shown in Fig. 4.1 is optimal. If the heater is located on a lateral edge of the PCW (e.g. heater located at $x_{\text{heater}}=7\mu\text{m}$, and the PCW core located at $x_{\text{core}}=0$), then the temperature rise in the PCW core ΔT_{core} could be 2~3 times smaller than the ΔT_{tot} at the heater due to the exponential temperature drop along x [125]. This can affect f_{sub} in the PCW core. To analyze such a case, we need to consider the total temperature rise in the top Si layer ΔT_{tot} , the vertical temperature difference between top and bottom surfaces of the substrate ΔT_{sub} , and the vertical temperature difference in oxide ΔT_{ox} in *two different vertical planes* at $x=x_{\text{heater}}$ and $x=x_{\text{core}}$, respectively. Obviously, the temperature rise in the core is just ΔT_{tot} in the plane at $x=x_{\text{core}}$, $\Delta T_{\text{core}} \equiv \Delta T_{\text{tot}}(x_{\text{core}})$. The actual delay tuning is determined by ΔT_{core} . Because ΔT_{core} is much lower than $\Delta T_{\text{tot}}(x_{\text{heater}})$, the fractional thermal tuning in the PCW core due to the

substrate in this case $f_{sub}(x_{core}) = \Delta T_{sub}(x_{core}) / \Delta T_{core}$ could be much larger than $\Delta T_{sub}(x_{heater}) / \Delta T_{tot}(x_{heater})$ given in preceding sections. In the worst case, $f_{sub}(x_{core})$ may exceed 20% in a non-optimal structure.

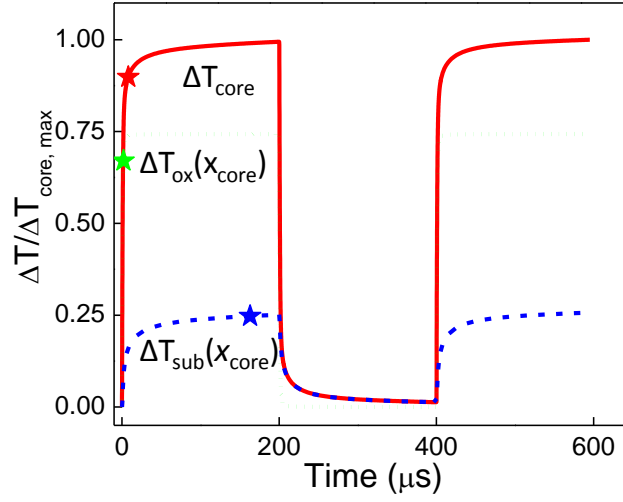


Figure 4. 10 Simulation result for a non-optimal case where the heater is located at the PCW lateral edge, 7 μ m from the PCW core (other parameters of this structure are same as in Fig. 4.8). All temperatures are evaluated in the vertical plane at $x=x_{core}$. Note $\Delta T_{core} \equiv \Delta T_{tot}(x_{core}) = \Delta T_{ox}(x_{core}) + \Delta T_{sub}(x_{core})$

For example, for the structure simulated in Fig. 4.8, if the heater is moved to a lateral edge about 7 μ m from the PCW core, $f_{sub}(x_{core})$ will reach ~25%, as shown in Fig. 4.10. Because $f_{sub}(x_{core})$ is far above 10%, the 10%-90% rise/fall time of $\Delta T_{tot}(x_{core})$ also elongates to ~12 μ s (compared to ~1 μ s rise/fall time from 10% to 90% for ΔT_{tot} in Fig. 4.8). This can explain the long rise time observed in prior experiments where the heater is located at the PCW edge (for example Ref. [121]). Note that 20% contribution is not negligible in many digital applications, as well as analog applications. This illustrates the

importance of design optimization in a wide range of thermo-optic tuning/switching applications. In some cases, configurations with a heater at the PCW edge may be desirable for the ease of fabrication, but the performance trade-off needs to be considered for a specific application. The formulas given in this work are useful to guide the design optimization and evaluate the substrate-induced thermal tuning.

4.5 Minimizing the substrate-induced thermooptic effect

Note that this theory also indicates that many factors have relatively weak influence on the device performance. For example, the hole radius of the photonic crystal structure, in its typical range ($r/a=0.25\sim0.35$), has a relatively weak influence on f_{sub} , as shown in Fig. 4.9(b). The heater width W is usually recommended to be relatively small to improve the heating efficiency [125]. As such, typically $W \ll 2X_{spr}$, and the influence of W on the ΔT_{sub} is fairly small according to our calculation. Also note that due to the complex anisotropic structure of a narrow heater embedded in a photonic crystal waveguide, the traditional fixed-angle spreading model is not applicable to this entire structure. The fixed-angle model can, however, be useful for a single, *thin* layer such as the buried oxide layer. The temperature variation within the top silicon layer is not taken into account because it is very small along y and z axes (less than 0.1%) [126].

Note that there exist small discrepancies between the analytic results and FEM simulation results. The maximum discrepancy of ΔT_{sub} between these two approaches is less than 5% in all cases we have simulated. The discrepancy can be attributed to several modeling assumptions used in this semi-analytic theory, including the quasi-1D model for heat transfer in a SOI PCW [125] and the fixed angle spreading model in buried oxide layer [133,134]. Each of these models has been validated in proper conditions with

reasonable accuracy (e.g. $<6\%$ in Ref. [125]). Also note that in most cases, ΔT_{sub} contributes less than 10% of ΔT_{tot} . Therefore, 5% discrepancies of ΔT_{sub} contribute less than 0.5% of the discrepancies of the overall temperature ΔT_{tot} . Such discrepancies of ΔT_{tot} are considered very small and very difficult to be further improved upon. Furthermore, it should be noted that our motivation of developing such a (semi-)analytic theory for describing a phenomenon is not to achieve best accuracy, but to gain physical insight that cannot be obtained through numerical simulations, such as how ΔT_{sub} scales with all key physical parameters, given in an analytic expression. It would be highly challenging to obtain such scaling or trends through FEM simulations when multiple parameters are involved and some parameters are varying over a large range. For example, to obtain the asymptotic trend shown in Fig. 4.7 through FEM simulations, it would require a prohibitive amount of computational resources because it would need to simulate many instances of extremely long/large devices with both L and t_{ox} varying.

It would be interesting to extend this theory to study the substrate-induced effect in other device geometries including air-bridge PCWs or non-photonic crystal structures. For some photonic structures, the ratio of the device dimension along y -axis over that along x -axis is not as large as PCWs. It can be expected that the heat is more concentrated like short PCWs, which means f_{sub} is typically a smaller value comparing to those of PCWs shown in Fig. 4.6. It may also be interesting to extend this work to integrated circuits on a SOI wafer. Because the transistors generally have smaller dimensions along x and y axis, it is expected that the substrate temperature rise due to a single transistor is fairly small. For a complicated circuit including many transistors and metal interconnects in different layers, it remains a challenging problem to investigate the substrate-induced

thermal issues. Detailed discussion of these further research topics is beyond the scope of this work.

4.6 Summary

In conclusion, the influence of the substrate on SOI thermo-optic photonic crystal devices is studied in terms of key physical parameters. The temperature rise in the substrate is calculated semi-analytically. The accuracy of the semi-analytic results is verified by the FEM simulations. The upper limit of the fractional delay tuning due to the substrate is obtained as a function of key physical parameters. For long delay lines, the substrate-induced fractional delay tuning could exceed 10% for heaters in the PCW core and exceed 20% for heaters at the PCW lateral edge. The slow response of the substrate may cause the device to take a long time to stabilize, which may significantly elongate the de facto response time of the device (by 10~100 fold). This could explain slow response observed in some non-optimal device structures and help guide further device optimization. Scaling of the substrate's influence with key structure parameters is analyzed. Strategies of minimizing the influence of the substrate are discussed.

Chapter 5 Conclusions and suggestions for future works

5.1 Conclusions

In this dissertation, the optical and thermal properties of periodic silicon photonic structures are studied. Targeting at high integration density, high power efficiency, and high response speed, different periodic photonic structures are proposed and studied.

Employing the 1-D periodically arranged AWA-based structure, we proposed and demonstrated a novel design for the high density on-chip integration of bus waveguides. An averaged pitch size as small as $0.8\mu\text{m}$ is achieved with a crosstalk level lower than -20dB. Results on asymmetric-waveguide pair show that, by tuning the width difference of the waveguides, a crosstalk level lower than -23dB can be achieved at the pitch size of $0.8\mu\text{m}$. Periodically arranged AWA bus waveguides are designed to achieve the -20dB system level crosstalk at a sub-micron pitch size. Fabricated 3-AWA structure firstly demonstrated an overall crosstalk level of -20.1dB with a pitch size at $1\mu\text{m}$. After the optimization, the 5-AWA-based bus waveguides with a pitch size at $0.8\mu\text{m}$ achieved a crosstalk level as low as -21.7dB.

Due to the high propagation loss, the applications of slow light PCWs are quite limited. In chapter 3, we systematically studied the slow light loss mechanisms in PCW structures. Firstly, we developed an analytic theory to study the roughness induced scattering loss in photonic crystal waveguides. Promising results were obtained. By separately calculating the backscattering loss and radiation loss, we proved that, in slow light region, the backscattering loss dominates. Our analytic results agree well with experiments. Combining with systematic simulations of the loss dependences on some key structure parameters, several methods were pointed out to reduce the backscattering loss.

Although the thermo-optic effect based tuning device is expected to show high power efficiency, its performance is hindered by the thick substrate. In chapter 4, the influence of the substrate on a TO PCW was simulated and analytically studied. An analytic model was built to calculate the temperature distribution across the substrate. The accuracy of this model is proved by comparing the analytic formula with the FEM simulations. It is shown that the substrate influence evidently depends on various parameters of the devices. By increasing the oxide layer thickness and/or reducing the substrate thickness, the substrate influence can be effectively reduced. Study on the transient response of the TO PCW devices shows that the rising time of the 500 μm thick substrate is on the order of 100 μs and the response speed can be improved by reducing the substrate thickness.

5.2 Suggestions for future works

Silicon photonics is a fast advancing field, especially after the demonstration of the compact and high speed active devices in the last decade. The hybrid integration with the electronic circuits is the target for the next step of the development. There are a lot of opportunities in the future. On system level, it is still arguable how the photonics should be integrated with electronics. Plenty of attentions have been attracted by the question of on what level the photonic structures should get involved. On device level, the high-efficiency silicon lasing source is still missing. Cost-effective hybrid III-V/IV integration or CMOS compatible light source should be developed.

Based on the results we have achieved, in the future, it would be interesting and intriguing to apply the AWA structure to other fields. For example, the coupling of light in multi-core fibers is extensively studied. By generalizing the model shown in Sec. 2.2 to two-dimensional case, it can be expected that the highly asymmetric structure can lead

to a significant reduction on the coupling strength and an enhancement on the channel-density. The periodic configuration will also ease the fiber design by just repeating the unit cell to get more channels. Some other kind of waveguide structures, such as the periodically width-tuning along the longitudinal direction, may lead to further improvement on the integration density.

In Chapter 3, we developed an analytic theory to calculate the slow light propagation loss in photonic crystal waveguides at a moderate group index (10~50). For group index higher than 50, new phenomena, such as multiple scattering, rise up, modifications and innovations should be made to adapt our theory for such applications. Practically, reduction of the propagation loss is fundamentally determined by the advancements of the fabrication technology. Cost-effective way to highly accurately pattern large areas of lattice structures will essentially advance the application of photonic crystal structures.

For the TO tuning photonic devices, its main limitation is its low speed. On one hand, the low thermal conductivity of SiO_2 enables the high tuning power efficiency. On the other hand, it limits the speed of the TO device. Tradeoffs must be made between these factors. To enhance its speed, new materials should be introduced. ZnO has a refractive index ~ 1.93 (close to Si_3N_4) and a thermal conductivity $\sim 60 \text{ W/m}^*\text{K}$ (40 times higher than SiO_2). The tuning speed will be greatly enhanced if high quality ZnO can be employed in silicon photonics.

Crosstalk between TO-tuning devices is another interesting topic in the future. Our analytic model discussed in chapter 4 is a one-dimensional approximation. It would be convenient to develop it to two-dimensional, which will enable the calculation of crosstalks between TO devices. Another challenging topic would be to develop an

analytic model to estimate the transient response of the TO devices. To do this, a new analogy other than the one used in Chapter 4, most probably, an analogy with the telegrapher's equations, should be considered.

References

- [1] . Jalali, and S. Fathpour, "Silicon Photonics", *J. Lightw. Technol.*, **24**, 4600-4615 (2006).
- [2] . N. Daldosso, and L. Pavesi, "Nanosilicon photonics", *Laser and Photon. Rev.*, **3**, 508-534 (2009).
- [3] . G. T. Reed (ed.), "Silicon Photonics: the State of the Art", Wiley, Chichester, UK, (2008).
- [4] . G. T. Reed, W. R. Headley, and C. E. J. Png, "Silicon Photonics – The Early Years", *Proc. SPIE*, 5730, 1-17 (2005).
- [5] . M. Lipson, "Guiding, Modulating, and Emitting Light on Silicon – Challenges and Opportunities", *J. Lightw. Techn.* **23**, 4222-4238 (2005).
- [6] . R. Soref, "The past, present, and future of silicon photonics," *IEEE J. Sel. Top. Quantum Electron.* **12**, 1678-1687 (2006).
- [7] . R. G. Beausoleil, "Large-scale Integrated Photonics for High-Performance Interconnects", *J. on Emerg. Technol. Compt. Syst.* **7**, 6, 1-54 (2011).
- [8] . G. T. Reed, G. Mashanovich, F. Y. Gardes and D. J. Thomson, "Silicon Optical Modulators", *Nat. Photon.* **4**, 518-526 (2010).
- [9] . M. J. Weber (ed.), "Handbook of optical materials", CRC Press, Boca Raton, Florida (2002).
- [10] . V. G. Dmitriev, G. G. Gurzadyan, D. N. Nikogosyan, "Handbook of nonlinear optical crystals", Springer, Heidelberg, Germany (1999).
- [11] . G. K. Celler, and S. Cristoloveanu, "Frontiers of silicon-on-insulator", *J. Appl. Phys.*, **93**, 4955-4978 (2003).
- [12] . L. Leuthold, C. Koos, and W. Freude, "Nonlinear silicon photonics", *Nat. Photon.*, **4**, 535-544 (2010).
- [13] . S. Feng, T. Lei, H. Chen, H. Cai, X. Luo, and A. W. Poon, "Silicon photonics: from a microresonator perspective", *Laser Photon. Rev.* **6**, 145-177 (2012).
- [14] . K. Yamada, "Silicon Photonic Wire Waveguides: Fundamentals and Applications", *Silicon. Photon. II. Top. Appl. Phys.* **119**, 1-29 (2011).
- [15] . A. V. Krishnamoorthy, X. Zheng, G. Li, J. Yao, T. Pinguet, A. Mekis, H. Thacker, I. Shubin, Y. Luo, K. Raj, and J. E. Cunningham, "Exploiting CMOS Manufacturing to Reduce Tuning Requirements for Resonant Optical Devices", *IEEE. Photon. J.* **3**, 567-579 (2011).
- [16] . J. M. Fedeli, B. Ben Bakir, L. Grenouillet, D. Marris-Morini, and L. Vivien, "Photonics and Electronics Integration", *Silicon. Photon. II, Top. Appl. Phys.* **119**, 217-249 (2011).
- [17]. Online source <http://www.itrs.net/>
- [18]. O. Boyraz and B. Jalali, "Demonstration of a silicon Raman laser", *Opt. Express* **12**, 5269–5273 (2004).
- [19] . Y. A. Vlasov, "Silicon CMOS-integrated nano-photonics for computer and data communications beyond 100G", *IEEE Commun. Magaz.* **50**, S67-S72 (2012).
- [20] . G. Roelkens, L. Liu, D. Liang, R. Jones, A. Fang, B. Koch, and J. Bower, "III-V/silicon photonics for on-chip and inter-chip optical interconnects", *Laser and Photon. Rev.* **4**, 751-779 (2010).

- [21] . R. Soref and B. ENNETT, “Electrooptical Effects in Silicon”, IEEE J. Quant Electron. **23**, 123-129 (1987).
- [22] . A. Liu, R. Jones, L. Liao, and D. Samara-Rubio, D. Rubin, O. Cohen, R. Nicolaescu, and M. Paniccia, “A high speed silicon optical modulator based on a metal-oxide-semiconductor capacitor”, Nature **427**, 615–618 (2004).
- [23] . Y. Jiang, W. Jiang, L. Gu, X. Chen, R. T. Chen, “80-micron interaction length silicon photonic crystal waveguide modulator”, Appl. Phys. Lett. **87**, 221105 (2005).
- [24] . Q. Xu, B. Schmidt, S. Pradhan, and M. Lipson, “Micrometre-scale silicon electrooptic modulator”, Nature **435**, 325–327 (2005).
- [25] . K. Okamoto, “Progress and technical challenge for planar waveguide devices: silica and silicon waveguides”, Laser and Photon. Rev. **6**, 14-23 (2012).
- [26] . T. Pinguet, S. Gloeckner, G. Masini, and A. Mekis, “CMOS photonics: a platform for optoelectronics integration”, Silicon. Photon. II, Top. Appl. Phys. **119**, 187-216 (2011).
- [27] . M. Paniccia, “Integrating silicon photonics”, Nat. Photon. **4**, 498-499 (2010).
- [28] . S. M. Selvaraja, W. Bogaerts, P. Dumon, D. Van Thourhout, and R. Baets, “Subnanometer Linewidth Uniformity in Silicon Nanophotonic Waveguide Devices Using CMOS Fabrication Technology”, J. Sel. Topic. Quant. Electron. **16**, 316-324 (2010).
- [29] . A. Scandurra, “Silicon photonics: the system on chip perspective”, Silicon. Photon. II, Top. Appl. Phys. **119**, 143-168 (2011).
- [30] . M.B. Ritter, Y. Vlasov, J.A. Kash and A. Benner, “Optical technologies for data communication in large parallel systems”, J. Instrument. **6**, C01012 (2011).
- [31] . X. Zheng, Y. Luo, J. Lexau, F. Liu, G. Li, H. D. Thacker, I. Shubin, J. Yao, R. Ho, J. E. Cunningham, and A. V. Krishnamoorthy, “2-pJ/bit (On-Chip) 10-Gb/s Digital CMOS Silicon Photonic Link”, IEEE Photon. Tech. Lett. **24**, 1260-1262 (2012).
- [32] . D. A. B. Miller, “Device Requirements for Optical Interconnects to Silicon Chips”, Proc. IEEE. **97**, 1166-1185 (2009).
- [33] . A. Liu, L. Liao, Y. Chetrit, J. Basak, H. Nguyen, D. Rubin, and M. Paniccia, “Wavelength Division Multiplexing Based Photonic Integrated Circuits on Silicon-on-Insulator Platform”, J. Sel. Topic. Quant. Electron. **16**, 23-32 (2010).
- [34] . J. D. Joannopoulos, S. G. Johnson, J. N. Winn, and R. D. Meade, “Photonic Crystals: Molding the Flow of Light”, 2nd ed. Princeton University Press, Princeton and Oxford, (2008).
- [35] . C. Kittel, “Introduction to Solid State Physics”, 8th ed. John Wiley & Sons, Hoboken, (2005).
- [36] . M. Notomi, “Manipulating light with strongly modulated photonic crystals”, Rep. Prog. Phys. **73**, 1-57 (2010).
- [37] . T. F. Krauss, and R. M. De La Rue, “Photonic crystals in the optical regime – past, present and future”, Prog. Quant. Electron. **23**, 51-96 (1999).
- [38] . R. M. De La Rue, and C. Seassal, “Photonic crystal devices: some basics and selected topics”, Laser Photon. Rev. **6**, 564-587 (2012).
- [39] . C. Grillet, C. Monat, C. L. Smith, M. W. Lee, S. Tomljenovic-Hanic, C. Karnutsch, and B. J. Eggleton, “Reconfigurable photonic crystal circuits”, Laser & Photon. Rev. **4**, 192-204 (2010).

- [40] . R. A. Integlia, W. Song, J. Tan, and W. Jiang, "Longitudinal and angular dispersions in photonic crystals: a synergistic perspective on slow light and superprism effects", *J. Nanosci. Nanotechnol.* **10**, 1596-1605 (2010).
- [41] . T. Baba, "Slow Light in Photonic crystal", *Nat. Photon.* **2**, 465-473 (2008).
- [42] . M. Soljacic and J. D. Joannopoulos, "Enhancement of nonlinear effects using photonic crystals", *Nat. Materials*, **3**, 211-219 (2004).
- [43]. G. Li, J. Yao, Y. Luo, H. Thacker, A. Mekis, X. Zheng, I. Shubin, J. Lee, K. Raj, J. Cunningham, and A. V. Krishnamoorthy, "Ultralow-loss, high-density SOI optical waveguide routing for macrochip interconnects", *Opt. Exp.* **20**, 12035-12039 (2012).
- [44]. M. Smit, J. van der Tol, and M. Hill, "Moore's law in photonics", *Laser & Photon. Rev.* **6**, 1-13 (2012).
- [45]. K. Okamoto, "Fundamentals of Optical Waveguides", Academic Press, San Diego, (2000).
- [46]. D. N. Christodoulides, F. Lederer, and Y. Silberberg, "Discretizing light behaviour in linear and nonlinear waveguide lattices", *Nature.* **424**, 817-823 (2003) .
- [47]. I. L. Garanovich, S. Longhi, A. A. Sukhorukov, and Y. S. Kivshar, "Light propagation and localization in modulated photonic lattices and waveguides", *Phys. Rep.* **518**, 1-79 (2012).
- [48]. H. F. Taylor, and A. Yariv, "Guided wave optics", *Proc. IEEE*, **62**, 1044-1060 (1974) .
- [49] . P. Yeh, A. Yariv, and C. S. Hong, "Electromagnetic propagation in periodic stratified media. I. General theory," *J. Opt. Soc. Am.* **67**, 423 (1977).
- [50] . F. Lederer, G. I. Stegeman, D. N. Christodoulides, G. Assanto, M. Segev, and Y. Silberberg, "Discrete solitons in optics", *Phys. Rep.* **463**, 1-126 (2008).
- [51] . R. G. Beausoleil, J. Ahn, N. Binkert, A. Davis, D. Fattal, M. Fiorentino, N. P. Jouppi, M. McLaren, C. M. Santori, R. S. Schreiber, S. M. Spillane, D. Vantrease, and Q. Xu, "A Nanophotonic Interconnect for High-Performance Many-Core Computation", 16th IEEE Symp. High Perform. Intercon. 182-189 (2008).
- [52] . A. Talneau, "Slow light modes for optical delay lines: 2D photonic crystal-based design structures, performances and challenges", *J. Opt.* **12**, 1-7 (2010).
- [53] . M. Natomi, K. Yamada, A. Shinya, J. Takahashi, C. Takahashi, and I. Yokohama, "Extremely large group-velocity dispersion of line-defect waveguides in photonic crystal slabs", *Phys. Rev. Lett.* **87**, 253902.
- [54] . T. Tanabe, M. Notomi, E. Kuramochi, and H. Taniyama, "Large pulse delay and small group velocity achieved using ultrahigh-Q photonic crystal nanocavities", *Opt. Exp.* **15**, 7826-7839 (2007).
- [55] . J. Li, T. P. White, L. O'Faolain, A. Gomez-Iglesias, and T. F. Krauss, "Systematic design of flat band slow light in photonic crystal waveguides", *Opt. Exp.* **16**, 6227-6232 (2008).
- [56]. Y. Hamachi, S. Kubo, and T. Baba, "slow light with low dispersion and nonlinear enhancement in a lattice-shifted photonic crystal waveguide", *Opt. Lett.* **34**, 1072-1074 (2009)
- [57] . S. A. Schulz, L. O'Faolain, D. M. Beggs, T. P. White, A. Melloni, and T. F. Krauss, "Dispersion engineered slow light in photonic crystals: a comparison", *J. Opt.* **12**, 1-10 (2010).

- [58] . T. F. Krauss, “Why do we need slow light”, *Nat. Photon.*, **2**, 448-450 (2008).
- [59] . Y. A. Vlasov and S. J. McNab, “Coupling into the slow light mode in slab-type photonic crystal waveguide”, *Opt. Lett.* **31**, 50-52 (2006)
- [60] . P. Pottier, M. Gnan, and R. M. De La Rur, “Efficient coupling into slow-light photonic crystal channel guides using photonic crystal tapers”, *Opt. Exp.* **15**, 6569-6575 (2007).
- [61] . J. P. Hugonin, P. Lalanne, T. P. White, and T. F. Krauss, “Coupling into slow-mode photonic crystal waveguides”, *Opt. Lett.* **32**, 2638-2640 (2007).
- [62] . A. Hosseini, X. Xu, D. N. Kwong, H. Subbaraman, W. Jiang, and R. T. Chen, “On the role of evanescent modes and group index tapering in slow light photonic crystal waveguide coupling efficiency”, *Appl. Phys. Lett.* **98**, 031107 (2011).
- [63] . S. Rahimi, A. Hosseini, X. Xu, H. Subbaraman, and R. T. Chen, “Group-index independent coupling to band engineered SOI photonic crystal waveguide with large slow-down factor”, *Opt. Exp.* **19**, 21832-21841 (2011).
- [64] . P. A. Morton, J. Cardenas, J. B. Khurgin, and M. Lipson, “Fast thermal switching of wideband optical delay line with no long-term transient”, *IEEE Photon. Tech. Lett.* **24**, 512-514 (2012).
- [65] . A. H. Atabaki, E. Shah Hosseini, A. A. Eftekhari, S. Yegnanarayanan, and A. Adibi, “Optimization of metallic microheaters for high-speed reconfigurable silicon photonics”, *Opt. Exp.*, **18**, 18312-18323 (2010).
- [66] . Y. A. Vlasov, M. O’boyle, H. F. Hamann, and S. J. McNab, “Active control of slow light on a chip with photonic crystal waveguides”, *Nature* **438**, 65-69 (2005).
- [67] . G.P. Watson, S.D. Berger, J.A. Liddle, and W.K. Waskiewicz, “A background dose proximity effect correction technique for scattering with angular projection electron lithography implemented in hardware”, *J. Vacuum Sci. Techn B*, **13**, 2504-2507, (1995).
- [68] . G. Owen, “Methods for proximity effect correction in electron lithography”, *J. Vacuum Sci. Techn B*, **8**, 1889-1892, (1990).
- [69] . EBL workshop for JEOL 6300 at Center for Functional Nanomaterial (Brookhaven National Lab, 2012).
- [70] . R. A. Integlia, L. Yin, D. Ding, D. Z. Pan, D. M. Gill, W. Song, Y. Qiana, and W. Jiang, “Fabrication and characterization of parallel-coupled dual racetrack silicon micro-resonators”, *Proc. of SPIE* **8266**, 82660M (2012).
- [71] . M. D. Henry, “ICP etching of silicon”, Ph. D. thesis (CALIFORNIA INSTITUTE OF TECHNOLOGY, 2010).
- [72] . J. Lee and G. Yeom, J. Lee and J. Lee, “Study of shallow silicon trench etch process using planar inductively coupled plasmas”, *J. Vacuum Sci. Techn A*, **15**, 573-578 (1997).
- [73] . U. Peschel, T. Pertsch, and F. Lederer, “Optical bloch oscillations in waveguide arrays”, *Opt. Lett.* **23**, 1701–1703 (1998).
- [74] . H.S. Eisenberg, Y. Silberberg, R. Morandotti, and J.S. Aitchison, “Diffraction management”, *Phys. Rev. Lett.* **85**, 1863–1866 (2000)
- [75] . S. Longhi, M. Marangoni, M. Lobino, R. Ramponi, P. Laporta, E. Cianci, and V. Foglietti, “Observation of dynamic localization in periodically curved waveguide arrays”, *Phys. Rev. Lett.* **96**, 243901 (2006).

- [76] . S. Longhi, "Optical Zener-Bloch oscillations in binary waveguide arrays", *Europhys. Lett.*, **76**, 416–421 (2006)
- [77] . R. Gordon, "Harmonic oscillation in a spatially finite array waveguide", *Opt. Lett.* **29**, 2752–2754 (2004).
- [78] . Y.V. Kartashov, and V.A. Vysloukh, "Light tunneling inhibition in array of couplers with longitudinal refractive index modulation", *Opt. Lett.* **35**, 205–207 (2010).
- [79] . A. Szameit, Y.V. Kartashov, F. Dreisow, M. Heinrich, T. Pertsch, S. Nolte, A. Tünnermann, V.A. Vysloukh, F. Lederer, and L. Torner, "Inhibition of light tunneling in waveguide arrays", *Phys. Rev. Lett.* **102**, 153901 (2009)
- [80] . S. Longhi, "Quantum-optical analogies using photonic structures", *Laser and Photon. Rev.* **3**, 243-261 (2009).
- [81] . Y. A. Vlasov and S. J. McNab, "Losses in single-mode silicon-on-insulator strip waveguides and bends", *Opt. Exp.*, **12**, 1622-1631 (2004).
- [82] . L. Gabrielli, D. Liu, S. G. Johnson, and M. Lipson, "On-chip transformation optics for multimode waveguide bends", *Nature Communicat.* **3**, 1271 (2012).
- [83] . S. Tang, R. Chen, R. Mayer, D. Gerold, T. Jansson, and A. Kostrzewski, "Channel Cross-Coupling in a Polymer-Based Single-Mode Bus Array", *J. Lightwave Tech.* **13**, 37-41 (1995).
- [84] . J. Chan, G. Hendry, A. Biberman, and K. Bergman, "Architectural Exploration of Chip-Scale Photonic Interconnection Network Designs Using Physical-Layer Analysis", *J. Lightwave Tech.* **28**, 1305-1315 (2010).
- [85] . H. Pan, S. Assefa, W. M. J. Green, D. M. Kuchta, C. L. Schow, A. V. Rylyakov, B. G. Lee, C. W. Baks, S. M. Shank, and Y. A. Vlasov, "High-speed receiver based on waveguide germanium photodetector wire-bonded to 90nm SOI CMOS amplifier", *Opt. Exp.*, **20**, 18145-18155(2012).
- [86] . A. Hardy and W. Streifer, "Coupled Mode Theory of Parallel Waveguides", *J. Lightwave Tech.* **LT-3**, 1135-1146 (1985).
- [87] . H. Hsu, Y. Hirobe, and T. Ishigure, "Fabrication and inter-channel crosstalk analysis of polymer optical waveguides with W-shaped index profile for high-density optical interconnections", *Opt. Expr.* **19**, 14018-14030 (2011)
- [88] . F. Eilenberger, S. Minardi, A. Szameit, U. Röpke, J. Kobelke, K. Schuster, H. Bartelt, S. Nolte, A. Tünnermann, and T. Pertsch, "Light Bullets in waveguide arrays: spacetime-coupling, spectral symmetry breaking and superluminal decay", *Opt. Expr.* **19**, 23171-23187 (2011)
- [89] . L. L. Gu, W. Jiang, X. Chen, L. Wang, and R. T. Chen, " High speed silicon photonic crystal waveguide modulator for low voltage operation", *Appl. Phys. Lett.* **90**, 071105 (2007).
- [90] . J. T. Mok, and B. J. Eggleton, "Photonics: expect more delays", *Nature* **433**, 811-812 (2005).
- [91] . M. Notomi, K. Yamada, A. Shinya, J. Takahashi, C. Takahashi, and I. Yokohama, "Extremely large group-velocity dispersion of line-defect waveguides in photonic crystal slabs", *Phys. Rev. Lett.* **87**, 253902 (2001).
- [92] . W. Bogaerts, P. Bienstman, and R. Baets, "Scattering at sidewall roughness in photonic crystal slabs", *Opt. Lett.* **28**, 689-691 (2003).

- [93] . D. Gerace, and L. C. Andreani, "Disorder-induced losses in photonic crystal waveguides with line defects", *Opt. Lett.* **29**, 1897-1899 (2004).
- [94] . S. G. Johnson, M. L. Povinelli, M. Soljacic, A. Karalis, S. Jacobs, and J. D. Joannopoulos, "Roughness losses and volume-current methods in photonic-crystal waveguides", *Appl. Phys. B* **81**, 283-293 (2005).
- [95] . S. Hughes, L. Ramunno, J. F. Young, and J. E. Sipe, "Extrinsic optical scattering loss in photonic crystal waveguides: role of fabrication disorder and photon group velocity", *Phys. Rev. Lett.* **94**, 033903 (2005).
- [96] . E. Kuramoch, M. Notomi, S. Hughes, A. Shinya, T. Watanabe, and L. Ramunno, "Disorder-induced scattering loss of line-defect waveguides in photonic crystal slabs", *Phys. Rev. B* **72**, 161318 (2005).
- [97] . R. J. P. Engelen, D. Mori, T. Baba, and L. Kuipers, "Two regimes of slow light losses revealed by adiabatic reduction of group velocity"., *Phys. Rev. Lett.* **101**, 103901 (2008).
- [98] . M. L. Povinelli, S. G. Johnson, E. Lidoridis, J. D. Joannopoulos, and M. Soljacic, "Effect of a photonic band gap on scattering from waveguide disorder", *Appl. Phys. Lett.* **84**, 3639 (2004).
- [99] . B. Wang, S. Mazoyer, J. P. Hugonin, and P. Lalane, "Backscattering in monomode periodic waveguides", *Phys. Rev. B* **78**, 245108 (2008).
- [100] . N. Le Thomas, H. Zhang, J. Jagerska, V. Zabelin, and R. Houdre, "Light transport regimes in slow light photonic crystal waveguides"., *Phys. Rev. B* **80**, 125332 (2009).
- [101] . A. Petrov, M. Krause, and M. Eich, "Backscattering and disorder limits in slow light photonic crystal waveguides", *Opt. Express* **17**, 8676-8684 (2009).
- [102] . J. F. McMillan, M. Yu, D. L. Kwong, and W. Chee, "Observation of four-wave mixing in slow-light silicon photonic crystal waveguides", *Opt. Express* **18**, 15484-15497 (2010).
- [103] . L. O'Faolain, T. P. White, D. O'Brien, X. Yuan, M. D. Settle, and T. F. Krauss, "Dependence of extrinsic loss on group velocity in photonic crystal waveguides", *Opt. Express* **15**, 13129-13138 (2007).
- [104] . S. G. Johnson, P. Bienstman, M. A. Skorobogatiy, M. Ibanescu, E. Lidoridis, and J. D. Joannopoulos, "Adiabatic theorem and continuous coupled-mode theory for efficient taper transitions in photonic crystals", *Phys. Rev. E* **66**, 066608 (2002).
- [105] . M. Skorobogatiy, M. Ibanescu, S. G. Johnson, O. Weisberg, T. D. Engeness, M. Soljacic, S. A. Jacobs, and Y. Fink, "Analysis of general geometric scaling perturbations in a transmitting waveguide: fundamental connection between polarization-mode dispersion and group-velocity dispersion", *J. Opt. Soc. Am. B* **19**, 2867-2875 (2002).
- [106] . D. Marcuse, "Theory of Dielectric Optical Waveguides", Academic Press, San Diego, (1991).
- [107] . G. Lecamp, J. P. Hugonin, and P. Lalanne, "Theoretical and computational concepts for periodic optical waveguides", *Opt. Express* **15**, 11042-11060 (2007).
- [108] . W. Jiang, and C. D. Gong, "Two mechanisms, three stages of the localization of light in a disordered dielectric structure with photonic band gaps", *Phys. Rev. B* **60**, 12015 (1999).

- [109] . S. G. Johnson, and J. D. Joannopoulos, "Block-iterative frequency-domain methods for Maxwell's equations in a planewave basis", *Opt. Express* **8**, 173-190 (2001).
- [110] . S. G. Johnson, M. Ibanescu, M. A. Skorobogatiy, O. Weisberg, J. D. Joannopoulos, and Y. Fink, "Perturbation theory for Maxwell's equations with shifting material boundaries", *Phys. Rev. E* **65**, 066611 (2002).
- [111] . W. Jiang, and R. T. Chen, "Rigorous analysis of diffraction gratings of arbitrary profiles using virtual photonic crystals", *J. Opt. Soc. Am. A* **23**, 2192 (2006).
- [112] . We also used the finite difference time-domain (FDTD) technique, but found that it required very long simulation time to obtain the frequency resolutions needed.
- [113] . S. Mazoyer, J. P. Hugonin, and P. Lalanne, "Disorder-induced multiple scattering in photonic-crystal waveguides", *Phys. Rev. Lett.* **103**, 063903 (2009).
- [114] . M. Patterson, S. Hughes, S. Schulz, D. M. Beggs, T. P. White, L. O'Faolin, and T. F. Krauss, "Disorder-induced incoherent scattering losses in photonic crystal waveguides: Bloch mode reshaping, multiple scattering, and breakdown of the Beer-Lambert law", *Phys. Rev. B* **80**, 195305 (2009).
- [115] . Y. A. Vlasov, and S. J. McNab, "Coupling into the slow light mode in slab-type photonic crystal waveguides", *Opt. Lett.* **31**, 50 (2006).
- [116] . S. John, "Strong localization of photons in certain disordered dielectric superlattices", *Phys. Rev. Lett.* **58**, 2486-2489 (1987).
- [117] . M. Patterson, S. Hughes, S. Combrie, N. V. Quynh Tran, A. De Rossi, R. Gabet, and Y. Jaouen, "Disorder-induced coherent scattering in slow-light photonic crystal waveguides", *Phys. Rev. Lett.* **102**, 253903 (2009).
- [118] . W. Jiang, R. T. Chen, and X. J. Lu, "Theory of light refraction at the surface of a photonic crystal", *Phys. Rev. B* **71**, 245115 (2005).
- [119] . L. Gu, W. Jiang, X. Chen, and R. T. Chen, "Physical mechanism of p-i-n diode based photonic crystal silicon electrooptic modulators for gigahertz operation," *IEEE J. Sel. Top. Quant. Electron.* **14**, 1132-1139 (2008).
- [120] . T. Chu, H. Yamada, S. Ishida, and Y. Arakawa, "Thermo-optic switch based on photonic-crystal line-defect waveguides," *IEEE Photon. Technol. Lett.* **17**, 2083-2085 (2005).
- [121] . L. Gu, W. Jiang, X. Chen, and R. T. Chen, "Thermooptically tuned photonic crystal waveguide silicon-on-insulator Mach-Zehnder interferometers," *IEEE Photonics Technol. Lett.* **19**, 342-344 (2007).
- [122] . D. M. Beggs, T. P. White, L. O'Faolain, and T. F. Krauss, "Ultracompact and low-power optical switch based on silicon photonic crystals," *Opt. Lett.* **33**, 147-149 (2008).
- [123] . N. Ishikura, T. Baba, E. Kuramochi, and M. Notomi, "Large tunable fractional delay of slow light pulse and its application to fast optical correlator," *Opt. Express* **19**, 24102 (2011).
- [124] . M. T. Tinker and J-B. Lee, "Thermal and optical simulation of a photonic crystal light modulator based on the thermo-optic shift of the cut-off frequency," *Opt. Express* **13**, 7174-7188 (2005).

- [125] . M. Chahal, G. K. Celler, Y. Jaluria, and W. Jiang, "Thermo-optic characteristics and switching power limit of slow-light photonic crystal structures on a silicon-on-insulator platform," *Opt. Express*, **20**, 4225-4231 (2012).
- [126] . W. Song, M. Chahal, G. K. Celler, Y. Jaluria, G. T. Reed and W. Jiang, "The influence of substrate on SOI photonic crystal thermo-optic devices", *Opt. Express*, **21**, 4235-4243 (2013).
- [127] . Y. Jaluria, "Design and Optimization of Thermal Systems", 2nd ed. CRC Press, Boca Raton, Florida, (2008).
- [128] . Y. Jaluria, "Natural Convection Heat and Mass Transfer", Pergamon Press, Oxford, UK, (1980).
- [129] . J. D. Jackson, "Classical electrodynamics", 3rd ed. John Wiley & Sons, Hoboken, NJ, (1999).
- [130] . F. P. Incropera, D. P. Dewitt, T. L. Bergman and A. S. Lavine, "Fundamentals of Heat and Mass Transfer", 6th ed. John Wiley & Sons, New York, (2007).
- [131] . H. S. Carslaw and J. C. Jaeger, "Conduction of heat solids", 2nd ed, Oxford University Press, Amen House, London, UK, (1959).
- [132] . G. Baffou, R. Quidant, and F. Javier Garcia de Abajo, "Nanoscale control of optical heating in complex plasmonic system", *ACS Nano*, **4**, 709-716 (2010).
- [133] . R. F. David, "Computerized Thermal Analysis of Hybrid Circuits," *IEEE Trans. Parts, Hybrids, Packag.*, **13**, 283-290 (1977).
- [134] . F. N. Masana, "A Closed Form Solution of Junction to Substrate Thermal Resistance in Semiconductor Chips," *IEEE Trans. Comp., Packag., Manufact. Technol.*, **19**, 539-545 (1996).
- [135] . W. H. Hayt and J. A. Buck, "Engineering Electromagnetics", 7th ed. McGraw-Hill, Boston (2006).
- [136] . W. Song, R. A. Integlia, and W. Jiang, "Slow light loss due to roughness in photonic crystal waveguides: An analytic approach," *Phys. Rev. B* **82**, 235306 (2010).
- [137] . M. Y. Chen, H. Subbaraman, and R. T. Chen, "Photonic Crystal Fiber Beamformer for Multiple X Band Phased-Array Antenna Transmissions," *IEEE Photon. Technol. Lett.* **20**, 375–377 (2008).
- [138] . E. Brookner, "Practical Phased Array Antenna Systems", Artech House, Boston (1991).
- [139] . J. A. Rogers, M. G. Lagally, R. G. Nuzzo, "Synthesis assembly and applications of semiconductor nanomembranes," *Nature* **477**, 45-53 (2011).
- [140] . S. Huang, J. Luo, H.L. Yip, A. Ayazi, X.H. Zhou, M. Gould, A. Chen, T. Baehr-Jones, M. Hochberg, A. K.Y. Jen, "Efficient Poling of Electro-Optic Polymers in Thin Films and Silicon Slot Waveguides by Detachable Pyroelectric Crystals", *Adv. Mater.* **24**, OP42–OP47(2012).

Curriculum Vitae

OF

WEIWEI SONG

EDUCATION

Ph.D. in Electrical Engineering, May 2013, Rutgers University, Piscataway, NJ
M.S. in Department of Physics, July 2008, Nanjing University, Nanjing, China
B.S. in Department of Physics, July 2005, Nanjing University, Nanjing, China

RESEARCH EXPERIENCE

- Demonstrated the pitch of Si bus waveguide array can be reduced from the generally believed μm to $0.8\mu\text{m}$ at a crosstalk level as low as -21.7dB .
- Improved the nanofabrication process previously used to fabricate ring resonator structures and the quality factor was increased from 10, 000 to 35, 000.
- Built an analytic model to study the influence of the substrate on thermally tuning photonic crystal waveguide devices.
- Developed a model for calculating the optical propagation loss due to the sidewall roughness in photonic crystal waveguide.
- Built a model to study the influence of the coupling effect on the energy band structures of self-assembled concentric III-V nanorings.

NANOFABRICATION EXPERIENCE AND SKILLS

Center for Functional Nanomaterials at Brookhaven National Lab (2010-present)

- Successfully fabricated low loss submicron Si photonic structures, such as array bus waveguides, photonic crystal structures, ring resonators, etc, with ultra fine roughness control.
- Skilled in e-beam lithography, dry etching process, and thin film deposition

Micro/Nano Fabrication Lab at Princeton University (2009-2010)

- Designed and fabricated photomasks for lithography by laser writer
- Proficient in photolithography, thin film deposition and characterization.

Microelectronics research lab at Rutgers University (2008-present)

- Well trained in photolithography, wet chemical processes, thermal annealing, mechanical cleaving and polishing.

DESIGN AND MODELING EXPERIENCE AND SKILLS

- Designed and simulated photonic crystal structures for different functionalities, such as superprisms, delay lines, Mach-Zehnder interferometers, etc, by Rsoft (BandSolve, FullWave)
- Modeled and calculated band structures of photonic crystal waveguides by Matlab
- Modeled the thermal response of photonic devices by Comsol (finite-element method)
- Skilled in the simulation of electrical circuits by PSPICE and NI Multisim

METROLOGY EXPERIENCE AND SKILLS

- Built the end-fire fiber-to-chip accurate aligning optical testing system
- Characterization of nanoscale structures by scanning electron microscope (SEM)
- Thin film characterization by ellipsometer, profilometer, reflectometer

PUBLICATIONS

Weiwei Song, Wei Jiang, “High density integration of bus waveguides based on the asymmetric-waveguide-array superlattice structure”, manuscript submitted.

Weiwei Song, Manjit Chahal, George K. Celler, Yogesh Jaluria, Graham T. Reed, and Wei Jiang, “The influence of substrate on SOI photonic crystal thermo-optic devices”, *Optics Express*, vol. 21, 4235 (2013)

Jun Tan, **Weiwei Song**, and Wei Jiang, "Anomalous Propagation in Low Index Contrast Metamaterials: Assessment of the Beam Collimation Condition," *Internation. J. Optics* (special issue on nanoplasmonics and metamaterials), vol. 2012, 120731 (2012)

Lianghong Yin, Ming Lu, Leszek Wielunski, **Weiwei Song**, Jun Tan, Yicheng Lu, and Wei Jiang, “Fabrication and characterization of compact silicon oxynitride waveguide on a silicon chip”, *Journal of Optics*, vol. 14, 085501 (2012)

Ryan A. Integlia, Lianghong Yin, Duo Ding, David Z. Pan, Douglas M. Gill, **Weiwei Song**, Ying Qian, and Wei Jiang, “Fabrication and characterization of parallel-coupled dual racetrack silicon micro-resonators”, *Proc. of SPIE*, vol. 8266, 82660M (2012)

Weiwei Song, Ryan A. Integlia, and Wei Jiang, "Slow light loss due to roughness in photonic crystal waveguides: An analytic approach", *Physical Review B*, vol. 82, 235306 (2010)

Ryan A. Integlia, **Weiwei Song**, Jun Tan, Wei Jiang, “Longitudinal and Angular Dispersions in Photonic Crystals: A Synergistic Perspective on Slow Light and Superprism Effects”, *J. Nanosci. Nanotech.*, vol. 10, 1596 (2010)

Weiwei Song, Guojun Jin, and Yuqiang Ma, “An exciton on coupled concentric double nanorings in a magnetic field” *Journal of Physics: Condensed Matter*. vol. 20, 365222 (2008)

PRESENTATIONS

Weiwei Song, Manjit Chahal, George K. Celler, Yogesh Jaluria, Wei Jiang, “Substrate induced effects in photonic crystal thermo-optic devices on a silicon-on-insulator platform”, *SPIE photonic west*, 8630-29 (2013)

Manjit Chahal, George K. Celler, Yogesh Jaluria, **Weiwei Song**, and Wei Jiang, “Thermo-optic Characteristics and Switching Power Limit of Slow-light Silicon-on-insulator Photonic Crystal Structures”, *Frontiers in Optics*, FTu5A (2012)

Weiwei Song, Ryan A. Integlia, Wei Jiang, “Slow light loss due to roughness in photonic crystal waveguides: insights on loss reduction from an analytic theory”, *SPIE photonic west*, 8269-07(2012)

Weiwei Song, Jun Tan, Ryan A. Integlia, Lianghong Yin, and Wei Jiang, “Ultra-high sensitivity in a photonic crystal superprism due to the curvature singularity of a dispersion surface”, *IEEE Photonics Conference*, 525-526(2011)